

Baryon-baryon interactions in the SU_6 quark model and their applications to light nuclear systems

Y. Fujiwara,¹ Y. Suzuki,² C. Nakamoto,³

¹ Department of Physics, Kyoto University, Kyoto 606-8502, Japan

² Department of Physics, and Graduate School of Science and Technology,
Niigata University, Niigata 950-2181, Japan

³ Suzuka College of Technology, Suzuka 510-0294, Japan

February 9, 2008

Abstract

Interactions between the octet-baryons (B_8) in the spin-flavor SU_6 quark model are investigated in a unified coupled-channels framework of the resonating-group method (RGM). The interaction Hamiltonian for quarks consists of the phenomenological confinement potential, the color Fermi-Breit interaction with explicit flavor-symmetry breaking (FSB), and effective-meson exchange potentials of scalar-, pseudoscalar- and vector-meson types. The model parameters are determined to reproduce the properties of the nucleon-nucleon (NN) system and the low-energy cross section data for the hyperon-nucleon interactions. Mainly due to the introduction of the vector mesons, the NN phase shifts at non-relativistic energies up to $T_{\text{lab}} = 350$ MeV are greatly improved in comparison with the previous quark-model NN interactions. The deuteron properties and the low-energy observables of the B_8B_8 interactions, including the inelastic capture ratio at rest for the Σ^-p scattering, are examined in the particle basis with the pion-Coulomb correction. The nuclear saturation properties and the single-particle (s.p.) potentials of B_8 in nuclear medium are examined through the G -matrix calculations, using the quark-exchange kernel. The Σ s.p. potential is weakly repulsive in symmetric nuclear matter. The s.p. spin-orbit strength for Λ is very small, due to the strong antisymmetric spin-orbit force generated from the Fermi-Breit interaction. The qualitative behavior of the B_8B_8 interactions is systematically understood by 1) the spin-flavor SU_6 symmetry of B_8 , 2) the special role of the pion exchange, and 3) the FSB of the underlying quark Hamiltonian. In particular, the B_8B_8 interaction becomes less attractive according to the increase of strangeness, implying that there exists no B_8B_8 di-baryon bound state except for the deuteron. The strong ΛN - ΣN coupling results from the important tensor component of the one-pion exchange. The $\Lambda\Lambda$ - ΞN - $\Sigma\Sigma$ coupling in the strangeness $S = -2$ and isospin $I = 0$ channel is relatively weak, since this coupling is caused by the strangeness exchange. The B_8B_8 interactions are then applied to some of few-baryon systems and light Λ -hypernuclei in a three-cluster Faddeev formalism using two-cluster RGM kernels. An application to the three-nucleon system shows that the quark-model NN interaction can give a sufficient triton binding energy with little room for the three-nucleon force. The hypertriton Faddeev calculation indicates that the attraction of the ΛN interaction in the 1S_0 state is only slightly more attractive than that in the 3S_1 state. In the application to the $\alpha\alpha\Lambda$ system, the energy spectrum of $^9_\Lambda\text{Be}$ is well reproduced using the $\alpha\alpha$ RGM kernel. The very small spin-orbit splitting of the $^9_\Lambda\text{Be}$ excited states is also discussed. In the $\Lambda\Lambda\alpha$ Faddeev calculation, the NAGARA event for $^6_{\Lambda\Lambda}\text{He}$ is found to be consistent with the quark-model $\Lambda\Lambda$ interaction.

- 1. Introduction
- 2. Formulation
 - 2.1 RGM formalism for quark clusters
 - 2.2 Effective-meson exchange potentials
 - 2.3 The Lippmann-Schwinger formalism for $(3q)$ -($3q$) RGM and the G -matrix equation
 - 2.4 Three-cluster Faddeev formalism using two-cluster RGM kernels
- 3. Results and discussions
 - 3.1 Two-nucleon system
 - 3.2 Hyperon-nucleon interactions
 - 3.2.1 The spin-flavor SU_6 symmetry in the B_8B_8 interactions
 - 3.2.2 Σ^+p system
 - 3.2.3 ΛN system
 - 3.2.4 Σ^-p system
 - 3.2.5 The inelastic capture ratio at rest in the low-energy Σ^-p scattering
 - 3.2.6 YN cross sections
 - 3.2.7 G -matrix calculations
 - 3.3 Interactions for other octet-baryons
 - 3.3.1 $S = -2$ systems
 - 3.3.2 $S = -3$ systems
 - 3.3.3 $S = -4$ systems
 - 3.4 Triton and hypertriton Faddeev calculations
 - 3.4.1 Three-nucleon bound state
 - 3.4.2 The hypertriton
 - 3.5 Application to ${}^9_\Lambda\text{Be}$ and ${}^6_{\Lambda\Lambda}\text{He}$ systems
 - 3.5.1 The $\alpha\alpha\Lambda$ system for ${}^9_\Lambda\text{Be}$
 - 3.5.2 The $\Lambda\Lambda\alpha$ system for ${}^6_{\Lambda\Lambda}\text{He}$
- 4. Summary

1 Introduction

Since the discovery of quantum chromodynamics (QCD), many efforts have been made to understand the structure of hadrons and hadron-hadron interactions based on this fundamental theory of the strong interaction. See, e.g., a review article [1] for these efforts. Such studies are of crucial importance in understanding many-body systems of nuclei and hadronic matter. A direct derivation of these elements from QCD, however, involves tremendous difficulties such as the quark confinement and multi-gluon effects in the low-energy phenomena. This has motivated a study using other effective models which take account of some important QCD characteristics like the color degree of freedom, one-gluon exchange, etc., even though they may not be rigorously derived from QCD.

In this review article, we will focus on the interactions between the octet-baryons (B_8), studied in the non-relativistic quark model (QM), and their applications to light nuclear systems. The QM study

of the baryon-baryon interaction started from applying the three-quark ($3q$) model for the nucleon (N) to the ($3q$)-($3q$) system, in order to obtain a microscopic understanding of the short-range repulsion of the nucleon-nucleon (NN) interaction. Almost 30 years ago Liberman [2] first calculated the quark-exchange kernel of the phenomenological confinement potential and the $(\boldsymbol{\sigma}_i \cdot \boldsymbol{\sigma}_j)(\lambda_i^C \cdot \lambda_j^C)$ -type color-magnetic interaction originating from the Fermi-Breit (FB) interaction. The latter was suggested by De Rújula, Georgi and Glashow [3] as a possible candidate of the quark-quark (qq) residual interaction based on the asymptotic freedom of QCD. The effect of antisymmetrization among quarks is most straightforwardly taken into account in the framework of a microscopic nuclear cluster model, the resonating-group method (RGM). The RGM equation for the ($3q$)-($3q$) system was solved by Oka and Yazaki [4] not only for the NN interaction, but also for the $\Delta\Delta$ interaction. Harvey [5] pointed out the appearance of the so-called hidden-color components in the many-quark systems. The nature of the repulsive core of the NN interaction was studied by Faessler, Fernandez, Lübeck and Shimizu [6] in the framework of RGM, including NN , $\Delta\Delta$ and the hidden-color channels. These early studies were followed by a number of works [7, 8, 9, 10, 11], which repeatedly confirmed that the medium- and long-range effects, usually described by meson-exchange potentials, are absent in the QM and must be incorporated to obtain a realistic description of the baryon-baryon interaction. The first such attempt for the NN interaction was carried out [12] by supplementing the well-established one-pion exchange potential (OPEP) and a phenomenological medium-range central potential in the Schrödinger-type equation equivalent to the RGM equation. The deuteron properties were investigated in relation with the compact ($6q$)-bag configuration [13]. The most successful calculation of the NN interaction in this approach was given in Ref. [14]. The authors introduced the spin-spin and non-central terms of the OPEP, assuming that the pions directly couple with the quarks in the ($3q$) core, and thereby yielding an effective-meson exchange potential (EMEP) at the baryon level. An alternative approach is to assume OPEP between the quarks in the RGM formalism and to calculate the quark-exchange kernel explicitly [15]. This program was carried out by the Tübingen group [16, 17], who extended the model of the NN interaction to the hyperon-nucleon (YN) and hyperon-hyperon (YY) interactions as well. Their approach includes a pseudoscalar (PS) meson exchange between the quarks as well as a phenomenological σ -like potential at the baryon level. A fully microscopic calculation including both PS- and σ -meson exchange potentials at the quark level was undertaken by the Salamanca group [18, 19] for the NN interaction in the framework of the chiral QM. This model was further extended by the Beijing group [20, 21, 22, 23] to a chiral SU_3 model with strangeness degree of freedom, and applied to the YN and YY interactions. In the meantime, meson-exchange models have also made a progress in the description of the medium-range attraction of the YN interaction. The new Jülich YN model [24] has discussed the contributions of the scalar-isoscalar (σ) and vector-isovector (ρ) exchange channels, constrained by a microscopic model of correlated $\pi\pi$ and $K\bar{K}$ exchanges. The extended Nijmegen soft-core model ESC04 [25, 26] has introduced two PS-meson exchange and meson-pair exchange, in addition to the standard one-boson exchange and short-range diffractive exchange potentials.

Our viewpoint for applying the RGM formalism to the baryon-baryon interactions is that the SU_6 QM with some realistic modifications like peripheral mesonic or ($q\bar{q}$) effects can essentially reproduce the whole low-energy hadronic phenomena. For the low-energy phenomena related to the S -wave ground-state hadrons, the predictions with the FB interaction of the one-gluon exchange have no apparent disagreement with experiment except for some trivial cases. Though the FB spin-orbit (LS) interaction is believed not to be favorable for the very small energy splitting of the negative-parity nucleon excited states, known as the “missing LS force problem” of the P -wave baryons, it was argued in Ref. [27] that this problem can be resolved by a proper treatment of a compact ($3q$) structure embedded in the ($3q$)($q\bar{q}$) continua. In other papers [28, 29], we showed that the same FB LS force has almost right order of magnitude compatible with the experimental information on the NN and YN spin-orbit interaction. Fujiwara and Hecht discussed in [30, 31] the off-shell FB interaction in the non-relativistic framework and incorporated the meson-exchange effects to the ($3q$)-($3q$) RGM by explicitly

introducing $(q\bar{q})$ and $(q\bar{q})^2$ excitations. As the main feature of the NN interaction was reproduced in the extended QM without introducing any extra meson parameters, it may be considered the first step toward the conventional meson-exchange description through a possible mechanism of $(q\bar{q})$ exchanges between nucleons. An extension of the model to include the antiquark degree of freedom is also made to describe other hadronic interactions such as the pion-pion and pion-nucleon scatterings as well as the proton-antiproton annihilation processes [32, 33, 34].

We note that to apply the RGM formalism to the $(3q)$ – $(3q)$ system is not straightforward, since there are some new features arising from the intrinsically relativistic nature of the system. The standard non-relativistic RGM formulation should be augmented with the following features: 1) the full FB interaction with flavor-symmetry breaking (FSB), including the momentum-dependent Breit retardation term and the Galilean non-invariant LS term, 2) a $(0s)^3$ harmonic-oscillator (h.o.) wave function with a common size parameter b for all the $(3q)$ systems, 3) a perturbative treatment of the FSB, in terms of the pure SU_6 QM wave functions with the [3]-symmetric spatial function, and 4) correct reduced masses and threshold energies in the RGM formalism. See Refs. [35, 36] for the background of these extensions.

The effective qq interaction in our model consists of a phenomenological quark-confining potential, the one-gluon exchange FB interaction, and other terms generating EMEP's from various meson-exchange mechanisms. Various versions of our QM for the baryon-baryon interactions emerge from several possibilities of how to incorporate these EMEP's in the RGM equation. A simplest method is to use effective local potentials V^{eff} at the baryon level, which are determined from the existing one-boson exchange potentials (OBEP) with some adjustable parameters. From the correspondence between the RGM formalism for composite particles and the Schrödinger equation for structureless particles, the relative-motion wave function should be renormalized with the square root of the normalization kernel \sqrt{N} . A nice point of this prescription is that we only need the normalization kernel to generate the exchange terms. Our earliest version of the QM, **RGM-F** [35, 36, 37], uses this prescription for EMEP's, where V^{eff} is assumed to be proportional to the scalar- (S-) meson and PS-meson exchange potentials of the Nijmegen model-F [38]. More specifically, the central force of the S-meson nonet and the tensor force of the π and K mesons in the Nijmegen model-F are used. With only two adjustable parameters determined in the NN sector, RGM-F can reproduce reasonably well all the low-energy cross section data of the YN systems.

In the next step, we have improved the way of introducing the EMEP's in two respects. One is to calculate the spin-flavor factors exactly at the quark level and the other is to include the spin-spin terms originating from all the PS mesons. We have shown in Ref. [39] that the available NN and YN data can simultaneously be reproduced in the standard $(3q)$ – $(3q)$ formulation, if one assumes the full PS- and S-meson nonet exchanges at the quark level and properly introduces the FSB in the quark sector. An explicit evaluation of quark-exchange kernels for the EMEP leads to a strong constraint on the flavor dependence of each NN and YN channel. The SU_3 relation of the coupling constants emerges as a natural consequence of the SU_6 QM. For S mesons, one of the SU_3 parameters, $F/(F+D)$ ratio, turns out to take the SU_6 value of a purely electric type. Under this restriction, the low-energy NN , Σ^+p and Λp total cross sections cannot be reproduced consistently with a unique mixing angle of the flavor-singlet and octet S mesons. We resolve this problem in two ways; one is to change the mixing angle only for Σ^+p channel and the other is to employ the same approximation as RGM-F, changing the $F/(F+D)$ ratio, solely for the isoscalar S mesons, ϵ and S^* . These models are called **FSS** and **RGM-H** [39, 40, 41], respectively. Since their predictions are not much different except for the roles of the $LS^{(-)}$ force in the ΛN – ΣN ($I = 1/2$) coupled-channels (CC) system, the result with FSS will be discussed in this article.

In the most recent model called **fss2** [42, 43], we have also included the following interaction pieces mediated by S and vector (V) mesons: LS , quadratic spin-orbit (QLS), and momentum-dependent Bryan-Scott terms. The introduction of these terms to the EMEP's is primarily motivated by the

insufficient description of the NN experimental data with our previous models. Due to these improvements, the NN phase shifts at non-relativistic energies up to $T_{\text{lab}} = 350$ MeV have attained an accuracy almost comparable to that of OBEP's. The model parameters are searched in the isospin basis to fit the NN phase-shift analysis with $J \leq 2$ and $T_{\text{lab}} \leq 350$ MeV, the deuteron binding energy, the 1S_0 NN scattering length, and the low-energy YN total cross section data. The model fss2 reproduces the YN scattering data and the essential features of the ΛN – ΣN coupling equally well with our previous models. Another important progress for the QM baryon-baryon interaction has come from a technique to solve the RGM equation in the momentum representation. Here we solve the T -matrix equation of the RGM kernel, for which all the Born terms are derived analytically. The partial wave decomposition of the Born kernel is carried out numerically in the Gauss-Legendre integral quadrature. This method, called Lippmann-Schwinger RGM (LS-RGM) [44], enables us not only to obtain very stable and accurate results for the S -matrix over a wide energy range up to a few GeV, but also to apply our QM baryon-baryon interactions to physically interesting problems such as G -matrix and three-cluster Faddeev calculations. The single-particle (s.p.) potentials of the B_8 (N , Λ and Σ) and the strength of the s.p. spin-orbit potential are predicted through the G -matrix calculations [45, 46].

We have carried out coupled-channels RGM (CCRGM) calculations both in the isospin basis and in the physical particle basis. The former is convenient to show concisely the characteristics of the $B_8 B_8$ interactions, but the latter is necessary to make a realistic evaluation of cross sections for a comparison with experimental data. The latter is also necessary for the study of the charge dependence of the NN interaction and the charge-symmetry breaking (CSB) of the ΛN interaction. The charge-independence breaking (CIB) is partially explained by the so-called pion-Coulomb correction [47], which implies 1) the small mass difference of the neutron and the proton, 2) the mass difference of the charged pions and the neutral pion, and 3) the Coulomb effect. For the CSB of the ΛN interaction, the early version of the Nijmegen potential [48] already focused on this CSB in the OBEP including the pion-Coulomb correction and the correct threshold energies of the ΛN – ΣN coupling in the particle basis. We always include the pion-Coulomb correction when the particle basis is used for the calculation. For the Coulomb effect, we calculate the full exchange kernel without any approximation. The pion-Coulomb correction and the correct treatment of the threshold energies are found to be very important to analyze the low-energy observables in the ΣN – ΛN CC problem.

In the next section, we briefly describe the formulation of the $(3q)$ – $(3q)$ RGM and its application to the G -matrix and Faddeev calculations. These formulations are made in the momentum representation. The essential points to be emphasized include the energy dependence of the RGM kernel and the existence of the Pauli-forbidden state. The treatment of the Coulomb force in the momentum representation is also given. Section 3 presents results and discussions. We start with the two-nucleon properties and proceed to the YN interaction, the G -matrix calculations, the YY interaction and the other $B_8 B_8$ interactions including the ΞN , ΞY and $\Xi \Xi$ interactions. The importance of the spin-flavor SU_6 symmetry in our QM framework is stressed through a systematic analysis of the phase-shift behavior and total cross sections in some particular channels. In Sec. 3.4, our QM baryon-baryon interactions, FSS and fss2, are applied to the calculations of the triton and hypertriton binding energies in the three-cluster Faddeev formalism. The application to other light hypernuclei, $^9_\Lambda\text{Be}$ and $^6_{\Lambda\Lambda}\text{He}$, is given in Sec. 3.5. The spin-orbit splitting of $^9_\Lambda\text{Be}$ excited states is also examined by the Faddeev and G -matrix calculations. A summary is drawn in Sec. 4.

2 Formulation

2.1 RGM formalism for quark clusters

The RGM is a microscopic theory which describes the dynamical motion of clusters, on the basis of two- (and three-, \dots) body interactions of constituent particles. For the application to baryon-baryon interactions in the QM, the B_8 's are assumed to be simple s -shell clusters composed of the $(0s)^3$ h.o. wave functions with a common size parameter b . They have spin-flavor and color degrees of freedom as well, for which we follow the standard non-relativistic SU_6 description. We use the Elliott notation to specify the SU_3 quantum numbers of B_8 , and write $B_8 = B_{(11)a}$ with $a \equiv YI$ (hypercharge Y , isospin I) to denote a flavor function N ($YI = 1\frac{1}{2}$), Λ ($YI = 00$), Σ ($YI = 01$) or Ξ ($YI = -1\frac{1}{2}$). We also use the notation $\alpha = aI_z$ to denote a specific member of the isospin multiplet for each baryon. Then the QM description of the B_8 is achieved with the correspondence

$$B_{(11)\alpha} \sim W_{\frac{1}{2}(11)\alpha}^{[3]}(123) = \sum_{S(\lambda\mu)=0(01), 1(20)} \frac{1}{\sqrt{2}} [[w_{\frac{1}{2}}(1)w_{\frac{1}{2}}(2)]_S w_{\frac{1}{2}}(3)]_{\frac{1}{2}} \times [[F_{(10)}(1)F_{(10)}(2)]_{(\lambda\mu)} F_{(10)}(3)]_{(11)\alpha} , \quad (2.1)$$

because the spin-flavor part of B_8 is totally symmetric. Here $w_{\frac{1}{2}}$ is the spin wave function and $F_{(10)}$ the flavor wave function of a single quark. The QM wave functions of the B_8 are expressed as

$$\phi_{B_8}(123) = \phi^{(\text{orb})}(123) W_{1/2(11)\alpha}^{[3]}(123) C(123) , \quad (2.2)$$

where $C(123)$ is the color-singlet wave function. The orbital wave function, $\phi^{(\text{orb})}(123)$, is an intrinsic part of B_8 and contains no dependence on the c.m. coordinate $\mathbf{X}_G = (\mathbf{x}_1 + \mathbf{x}_2 + \mathbf{x}_3)/3$. The orbital functions for the $(3q)$ -clusters are thus assumed to be flavor-independent and are taken to be the same for all the B_8 's.

The RGM wave function for the $(3q)$ -($3q$) system can be expressed as

$$\Psi = \sum_{\alpha} \mathcal{A}' \{ \phi_{\alpha} \chi_{\alpha}(\mathbf{R}) \} , \quad (2.3)$$

where the channel wave function $\phi_{\alpha} = \phi^{(\text{orb})} \xi_{\alpha}^{SF} \xi^C$ is composed of the orbital part of the internal wave function $\phi^{(\text{orb})} = \phi^{(\text{orb})}(123)\phi^{(\text{orb})}(456)$, the isospin-coupled basis ξ_{α}^{SF} of the spin-flavor SU_6 wave functions and $\xi^C = C(123)C(456)$. A detailed definition of ξ_{α}^{SF} with a set of specific two-baryon quantum numbers α will be given below. The antisymmetrization operator \mathcal{A}' in Eq. (2.3) makes Ψ totally antisymmetric under the exchange of any quark pairs and can be reduced to the form $\mathcal{A}' \rightarrow (1/2)(1 - 9P_{36})(1 - P_0)$ with the core-exchange operator of the two $(3q)$ -clusters $P_0 = P_{14}P_{25}P_{36}$.

We now explain the basis ξ_{α}^{SF} . In the general $B_8 B_8$ interaction, there appear several new features which are absent in the NN interaction. These are mainly related to the rich flavor contents of the $B_8 B_8$ system constrained by the spin-flavor SU_6 symmetry and the generalized Pauli principle. Since these features are common in both OBEP and QM descriptions, we will use the baryon's degree of freedom as much as possible. Here we use the isospin-coupled basis for presentation, but the transformation to the physical particle basis is straightforward. The SU_3 -coupled basis of two B_8 's is defined by

$$\begin{aligned} [B_{(11)}B_{(11)}]_{(\lambda\mu)\alpha;\rho} &= [B_{(11)}(1) B_{(11)}(2)]_{(\lambda\mu)\alpha;\rho} \\ &= \sum_{a_1, a_2} \langle (11)a_1 (11)a_2 \parallel (\lambda\mu)a \rangle_{\rho} [B_{(11)a_1}(1) B_{(11)a_2}(2)]_{II_z} , \end{aligned} \quad (2.4)$$

where the last brackets denote the isospin coupling and ρ denotes a possible multiplicity label of the SU_3 coupling, $(11) \times (11) \rightarrow (22) + (30) + (03) + (11)_s + (11)_a + (00)$ ($\rho = 1$ for $(11)_a$ and $\rho = 2$ for

(11)_s). We assume that the first $B_{(11)}$ is always for particle 1 and the second for particle 2. A set of the internal quantum numbers, α ($\alpha = aI_z$), stand for the hypercharge $Y = Y_1 + Y_2$, the total isospin I and its z -component I_z , which are all conserved quantities if we assume the isospin symmetry and the charge conservation $Q/e = Y/2 + I_z$. Only when the particle-basis is used, the isospin I is no longer “exactly” conserved. The flavor-symmetry phase \mathcal{P} of the two-baryon system is determined from the symmetry of the SU_3 Clebsch-Gordan coefficients through

$$P_{12}^F [B_{(11)} B_{(11)}]_{(\lambda\mu)\alpha;\rho} = \mathcal{P} [B_{(11)} B_{(11)}]_{(\lambda\mu)\alpha;\rho} , \quad (2.5)$$

with

$$\mathcal{P} = \begin{cases} (-1)^{\lambda+\mu} & \text{in multiplicity-free case ,} \\ (-1)^\rho & \text{for } (\lambda\mu) = (11) . \end{cases} \quad (2.6)$$

Here $P_{12}^F = (\lambda_1^F \cdot \lambda_2^F)/2 + 1/3$ is the flavor-exchange operator with λ_i^F ($i = 1, 2$) being the Gell-Mann matrices for the flavor degree of freedom. It is important to maintain the definite flavor symmetry even in the isospin-coupled basis and in the particle basis, since the flavor symmetry is related to the total spin and the parity through the generalized Pauli principle;

$$(-1)^{L+S} \mathcal{P} = 1 , \quad (2.7)$$

where L is the relative orbital angular momentum. For the NN system with $Y = 2$, the total isospin I is good enough to specify \mathcal{P} ; i.e., $\mathcal{P} = (-1)^{1-I}$, so that Eq. (2.7) becomes the well-known rule $(-1)^{L+S+I} = -1$. More generally, the flavor-exchange symmetry \mathcal{P} is actually redundant for the systems of identical particles with $a_1 = a_2$ and $I_1 = I_2$, since it is uniquely determined as $\mathcal{P} = (-1)^{2I_1-I}$. Let us introduce a simplified notation $B_i \equiv B_{(11)a_i}$ ($i = 1, \dots, 4$ in general) with $a_i = Y_i I_i$. Then the symmetrized isospin basis is defined through

$$\begin{aligned} [B_1 B_2]_{II_z}^{\mathcal{P}} &= \frac{1}{\sqrt{2(1 + \delta_{B_1 B_2})}} \{ [B_1 B_2]_{II_z} + \mathcal{P} (-1)^{I_1+I_2-I} [B_2 B_1]_{II_z} \} \\ &= \sqrt{\frac{2}{1 + \delta_{B_1 B_2}}} \sum_{(\lambda\mu)\rho \in \mathcal{P}} \langle (11)a_1 (11)a_2 \parallel (\lambda\mu)a; \rho \rangle [B_{(11)} B_{(11)}]_{(\lambda\mu)\alpha;\rho} , \end{aligned} \quad (2.8)$$

where the sum is over $(\lambda\mu)\rho$ compatible with Eq. (2.6). As is apparent from the construction, the basis in Eq. (2.8) is naturally an eigenstate of the flavor-exchange operator P_{12}^F with the eigenvalue \mathcal{P} . It is now straightforward to incorporate the spin degree of freedom in the above formulation and extend the argument to the spin-flavor SU_6 wave functions of the $(3q)$ -($3q$) system. In the QM, the isospin basis with a definite flavor-exchange symmetry is given by

$$\begin{aligned} \xi_\alpha^{SF} &= \frac{1}{\sqrt{2(1 + \delta_{a_1 a_2})}} \left\{ \left[W_{\frac{1}{2}(11)a_1}^{[3]} (123) W_{\frac{1}{2}(11)a_2}^{[3]} (456) \right]_{SS_z II_z} \right. \\ &\quad \left. + \mathcal{P} (-1)^{I_1+I_2-I} \left[W_{\frac{1}{2}(11)a_2}^{[3]} (123) W_{\frac{1}{2}(11)a_1}^{[3]} (456) \right]_{SS_z II_z} \right\} . \end{aligned} \quad (2.9)$$

The subscript α in Eq. (2.9) specifies a set of quantum numbers of the channel wave function;

$$\alpha \equiv \left[\frac{1}{2}(11) a_1 \frac{1}{2}(11) a_2 \right] SS_z Y II_z; \mathcal{P} . \quad (2.10)$$

In the particle basis, we use the notation $B_{\alpha_i} = B_{(11)\alpha_i}$ and define

$$\begin{aligned} (B_{\alpha_1} B_{\alpha_2})^{\mathcal{P}} &= \frac{1}{\sqrt{2(1 + \delta_{\alpha_1, \alpha_2})}} (B_{\alpha_1} B_{\alpha_2} + \mathcal{P} B_{\alpha_2} B_{\alpha_1}) \\ &= \sqrt{\frac{1 + \delta_{a_1, a_2}}{1 + \delta_{\alpha_1, \alpha_2}}} \sum_{II_z} \langle I_1 I_{1z} I_2 I_{2z} \parallel II_z \rangle [B_1 B_2]_{II_z}^{\mathcal{P}} . \end{aligned} \quad (2.11)$$

The channel quantum number α in Eq. (2.10) in this case is specified by $\alpha \equiv [\frac{1}{2}(11) \alpha_1 \frac{1}{2}(11) \alpha_2] SS_z; \mathcal{P}$ with $Y = Y_1 + Y_2$ and $I_z = I_{1z} + I_{2z}$. For the system of identical particles with $\alpha_1 = \alpha_2$, the flavor-exchange symmetry is again redundant and $\mathcal{P} = 1$. The relationship between the isospin basis and the particle basis in Eq. (2.11) is inversely written as

$$[B_1 B_2]_{II_z}^{\mathcal{P}} = \sum_{I_{1z} I_{2z}} \sqrt{\frac{1 + \delta_{\alpha_1, \alpha_2}}{1 + \delta_{a_1, a_2}}} \langle I_1 I_{1z} I_2 I_{2z} | II_z \rangle (B_{\alpha_1} B_{\alpha_2})^{\mathcal{P}}. \quad (2.12)$$

The bases in Eqs. (2.9) and (2.11) are the eigenstates of the core exchange operator $P_0^{SF} = P_{14}^{SF} P_{25}^{SF} P_{36}^{SF}$ with the eigenvalue $(-1)^{1-S} \mathcal{P}$, where $P_{ij}^{SF} = P_{ij}^{\sigma} P_{ij}^F$ exchanges the spin-flavor coordinates.

The QM Hamiltonian consists of the rest-mass plus non-relativistic kinetic-energy term, the quadratic confinement potential, the full FB interaction with explicit quark-mass dependence, and the S-, PS-, and V-meson exchange potentials acting between quarks:

$$H = \sum_{i=1}^6 \left(m_i c^2 + \frac{\mathbf{p}_i^2}{2m_i} - T_G \right) + \sum_{i < j}^6 \left(U_{ij}^{\text{Cf}} + U_{ij}^{\text{FB}} + \sum_{\beta} U_{ij}^{\text{S}\beta} + \sum_{\beta} U_{ij}^{\text{PS}\beta} + \sum_{\beta} U_{ij}^{\text{V}\beta} \right). \quad (2.13)$$

Here $U_{ij}^{\text{Cf}} = -(\lambda_i^C \cdot \lambda_j^C) a_c r^2$ with $r = |\mathbf{r}| = |\mathbf{x}_i - \mathbf{x}_j|$ is the confinement potential of quadratic power law, which gives a vanishing contribution to the interaction in the present formalism. The qq FB interaction U_{ij}^{FB} is composed of the following pieces [7, 49]:

$$U_{ij}^{\text{FB}} = U_{ij}^{CC} + U_{ij}^{MC} + U_{ij}^{GC} + U_{ij}^{sLS} + U_{ij}^{aLS} + U_{ij}^T, \quad (2.14)$$

where the superscript (CC) stands for the color-Coulombic or $(\lambda_i^C \cdot \lambda_j^C)/r$ piece, (MC) for the momentum-dependent Breit retardation term or $(\lambda_i^C \cdot \lambda_j^C) \{ (\mathbf{p}_i \cdot \mathbf{p}_j) + \mathbf{r}(\mathbf{r} \cdot \mathbf{p}_i) \cdot \mathbf{p}_j / r^2 \} / (m_i m_j r)$ piece, (GC) for the combined color-delta and color-magnetic or $(\lambda_i^C \cdot \lambda_j^C) \{ 1/(2m_i^2) + 1/(2m_j^2) + 2/(3m_i m_j) (\boldsymbol{\sigma}_i \cdot \boldsymbol{\sigma}_j) \} \delta(\mathbf{r})$ piece, (sLS) for the symmetric LS , (aLS) for the antisymmetric LS , and (T) for the tensor term. It is important to note that all the contributions from the FB interaction are generated from the quark-exchange diagrams, since we assume color-singlet cluster wave functions. The EMEP's, $U_{ij}^{\text{S}\beta}$, $U_{ij}^{\text{PS}\beta}$, and $U_{ij}^{\text{V}\beta}$ will be discussed in the next section. When the calculations are made in the particle basis, the Coulomb force is also introduced at the quark level.

The RGM equation for the parity-projected relative wave function $\chi_{\alpha}^{\pi}(\mathbf{R})$ is derived from the variational principle $\langle \delta \Psi | E - H | \Psi \rangle = 0$, and it reads as [11, 40]

$$\left[\varepsilon_{\alpha} + \frac{\hbar^2}{2\mu_{\alpha}} \left(\frac{\partial}{\partial \mathbf{R}} \right)^2 \right] \chi_{\alpha}^{\pi}(\mathbf{R}) = \sum_{\alpha'} \int d\mathbf{R}' \mathcal{M}_{\alpha\alpha'}(\mathbf{R}, \mathbf{R}'; E) \chi_{\alpha'}^{\pi}(\mathbf{R}'), \quad (2.15)$$

where $\mathcal{M}_{\alpha\alpha'}(\mathbf{R}, \mathbf{R}'; E)$ is composed of various pieces of the interaction kernels as well as the direct potentials of EMEP:

$$\mathcal{M}_{\alpha\alpha'}(\mathbf{R}, \mathbf{R}'; E) = \delta(\mathbf{R} - \mathbf{R}') \sum_{\beta} \sum_{\Omega} V_{\text{D}\alpha\alpha'}^{\Omega\beta}(\mathbf{R}) + \sum_{\Omega} \mathcal{M}_{\alpha\alpha'}^{\Omega}(\mathbf{R}, \mathbf{R}') - \varepsilon_{\alpha} \mathcal{M}_{\alpha\alpha'}^N(\mathbf{R}, \mathbf{R}'). \quad (2.16)$$

The relative energy ε_{α} in channel α is related to the total energy E of the system in the c.m. system through $\varepsilon_{\alpha} = E - E_a^{\text{int}}$, where $E_a^{\text{int}} = E_{a_1}^{\text{int}} + E_{a_2}^{\text{int}}$ with $a = a_1 a_2$. In Eq. (2.16) the sum over Ω in the direct term implies various contributions of interaction types for the meson-exchange potentials, while β specifies the meson species. These EMEP interaction types are classified to $\Omega = CN, SS, TN, LS$, and QLS , which are the spin-independent central, spin-spin, tensor, LS , and quadratic LS terms,

respectively. On the other hand, Ω for the exchange kernel $\mathcal{M}_{\alpha\alpha'}^{\Omega}(\mathbf{R}, \mathbf{R}')$ involves not only the exchange kinetic-energy (K) term but also various pieces (CC , MC , GC , sLS , aLS , T) of the FB interaction, as well as the EMEP contributions corresponding to the direct term. The structure of the EMEP contributions is rather involved and contains some ambiguities in the way of introducing them even starting from the meson-exchange potentials at the quark level, as will be discussed in the next section. Here we only refer to a general procedure to solve the RGM equation (2.15) and a couple of important features of the present RGM framework using solely qq interactions.

A simple way to solve the CCRGM equation (2.15) is the variational method developed by Kamimura [50]. Although this technique gives accurate results up to about $T_{\text{lab}} = 300$ MeV, it seems almost inaccessible to higher energies due to the rapid oscillation of the relative wave functions. We alternatively use a method to solve the CCRGM equation in the momentum representation, namely, an LS-RGM equation [44]. The idea of solving the RGM equation in the momentum representation is not new [51]. It is also used by Salamanca group in the study of the QM baryon-baryon interactions [52]. In this method all the necessary Born amplitudes (or the Born kernels) for the quark-exchange kernels are analytically derived by using a transformation formula, which is specifically developed for momentum-dependent two-body interactions acting between quarks [44]. The partial-wave decomposition of the Born kernel is carried out numerically in the Gauss-Legendre integral quadrature. The LS-RGM equation is then solved by using the techniques developed by Noyes [53] and Kowalski [54]. Although this method requires more CPU time than the variational method, it gives very stable and accurate results in a wide energy range. Since we first calculate the Born amplitudes of the RGM kernel, it is almost straightforward to proceed to the G -matrix calculations [45], as well as many Faddeev calculations in the three-cluster Faddeev formalism. The transformation to the RGM equation (2.15) is easily carried out by simple Fourier transformations.

A nice property of the present RGM formalism is that the internal-energy contribution is already subtracted in the exchange kernel. Namely, $\mathcal{M}_{\alpha\alpha'}^{(\Omega)}(\mathbf{R}, \mathbf{R}')$ in Eq. (2.16) for the central components $\Omega = K$, CC , MC , GC , CN , and SS is defined through its corresponding original exchange kernel $\mathcal{M}_{\alpha\alpha'}^{(\Omega)exch}(\mathbf{R}, \mathbf{R}')$:

$$\mathcal{M}_{\alpha\alpha'}^{(\Omega)}(\mathbf{R}, \mathbf{R}') = \mathcal{M}_{\alpha\alpha'}^{(\Omega)exch}(\mathbf{R}, \mathbf{R}') - (E_{a_1}^{(\Omega)} + E_{a_2}^{(\Omega)}) \mathcal{M}_{\alpha\alpha'}^N(\mathbf{R}, \mathbf{R}') \quad , \quad (2.17)$$

where $E_a^{(\Omega)}$ denotes the Ω -term contribution to the internal energy of the B_8 specified by the flavor label $a = a_1 a_2$. Owing to this subtraction, the mass term of the kinetic-energy operator in Eq. (2.13) as well as the confinement potential with $\Omega = \text{Cf}$ exactly cancels between the first and the second terms on the right-hand side of Eq. (2.17). We consider this feature one of the advantages of the RGM formalism, because the present QM produces those results which are independent of the strength of the confinement potential and are insensitive to the details of the confinement phenomenology.

We should note that the original Hamiltonian (2.13) in general contains the derivative operators $\partial/\partial\mathbf{x}_i$ and $\partial/\partial\mathbf{x}_j$, which cannot be reduced to the derivative of the relative coordinate $\mathbf{r} = \mathbf{x}_i - \mathbf{x}_j$ between two quarks. The appearance of these Galilean non-invariant terms, like the momentum-dependent Breit retardation term U_{ij}^{MC} and the antisymmetric LS term U_{ij}^{aLS} , is a direct consequence of the more strict Lorentz invariance at the relativistic level, and their RGM kernel should be explicitly evaluated in the total c.m. system [28, 35]. We include the U_{ij}^{MC} term and take account of its contribution to the relative kinetic-energy term explicitly. Even with this procedure, the calculated reduced mass of the ΣN system is degenerate with that of the ΛN system. This is one of the limitations of the non-relativistic QM, in which the inertia masses (of Σ and Λ in the present case) are not always reproduced correctly. In order to use the correct reduced masses in the CCRGM equation, we make the following replacement only for the exchange kernels $\mathcal{M}_{\alpha\alpha'}^{(K)}(\mathbf{R}, \mathbf{R}')$ and $\mathcal{M}_{\alpha\alpha'}^{(MC)}(\mathbf{R}, \mathbf{R}')$:

$$\mathcal{M}_{\alpha\alpha'}^{(\Omega)}(\mathbf{R}, \mathbf{R}') \rightarrow \widetilde{\mathcal{M}}_{\alpha\alpha'}^{(\Omega)}(\mathbf{R}, \mathbf{R}') = \frac{\mu_{\alpha_0}}{\mu_{\alpha_0}^{exp}} \mathcal{M}_{\alpha\alpha'}^{(\Omega)}(\mathbf{R}, \mathbf{R}') \quad \Omega = K \quad \text{and} \quad MC \quad , \quad (2.18)$$

where α_0 is the incident channel. (This prescription is slightly different from that of Refs. [37, 40].) For such a case that the exact Pauli-forbidden state exists in the CC system, a modification is necessary as discussed in Sec. 4 of Ref. [55]. The essential idea is as follows. Let us express the CCRGM equation (2.15) as

$$(\varepsilon - H_0 - V^{\text{RGM}})\chi = 0 , \quad (2.19)$$

with $\varepsilon = E - E_{\text{int}}$ and $V^{\text{RGM}} = V_{\text{D}} + G + \varepsilon K$. Here V^{RGM} represents the RGM kernel in Eq. (2.16) with V_{D} the direct potential, G the exchange kernel $\sum_{\Omega} \mathcal{M}_{\alpha\alpha'}^{\Omega}(\mathbf{R}, \mathbf{R}')$, and K the exchange normalization kernel $-\mathcal{M}_{\alpha\alpha'}^N(\mathbf{R}, \mathbf{R}')$. The essential feature of the RGM equation (2.19) is the existence of the trivial solution $\chi = u$, which satisfies $Ku = u$. If we use the projection operator on the Pauli-allowed space, $\Lambda = 1 - |u\rangle\langle u|$, Eq. (2.19) can equivalently be written as

$$\Lambda(\varepsilon - H_0 - V^{\text{RGM}})\Lambda\chi = 0 . \quad (2.20)$$

In this form, we can safely replace the calculated reduced mass μ_{α} with the empirical mass $\mu_{\alpha}^{\text{exp}}$. Quite obviously, this procedure is accurate only when the calculated mass is a good approximation for the empirical mass. The same procedure is also applied when we formulate the CCRGM equation in the particle basis. The present constituent QM does not reproduce the small mass difference of the isospin multiplets exactly even if the FSB of the quark masses and the Coulomb interaction at the quark level are properly introduced. We therefore solve the modified equation

$$\Lambda(\varepsilon^{\text{exp}} - H_0^{\text{exp}} - V^{\text{RGM}})\Lambda\chi = 0 , \quad (2.21)$$

instead of Eq. (2.20), where ε^{exp} and H_0^{exp} are defined by

$$\varepsilon^{\text{exp}} = E - E_{\text{int}}^{\text{exp}} , \quad H_0^{\text{exp}} = -\frac{\hbar^2}{2\mu^{\text{exp}}} \left(\frac{\partial}{\partial \mathbf{R}} \right)^2 = \frac{\mu}{\mu^{\text{exp}}} H_0 . \quad (2.22)$$

This procedure to use the empirical reduced masses and threshold energies in the Pauli-allowed model space has a wide applicability to remedy the inflexibility of the RGM framework. If we restore Eq. (2.22) to the original Schrödinger-type equation (2.19), we obtain an additional correction term to the RGM kernel, which is supposed to be small enough for practical calculations, but necessary to preserve the exact treatment of the Pauli principle:

$$(\varepsilon^{\text{exp}} - H_0^{\text{exp}} - V^{\text{RGM}} - \Delta G)\chi = 0 . \quad (2.23)$$

Here ΔG is given by

$$\Delta G = \Lambda (\Delta E_{\text{int}} + \Delta H_0) \Lambda - (\Delta E_{\text{int}} + \Delta H_0) \quad (2.24)$$

with

$$\Delta E_{\text{int}} = E_{\text{int}}^{\text{exp}} - E_{\text{int}} , \quad \Delta H_0 = H_0^{\text{exp}} - H_0 = \left(\frac{\mu}{\mu^{\text{exp}}} - 1 \right) H_0 . \quad (2.25)$$

A detailed example is given in Ref. [55] for the ΛN - ΣN ($I = 1/2$) CCRGM, which involves a Pauli-forbidden state in the $(11)_s$ SU_3 representation for the 1S_0 state [37]. With this procedure we can employ the empirical reduced masses and threshold energies without impairing the major role of the Pauli principle.

2.2 Effective-meson exchange potentials

In this subsection, we outline a procedure to derive the RGM kernel, starting from a general form of the qq interaction, and discuss appropriate forms of the EMEP's used in the model FSS and fss2. Refer to the original papers [56, 57, 40, 42, 44] for detailed calculations.

The systematic evaluation of the quark-exchange kernel is carried out for a two-body interaction

$$U_{ij}^\Omega = \alpha^\Omega w_{ij}^\Omega w_{ij}^C u_{ij}^\Omega, \quad (2.26)$$

where α^Ω is a simple numerical factor including a single quark-gluon coupling constants $\alpha_S = g_{qG}^2/(4\pi)$ and various types of quark-meson coupling constants $g_{qq\beta}$, $f_{qq\beta}$, etc., w_{ij}^Ω represents the spin-flavor part, w_{ij}^C the color part and u_{ij}^Ω the spatial part. The color part is $w_{ij}^C = (1/4)(\lambda_1^C \cdot \lambda_2^C)$ for the FB interaction and $w_{ij}^C = 1$ for EMEP's. In Table 1, α^Ω , w_{ij}^Ω and u_{ij}^Ω are given for the FB interaction [7], while those for EMEP's in Tables VII and VIII of Ref. [42]. Four different types of the spin-flavor factors $\Omega = C, SS, T, LS$ are required for the most general EMEP up to the V mesons; $w_{ij}^C = 1$, $w_{ij}^{SS} = (\boldsymbol{\sigma}_i \cdot \boldsymbol{\sigma}_j)$, $w_{ij}^T = [\boldsymbol{\sigma}_i \boldsymbol{\sigma}_j]_\mu^{(2)}$, and $w_{ij}^{LS} = (\boldsymbol{\sigma}_i + \boldsymbol{\sigma}_j)/2$. For the flavor-octet mesons, these spin operators should be multiplied with $(\lambda_i^F \cdot \lambda_j^F)$. The non-central factors are defined by the reduced matrix elements for the tensor operators of rank 1 and 2. For example, the tensor operator is expressed as

$$S_{12}(\mathbf{k}, \mathbf{k}) = 3(\boldsymbol{\sigma}_i \cdot \mathbf{k})(\boldsymbol{\sigma}_j \cdot \mathbf{k}) - (\boldsymbol{\sigma}_i \cdot \boldsymbol{\sigma}_j) \mathbf{k}^2 = 3\sqrt{10} \left[[\boldsymbol{\sigma}_i \boldsymbol{\sigma}_j]^{(2)} \mathcal{Y}_2(\mathbf{k}) \right]^{(0)}, \quad (2.27)$$

with $\mathcal{Y}_{2\mu}(\mathbf{k}) = \sqrt{4\pi/15} \mathbf{k}^2 Y_{2\mu}(\hat{\mathbf{k}})$. The Born kernel for the two-body interaction (2.26) is calculated by

$$M(\mathbf{q}_f, \mathbf{q}_i) = \langle e^{i\mathbf{q}_f \cdot \mathbf{R}} \phi | \sum_{i < j}^6 U_{ij} \mathcal{A}' | e^{i\mathbf{q}_i \cdot \mathbf{R}} \phi \rangle = \sum_{xT} X_{xT} M_{xT}(\mathbf{q}_f, \mathbf{q}_i). \quad (2.28)$$

where $\phi = \phi^{(\text{orb})} \xi$ with $\xi = \xi^{SF} \xi^C$ is the h.o. internal wave function of the $(3q)$ -($3q$) system and the superscript Ω for specifying the interaction piece, as well as the channel subscript α , are omitted for simplicity. In Eq. (2.28), the spatial part of the Born kernel is expressed as

$$M_{xT}(\mathbf{q}_f, \mathbf{q}_i) = \langle z_x e^{i\mathbf{q}_f \cdot \mathbf{R}} \phi^{(\text{orb})} | u_{ij} | e^{i\mathbf{q}_i \cdot \mathbf{R}} \phi^{(\text{orb})} \rangle \quad \text{with} \quad (i, j) \in \mathcal{T}. \quad (2.29)$$

Table 1: The coefficients α^Ω , the corresponding spatial functions $u^\Omega(\mathbf{k}, \mathbf{p}_1, \mathbf{p}_2)$, and the spin-flavor operators w^Ω for the Fermi-Breit interaction. The quark pair $i, j = 1, 2$ is assumed. For the non-central terms, the angular-momentum coupling $U^T = \alpha^T 3\sqrt{10} [u^T w^T]^{(0)} w^C$ etc. should be taken.

Ω	α^Ω/α_S	u^Ω	w^Ω
CC	1	$\frac{4\pi}{k^2}$	1
MC	$\left(\frac{1}{m_{ud}}\right)^2$	$\frac{4\pi}{k^2} \left[\frac{1}{k^2} (\mathbf{k} \cdot \mathbf{p}_1)(\mathbf{k} \cdot \mathbf{p}_2) - (\mathbf{p}_1 \cdot \mathbf{p}_2) \right]$	$\frac{(m_{ud})^2}{m_1 m_2}$
GC	$-\pi \left(\frac{1}{m_{ud}}\right)^2$	1	$\frac{1}{2} \left[\left(\frac{m_{ud}}{m_1}\right)^2 + \left(\frac{m_{ud}}{m_2}\right)^2 \right] + \frac{2}{3} \frac{(m_{ud})^2}{m_1 m_2} (\boldsymbol{\sigma}_1 \cdot \boldsymbol{\sigma}_2)$
sLS	$\frac{3}{4} \left(\frac{1}{m_{ud}}\right)^2$	$\frac{4\pi}{k^2} i \left[\mathbf{k}, \frac{1}{2}(\mathbf{p}_1 - \mathbf{p}_2) \right]$	$\frac{1}{3} \left(\frac{m_{ud}}{m_1}\right)^2 \boldsymbol{\sigma}_1 + \frac{1}{3} \left(\frac{m_{ud}}{m_2}\right)^2 \boldsymbol{\sigma}_2 + \frac{2}{3} \frac{(m_{ud})^2}{m_1 m_2} (\boldsymbol{\sigma}_1 + \boldsymbol{\sigma}_2)$
aLS	$-\frac{1}{8} \left(\frac{1}{m_{ud}}\right)^2$	$\frac{4\pi}{k^2} i \left[\mathbf{k}, \mathbf{p}_1 + \mathbf{p}_2 \right]$	$-\left(\frac{m_{ud}}{m_1}\right)^2 \boldsymbol{\sigma}_1 + \left(\frac{m_{ud}}{m_2}\right)^2 \boldsymbol{\sigma}_2 + \frac{2(m_{ud})^2}{m_1 m_2} (\boldsymbol{\sigma}_1 - \boldsymbol{\sigma}_2)$
T	$\frac{1}{12} \left(\frac{1}{m_{ud}}\right)^2$	$\frac{4\pi}{k^2} \mathcal{Y}_{2\mu}(\mathbf{k})$	$\frac{(m_{ud})^2}{m_1 m_2} [\boldsymbol{\sigma}_1 \boldsymbol{\sigma}_2]_\mu^{(2)}$

It is specified by the number of exchanged quarks, $x = 0, 1$, and various interaction types, \mathcal{T} . More specifically, $x = 0$ with $z_0 = 1$ corresponds to the direct term (EMEP's only) and $x = 1$ with $z_1 = P_{36}$ the (one-quark) exchange term. The interaction types, $\mathcal{T} = E, S, S', D_+$ and D_- , correspond to some specific (i, j) pairs of quarks [56]. The spin-flavor-color factor $X_{x\mathcal{T}}$ is defined through

$$\begin{aligned} X_{x\mathcal{T}} &= C_x \langle z_x \xi | \sum_{i < j}^{\mathcal{T}} w_{ij} w_{ij}^C | \xi \rangle \\ &= \begin{cases} X_{0\mathcal{T}}^C \langle \xi^{SF} | \sum_{i < j}^{\mathcal{T}} w_{ij} | \xi^{SF} \rangle \\ (-9) X_{1\mathcal{T}}^C \langle P_{36} \xi^{SF} | \sum_{i < j}^{\mathcal{T}} w_{ij} | \xi^{SF} \rangle \end{cases} \quad \text{for } x = \begin{cases} 0 \\ 1 \end{cases}, \end{aligned} \quad (2.30)$$

where $C_0 = 1$ and $C_1 = -9$. The color-factors $X_{x\mathcal{T}}^C = \langle z_x \xi^C | w_{ij}^C | \xi^C \rangle$ for each $(i, j) \in \mathcal{T}$ are given as follows. For the quark sector with $w_{ij}^C = (1/4)(\lambda_i^C \cdot \lambda_j^C)$, $X_{0E}^C = -(2/3)$, $X_{0D_+}^C = 0$, and $X_{1E}^C = X_{0S}^C = X_{0S'}^C = -(2/9)$, $X_{1D_+}^C = 1/9$, $X_{1D_-}^C = 4/9$. For the EMEP sector with $w_{ij}^C = 1$, $X_{0\mathcal{T}}^C = 1$ and $X_{1\mathcal{T}}^C = 1/3$. The spin-flavor-color factor for the exchange normalization kernel is defined by $X_N = (-3) \langle P_{36} \xi^{SF} | \xi^{SF} \rangle$. We also need $X_K = 24 \langle P_{36} \xi^{SF} | Y_6 - Y_5 | \xi^{SF} \rangle$ with the hypercharge operator Y_i for the exchange kinetic-energy kernel of the YN systems.

To calculate the matrix elements in Eq. (2.30), it is convenient first to calculate three-quark matrix elements of various operators with respect to the [3]-symmetric and [21]-symmetric SU_6 wave functions. We need a small number of operators for this calculation, which are always expressed as composite operators of the two SU_6 unit vectors [49, 58]. After representing the spin-flavor factors in $(3q)$ -($3q$) system as operator products of these composite operators, we can evaluate the $(3q)$ -($3q$) matrix elements of these operator products, using a simple formula which combines the $(3q)$ matrix elements in various ways. The advantage of this method is that it is directly related to the straightforward separation of spin-isospin dependence of various non-central forces appearing in the $B_8 B_8$ interactions. The final results of some spin-flavor factors are already published in our previous papers. In the quark sector, the operator form of the spin-flavor factor is expressed as $X_{\mathcal{T}}^\Omega$, which is essentially $X_{1\mathcal{T}}^\Omega$ in Eq. (2.30) but has a slightly different numerical factor. The spin-flavor-color factors in the quark sector for the NN system are given in Eq. (B.6) of Ref. [31]. We should note that $X_{\mathcal{T}}$ there is actually $X_{\mathcal{T}}^{GC}$ for $\mathcal{T} = D_+$ and D_- , and $X_S^{GC} = X_{S'}^{GC} = -X_E$. (Note that X_E is not X_E^{GC} .) Furthermore, $X_{D_-}^{MC} = X_{D_+}^{MC} = X_N$, $X_S^{MC} = X_{S'}^{MC} = -2X_N$, $X_E^{MC} = -X_N$, and $X_K = 0$ for NN . The spin-orbit and tensor factors for YN systems are found in Appendix C of Ref. [59]. The one-quark exchange ($x = 1$) central factors $(X_{\mathcal{T}}^\Omega)_{B_3 N B_1 N}$ in the YN system with $Y = \Lambda, \Sigma$ and Ξ are given in Appendix B.3 of Ref. [44].

We define the Born kernel for the exchange kernel $\mathcal{M}_{\alpha\alpha'}(\mathbf{R}, \mathbf{R}'; E)$ in Eq. (2.16) as

$$\begin{aligned} M_{\alpha\alpha'}^B(\mathbf{q}_f, \mathbf{q}_i; E) &= \langle e^{i\mathbf{q}_f \cdot \mathbf{R}} | \mathcal{M}_{\alpha\alpha'}(\mathbf{R}, \mathbf{R}'; E) | e^{i\mathbf{q}_i \cdot \mathbf{R}'} \rangle \\ &= \sum_{\beta} \sum_{\Omega} M_{D\alpha\alpha'}^{\Omega\beta}(\mathbf{q}_f, \mathbf{q}_i) \mathcal{O}^\Omega(\mathbf{q}_f, \mathbf{q}_i) + \sum_{\Omega} M_{\alpha\alpha'}^\Omega(\mathbf{q}_f, \mathbf{q}_i) \mathcal{O}^\Omega(\mathbf{q}_f, \mathbf{q}_i) - \varepsilon_\alpha M_{\alpha\alpha'}^N(\mathbf{q}_f, \mathbf{q}_i) . \end{aligned} \quad (2.31)$$

Each component of the Born kernel is given in terms of the transferred momentum $\mathbf{k} = \mathbf{q}_f - \mathbf{q}_i$ and the local momentum $\mathbf{q} = (\mathbf{q}_f + \mathbf{q}_i)/2$. In Eq. (2.31) the space-spin invariants $\mathcal{O}^\Omega = \mathcal{O}^\Omega(\mathbf{q}_f, \mathbf{q}_i)$ are given by $\mathcal{O}^{central} = 1$ and

$$\begin{aligned} \mathcal{O}^{LS} &= i\mathbf{n} \cdot \mathbf{S}, \quad \mathcal{O}^{LS^{(-)}} = i\mathbf{n} \cdot \mathbf{S}^{(-)}, \quad \mathcal{O}^{LS^{(-)\sigma}} = i\mathbf{n} \cdot \mathbf{S}^{(-)} P_\sigma, \\ \text{with } \mathbf{n} &= [\mathbf{q}_i \times \mathbf{q}_f], \quad \mathbf{S} = \frac{1}{2}(\boldsymbol{\sigma}_1 + \boldsymbol{\sigma}_2), \quad \mathbf{S}^{(-)} = \frac{1}{2}(\boldsymbol{\sigma}_1 - \boldsymbol{\sigma}_2), \quad P_\sigma = \frac{1 + \boldsymbol{\sigma}_1 \cdot \boldsymbol{\sigma}_2}{2}. \end{aligned} \quad (2.32)$$

For the tensor and QLS parts, it is convenient to take four natural operators defined by

$$\mathcal{O}^T = S_{12}(\mathbf{k}, \mathbf{k}), \quad \mathcal{O}^{T'} = S_{12}(\mathbf{q}, \mathbf{q}), \quad \mathcal{O}^{T''} = S_{12}(\mathbf{k}, \mathbf{q}), \quad \mathcal{O}^{QLS} = S_{12}(\mathbf{n}, \mathbf{n}), \quad (2.33)$$

where $S_{12}(\mathbf{a}, \mathbf{b}) = (3/2)[(\boldsymbol{\sigma}_1 \cdot \mathbf{a})(\boldsymbol{\sigma}_2 \cdot \mathbf{b}) + (\boldsymbol{\sigma}_2 \cdot \mathbf{a})(\boldsymbol{\sigma}_1 \cdot \mathbf{b})] - (\boldsymbol{\sigma}_1 \cdot \boldsymbol{\sigma}_2)(\mathbf{a} \cdot \mathbf{b})$. The calculation of Eq. (2.31) is most easily carried out by using a special type of the transformation formula, developed in Appendix A of Ref. [44] for the systems of two $(0s)^3$ -clusters. This formula is particularly useful to calculate the Born kernel from the momentum-dependent two-body interaction. For the direct term of the static two-body interaction, this formula is reduced to the simple multiplication of the Gaussian form factor $F(\mathbf{k})^2 = e^{-(bk)^2/3}$ to the two-body interaction in the momentum representation. For the exchange term, the exchange normalization kernel is factored out. The formula is especially simple for the Gaussian interaction, but is also applicable to the Yukawa functions preserving the factorization property. The resultant Born kernel is expressed using generalized Dawson's integrals $\tilde{h}_n(x)$ and modified Yukawa functions $\tilde{\mathcal{Y}}_\alpha(x)$, $\tilde{\mathcal{Z}}_\alpha(x)$ etc., which are given by the error function of the imaginary argument. The momentum dependence of the two-body interaction appears as the polynomial terms in \mathbf{q} up to the second order. The direct Born kernel $M_{D\alpha\alpha'}^{\Omega\beta}(\mathbf{q}_f, \mathbf{q}_i)$ in the EMEP sector is shown below. The exchange Born kernel $M_{\alpha\alpha'}^{(\Omega)}(\mathbf{q}_f, \mathbf{q}_i)$ is given in Appendix B of Ref. [44] for the FB interaction and in Appendix A of Ref. [42] for the EMEP's.

The EMEP's at the quark level are most easily formulated in the momentum representation, by using the second-order perturbation theory with respect to the quark-baryon vertices. We employ the following qq interaction, which is obtained through the non-relativistic reduction of the one-boson exchange amplitudes in the parameter $\gamma = (m/2m_{ud})$ (where m is the exchanged meson mass and m_{ud} is the up-down quark mass):

$$\begin{aligned}
U^S(\mathbf{q}_f, \mathbf{q}_i) &= gg^\dagger \frac{4\pi}{\mathbf{k}^2 + m^2} \left(-1 + \frac{\mathbf{q}^2}{2m_{ud}^2} - \frac{1}{2m_{ud}^2} i\mathbf{n} \cdot \mathbf{S} \right), \\
U^{PS}(\mathbf{q}_f, \mathbf{q}_i) &= -ff^\dagger \frac{1}{m_{\pi^+}^2} \frac{4\pi}{\mathbf{k}^2 + m^2} \left[(\boldsymbol{\sigma}_i \cdot \mathbf{k})(\boldsymbol{\sigma}_j \cdot \mathbf{k}) - (1 - c_\delta)(m^2 + \mathbf{k}^2) \frac{1}{3} (\boldsymbol{\sigma}_i \cdot \boldsymbol{\sigma}_j) \right], \\
U^V(\mathbf{q}_f, \mathbf{q}_i) &= \frac{4\pi}{\mathbf{k}^2 + m^2} \left\{ f^e f^{e\dagger} \left(1 + \frac{3\mathbf{q}^2}{2m_{ud}^2} \right) - f^m f^{m\dagger} \frac{2}{(m_{ud}m)^2} \left[(\boldsymbol{\sigma}_i \cdot \mathbf{n})(\boldsymbol{\sigma}_j \cdot \mathbf{n}) \right. \right. \\
&\quad \left. \left. - (1 - c_{qss}) \frac{1}{3} \mathbf{n}^2 (\boldsymbol{\sigma}_i \cdot \boldsymbol{\sigma}_j) \right] - (f^m f^{e\dagger} + f^e f^{m\dagger}) \frac{2}{m_{ud}m} i\mathbf{n} \cdot \mathbf{S} \right\}. \quad (2.34)
\end{aligned}$$

Here the quark-meson coupling constants are expressed in the operator form in the flavor space [58, 59]. For example, the product of the two different coupling-constant operators g and f are expressed as

$$gf^\dagger = \begin{cases} g_1 f_1 \\ g_8 f_8 \Sigma_a \lambda_{ai} \lambda_{aj} \end{cases} \quad \text{for } \begin{cases} \text{singlet mesons} \\ \text{octet mesons} \end{cases}. \quad (2.35)$$

The meson mixing between the flavor-singlet and octet mesons is very important, implying

$$f_{\eta'} = f_1 \cos \theta + f_8 \sin \theta \lambda_8, \quad f_\eta = -f_1 \sin \theta + f_8 \cos \theta \lambda_8, \quad (2.36)$$

instead of f_1 and $f_8 \lambda_8$ in Eq. (2.35) for the PS mesons. A similar transformation is also applied to the S- and V-meson coupling constants. The SU_3 parameters of the EMEP coupling constants are therefore f_1 , f_8 and θ . The S-meson exchange EMEP in Eq. (2.34) involves not only the attractive leading term, but also the momentum-dependent \mathbf{q}^2 term and the LS term. In the PS-meson exchange operator, the parameter c_δ is introduced only for the one-pion exchange, in order to reduce the very strong effect of the delta-function type contact term involved in the spin-spin interaction. The case $c_\delta = 1$ corresponds to the full expression, while $c_\delta = 0$ corresponds to the case with no spin-spin contact term. The V-meson exchange potential is composed of the electric-type term, the magnetic-type term and the cross term. In the electric term, the central force generated by the ω -meson exchange potential

is usually most important, and it also includes the \mathbf{q}^2 -type momentum-dependent term. As to the introduction of the V-meson EMEP to the QM, the problem of double counting is addressed especially in the strong short-range repulsion from the ω meson [60]. We will not discuss this problem here, but avoid this double counting for the short-range repulsion and the LS force, by simply choosing appropriate coupling constants for V mesons, i.e., $f_1^{\text{Ve}}, f_1^{\text{Vm}} \sim 1$, and $f_8^{\text{Ve}} = 0$ (see Table 2). The magnetic term is usually important for the isovector ρ meson, and yields the spin-spin, tensor and QLS terms in the standard OBEP. The choice in Eq. (2.34) is to keep only the QLS term with the spin-spin term proportional to \mathbf{L}^2 , the reason for which is discussed below. Finally, the cross term between the electric and magnetic coupling constants leads to the LS force for the qq interaction. The antisymmetric LS ($LS^{(-)}$) force with $\mathbf{S} = (\boldsymbol{\sigma}_1 - \boldsymbol{\sigma}_2)/2$ is not generated from EMEP, because the flavor operator in Eq. (2.35) is the Gell-Mann matrix and also because the mass difference between the up-down and strange quarks is ignored in Eq. (2.34).

We should keep in mind that these EMEP's are by no means the consequences of the real meson-exchange processes taking place between the quarks. First of all, the static approximation used to derive the meson-exchange potentials between the quarks is not permissible, since the masses of S mesons and V mesons are more than twice as heavy as the quark mass $m_{ud} = 300 - 400 \text{ MeV}/c^2$. Since the parameter γ is not small, the non-relativistic reduction is not justified. Also, the very strong S-meson central attraction is just a replacement of the real processes of the 2π exchange, the $\pi\rho$ exchange, the Δ excitations and so forth. The V mesons are supposed to behave as composite particles of the $(q\bar{q})$ pairs. Furthermore, the choice of terms in Eq. (2.34) is quite *ad hoc* and phenomenological. We should consider Eq. (2.34) an effective interaction to simulate those residual interactions between the quarks which are not taken into account by the FB interaction. The full expression of the Born kernel Eq. (2.31) is lengthy, but the direct term from the EMEP's is simple enough to show the main characteristics of the EMEP's introduced in the present model:

$$\begin{aligned}
M_D^S(\mathbf{q}_f, \mathbf{q}_i) &= g^2 \frac{4\pi}{\mathbf{k}^2 + m^2} e^{-\frac{1}{3}(bk)^2} \left\{ X_{0D+}^C \left[-1 + \frac{1}{2(3m_{ud})^2} \left(\mathbf{q}^2 + \frac{9}{2b^2} \right) \right] - \frac{3}{2(3m_{ud})^2} X_{0D+}^{LS} i\mathbf{n} \cdot \mathbf{S} \right. \\
&\quad \left. - \frac{3}{2(3m_{ud})^2} X_{0D+}^{LS^{(-)}} i\mathbf{n} \cdot \mathbf{S}^{(-)} \right\}, \\
M_D^{\text{PS}}(\mathbf{q}_f, \mathbf{q}_i) &= -f^2 \frac{1}{m_{\pi+}^2} \frac{4\pi}{\mathbf{k}^2 + m^2} e^{-\frac{1}{3}(bk)^2} X_{0D+}^T \left[(\boldsymbol{\sigma}_1 \cdot \mathbf{k})(\boldsymbol{\sigma}_2 \cdot \mathbf{k}) - (1 - c_\delta)(m^2 + \mathbf{k}^2) \frac{1}{3}(\boldsymbol{\sigma}_1 \cdot \boldsymbol{\sigma}_2) \right], \\
M_D^{\text{V}}(\mathbf{q}_f, \mathbf{q}_i) &= \frac{4\pi}{\mathbf{k}^2 + m^2} e^{-\frac{1}{3}(bk)^2} \left\{ (f^e)^2 X_{0D+}^C \left[1 + \frac{3}{2(3m_{ud})^2} \left(\mathbf{q}^2 + \frac{9}{2b^2} \right) \right] \right. \\
&\quad - (f^m)^2 \frac{2}{(3m_{ud}m)^2} X_{0D+}^T \left[(\boldsymbol{\sigma}_1 \cdot \mathbf{n})(\boldsymbol{\sigma}_2 \cdot \mathbf{n}) - (1 - c_{qss}) \left(\frac{\mathbf{n}^2}{3} + \frac{\mathbf{k}^2}{b^2} \right) (\boldsymbol{\sigma}_1 \cdot \boldsymbol{\sigma}_2) \right. \\
&\quad \left. \left. + \frac{3}{2b^2} [\boldsymbol{\sigma}_1 \times \mathbf{k}] \cdot [\boldsymbol{\sigma}_2 \times \mathbf{k}] \right] - 2f^m f^e \frac{2}{3m_{ud}m} X_{0D+}^{LS} i\mathbf{n} \cdot \mathbf{S} - 2f^m f^e \frac{2}{3m_{ud}m} X_{0D+}^{LS^{(-)}} i\mathbf{n} \cdot \mathbf{S}^{(-)} \right\}. \quad (2.37)
\end{aligned}$$

Here X_{0D+}^Ω represents the spin-flavor factors related to the spin-flavor operators in Eq. (2.34). Besides the Gaussian factor $\exp\{-(bk)^2/3\}$ related to the $(0s)^3$ -cluster wave functions, the finite size effect of the baryons also appears as the constant zero-point oscillation terms accompanied with the \mathbf{q}^2 terms, which appear in the S- and V-meson contributions. For the QLS force, the same effect appears as the tensor force having the form $[\boldsymbol{\sigma}_1 \times \mathbf{k}] \cdot [\boldsymbol{\sigma}_2 \times \mathbf{k}]$. The magnitude of this term is about one third, compared to the original tensor term appearing at the level of the qq interaction. The advantage of using the QLS force in Eq. (2.34), instead of the tensor force, is that we can avoid the π - ρ cancellation of the tensor force for the coupling term of the S and D waves. The ε_1 parameter of the NN interaction is very sensitive to this coupling strength.

We have four QM parameters; the h.o. size parameter b for the $(3q)$ -clusters, the up-down quark mass m_{ud} , the strength of the quark-gluon coupling constant α_S , and the mass ratio of the strange to

up-down quarks $\lambda = (m_s/m_{ud})$. A reasonable range of the values for these parameters in the present framework is $b = 0.5 - 0.6$ fm, $m_{ud} = 300 - 400$ MeV/ c^2 , $\alpha_S \approx 2$, and $\lambda = 1.2 - 1.7$. Note that we are dealing with the constituent QM with explicit mesonic degree of freedom. The size of the system determined from the $(3q)$ wave function with b (the rms radius of the $(3q)$ system is equal to b) is related to the quark distribution, which determines the range in which the effect of the FB interaction plays an essential role through the quark-exchange kernel. The internal energies of the clusters should be calculated from the same Hamiltonian as used in the two-baryon system, and contain not only the quark contribution but also various EMEP contributions. The value of α_S is naturally correlated with b , m_{ud} , and other EMEP parameters. This implies that α_S is merely a parameter in our framework, and has very little to do with the real quark-gluon coupling constant of QCD. The quark and EMEP contributions to the baryon mass differences between N and Δ and between Λ and Σ , calculated in the isospin basis, is tabulated in Table III of Ref. [42].

For the EMEP part, we have three parameters f_1 , f_8 , and θ for each of the S, PS, Ve (vector-electric) and Vm (vector-magnetic) terms. The $F/(F + D)$ ratio is no longer a free parameter in the present framework, but takes the pure SU_6 values $\alpha_e = 1$ (for S and Ve) and $\alpha_m = 2/5$ (for PS and Vm). It is convenient to use the coupling constants at the baryon level, in order to compare our result with the predictions by other OBEP models. These are related to the coupling constants at the quark level used in Eqs. (2.34) and (2.37) through a simple relationship

$$\begin{aligned} f_1^S &= 3g_1 \quad , \quad f_8^S = g_8 \quad , \quad f_1^{PS} = f_1 \quad , \quad f_8^{PS} = \frac{5}{3}f_8 \quad , \\ f_1^{Ve} &= 3f_1^e \quad , \quad f_8^{Ve} = f_8^e \quad , \quad f_1^{Vm} = f_1^m \quad , \quad f_8^{Vm} = \frac{5}{3}f_8^m \quad . \end{aligned} \quad (2.38)$$

Through this replacement, the leading term for each meson in Eq. (2.37) precisely coincides with that of the OBEP with Gaussian form factors. In the present framework, the S-meson masses for ϵ , S^* , δ and κ , are also considered free parameters within some appropriate ranges, expected from some real mesons, $f_0(600)$ or σ , $f_0(980)$, $a_0(980)$ and $K_0^*(800)$ or κ , respectively. We further introduce three parameters to improve the fit of the NN phase shifts to the empirical data [42], c_δ the strength factor for the delta-function type spin-spin contact term of the one-pion exchange potential (OPEP), c_{qss} the strength factor for the spin-spin term of the QLS force, and c_{qT} the strength factor for the tensor term of the FB interaction.

We determine these parameters so as to fit the phase shift analysis SP99 [61] for the np scattering with the partial waves $J \leq 2$ and the incident energies $T_{lab} \leq 350$ MeV, under the constraint that the deuteron binding energy and the 1S_0 NN scattering length are reproduced. Some parameters are very sensitive to reproduce the available data for the low-energy YN total cross sections. In the parameter search, we minimize the χ^2 value defined as

$$\sqrt{\chi^2} = \left\{ \frac{1}{N} \sum_{i=1}^N (\delta_i^{\text{cal}} - \delta_i^{\text{exp}})^2 \right\}^{\frac{1}{2}} \quad , \quad (2.39)$$

where no experimental error bars are employed because they are not given in the energy-dependent solution of the phase-shift analysis. Here the sum over $i = 1 - N$ covers various angular momenta and energies, and the mixing parameters, ε_1 and ε_2 , in units of degree. The value $\sqrt{\chi^2}$ gives a measure for the deviation of the calculated phase shifts from the empirical values. The result of the parameter search is shown in Table 2. The parameters of the previous model FSS are also shown for comparison. The resultant χ^2 values are $\sqrt{\chi^2} \approx 3^\circ$ in FSS and $\sqrt{\chi^2} = 0.59^\circ$ in fss2 for the np scattering, when the energies $T_{lab} = 25, 50, 100, 150, 200, 300$ MeV and the partial waves up to $J = 2$ are employed.

Table 2: Quark-model parameters, SU_3 parameters of the EMEP's, S-meson masses, and some reduction factors c_δ etc. for the models fss2 and FSS. The ρ meson in fss2 is treated in the two-pole approximation, for which m_1 (β_1) and m_2 (β_2) are shown below the table.

	b (fm)	m_{ud} (MeV/ c^2)	α_S	$\lambda = m_s/m_{ud}$
fss2	0.5562	400	1.9759	1.5512
FSS	0.616	360	2.1742	1.526
	f_1^S	f_8^S	θ^S	$\theta_4^{S\ 1)}$
fss2	3.48002	0.94459	33.3295°	55.826°
FSS	2.89138	1.07509	27.78°	65°
	f_1^{PS}	f_8^{PS}	θ^{PS}	
fss2	—	0.26748	—	(no η, η')
FSS	0.21426	0.26994	−23°	
	f_1^{Ve}	f_8^{Ve}	f_1^{Vm}	$f_8^{Vm\ 2)}$
fss2	1.050	0	1.000	2.577
(MeV/ c^2)	m_ϵ	m_{S^*}	m_δ	m_κ
fss2	800	1250	846 ³⁾	936
FSS	800	1250	970	1145
	c_δ	c_{qss}	c_{qT} ⁵⁾	
fss2	0.4756 ⁴⁾	0.6352	3.139	
FSS	0.381	—	—	

- 1) θ_4^S is used only for $\Sigma N(I = 3/2)$.
- 2) $\theta^V = 35.264^\circ$ (ideal mixing) and two-pole ρ meson with m_1 (β_1) = 664.56 MeV/ c^2 (0.34687) and m_2 (β_2) = 912.772 MeV/ c^2 (0.48747) [62] are used.
- 3) For the NN system, $m_\delta = 720$ MeV/ c^2 is used.
- 4) Only for π , otherwise 1.
- 5) The enhancement factor for the Fermi-Breit tensor term.

2.3 The Lippmann-Schwinger formalism for (3q)-(3q) RGM and the G -matrix equation

As mentioned in the Introduction, the RGM equation (2.15) is solved in the momentum representation. The basic LS-RGM equation is given by

$$T_{\gamma\alpha}(\mathbf{p}, \mathbf{q}; E) = V_{\gamma\alpha}(\mathbf{p}, \mathbf{q}; E) + \sum_{\beta} \frac{1}{(2\pi)^3} \int d\mathbf{k} V_{\gamma\beta}(\mathbf{p}, \mathbf{k}; E) \frac{2\mu_{\beta}}{\hbar^2} \frac{1}{k_{\beta}^2 - k^2 + i\epsilon} T_{\beta\alpha}(\mathbf{k}, \mathbf{q}; E), \quad (2.40)$$

where the quasipotential $V_{\gamma\beta}(\mathbf{p}, \mathbf{q}; E)$ is calculated from the basic Born kernel (2.31) through

$$V_{\gamma\alpha}(\mathbf{k}, \mathbf{k}'; E) = \frac{1}{2} \left[M_{\gamma\alpha}^B(\mathbf{k}, \mathbf{k}'; E) + (-1)^{S_\alpha} \mathcal{P}_\alpha M_{\gamma\alpha}^B(\mathbf{k}, -\mathbf{k}'; E) \right]. \quad (2.41)$$

Using the partial wave decomposition of the LS-RGM equation [44], we introduce the definition

$$T_{\gamma\alpha}(\mathbf{k}, \mathbf{k}'; E) = \sum_{JM\ell\ell'}' 4\pi T_{\gamma S'\ell', \alpha S\ell}^J(k, k'; E) \sum_{mm'} \langle \ell' m' S' S'_z | JM \rangle \langle \ell m S S_z | JM \rangle Y_{\ell' m'}(\hat{\mathbf{k}}) Y_{\ell m}^*(\hat{\mathbf{k}}'), \quad (2.42)$$

where $\gamma = [1/2(11)c_1, 1/2(11)c_2] S' S'_z Y_{II} I_z; \mathcal{P}'$. The prime on the summation symbol indicates that ℓ and ℓ' are limited to such values that satisfy the condition $(-1)^\ell = (-1)^{S\mathcal{P}}$ and $(-1)^{\ell'} = (-1)^{S'\mathcal{P}'}$. We write the spin quantum numbers S and S' of the T -matrix explicitly for the later convenience, although these are already included in the definition of α and γ . The LS-RGM equation is reduced to

$$T_{\gamma S' \ell', \alpha S \ell}^J(p, q; E) = V_{\gamma S' \ell', \alpha S \ell}^J(p, q; E) + \sum_{\beta S'' \ell''}' \frac{4\pi}{(2\pi)^3} \int_0^\infty k^2 dk V_{\gamma S' \ell', \beta S'' \ell''}^J(p, k; E) \\ \times \frac{2\mu_\beta}{\hbar^2} \frac{1}{k_\beta^2 - k^2 + i\varepsilon} T_{\beta S'' \ell'', \alpha S \ell}^J(k, q; E), \quad (2.43)$$

where $E = E_\beta^{\text{int}} + (\hbar^2/2\mu_\beta)k_\beta^2$ and $V_{\gamma S' \ell', \alpha S \ell}^J(p, q; E)$ is the partial-wave decomposition of $V_{\gamma\alpha}(\mathbf{p}, \mathbf{q}; E)$. We use the Gauss-Legendre 20-point quadrature formula to carry out the numerical integration. The Lippmann-Schwinger equation (2.43) involves a pole at $k = k_\beta$ in the Green function. A proper treatment of such a singularity for positive energies is well known. Here we use the technique developed by Noyes [53] and Kowalski [54], and separate the momentum region of k (and also p and q) into two parts. After eliminating the singularity, we carry out the integral over $0 \leq k \leq k_\beta$ by the Gauss-Legendre 15-point quadrature formula, and the integral over $k_\beta \leq k < \infty$ by using the Gauss-Legendre 20-point quadrature formula through the mapping, $k = k_\beta + \tan[(\pi/4)(1+x)]$.

Once we obtain the phase shift parameters for all the partial waves, it is straightforward to calculate the scattering amplitude, which is defined by the on-shell T -matrix through

$$M_{\gamma\alpha}(\mathbf{q}_f, \mathbf{q}_i; E) = -\frac{\sqrt{\mu_\gamma \mu_\alpha q_f q_i}}{2\pi \hbar^2} T_{\gamma\alpha}(\mathbf{q}_f, \mathbf{q}_i; E). \quad (2.44)$$

Here \mathbf{q}_f and \mathbf{q}_i are related to the total energy E by the on-shell condition $E = E_\gamma^{\text{int}} + \varepsilon_\gamma = E_\alpha^{\text{int}} + \varepsilon_\alpha$ with $\varepsilon_\gamma = (\hbar^2/2\mu_\gamma)q_f^2$ and $\varepsilon_\alpha = (\hbar^2/2\mu_\alpha)q_i^2$. For the calculation of the polarization observables, it is customary to write the scattering amplitude Eq. (2.44) in the invariant form with respect to the space-spin operators. In the YN scattering, the three basic vectors, $\mathbf{k} = \mathbf{q}_f - \mathbf{q}_i$, $\mathbf{q} = (\mathbf{q}_f + \mathbf{q}_i)/2$ and $\mathbf{n} = [\mathbf{q}_i \times \mathbf{q}_f] = [\mathbf{q} \times \mathbf{k}]$ are not mutually orthogonal. We therefore use $\mathbf{k} = \mathbf{q}_f - \mathbf{q}_i$, $\mathbf{n} = [\mathbf{q} \times \mathbf{k}]$ and $\mathbf{P} = [\mathbf{k} \times \mathbf{n}] = \mathbf{k}^2 \mathbf{q} - (\mathbf{k} \cdot \mathbf{q})\mathbf{k}$ to define the invariant amplitudes:

$$M(\mathbf{q}_f, \mathbf{q}_i; E) = g_0 + h_0 i(\boldsymbol{\sigma}_1 + \boldsymbol{\sigma}_2) \cdot \hat{\mathbf{n}} + h_- i(\boldsymbol{\sigma}_1 - \boldsymbol{\sigma}_2) \cdot \hat{\mathbf{n}} + h_n (\boldsymbol{\sigma}_1 \cdot \hat{\mathbf{n}}) \cdot (\boldsymbol{\sigma}_2 \cdot \hat{\mathbf{n}}) \\ + h_k (\boldsymbol{\sigma}_1 \cdot \hat{\mathbf{k}}) \cdot (\boldsymbol{\sigma}_2 \cdot \hat{\mathbf{k}}) + h_P (\boldsymbol{\sigma}_1 \cdot \hat{\mathbf{P}}) \cdot (\boldsymbol{\sigma}_2 \cdot \hat{\mathbf{P}}) + f_+ \left\{ (\boldsymbol{\sigma}_1 \cdot \hat{\mathbf{k}})(\boldsymbol{\sigma}_2 \cdot \hat{\mathbf{P}}) + (\boldsymbol{\sigma}_1 \cdot \hat{\mathbf{P}})(\boldsymbol{\sigma}_2 \cdot \hat{\mathbf{k}}) \right\} \\ + f_- \left\{ (\boldsymbol{\sigma}_1 \cdot \hat{\mathbf{k}})(\boldsymbol{\sigma}_2 \cdot \hat{\mathbf{P}}) - (\boldsymbol{\sigma}_1 \cdot \hat{\mathbf{P}})(\boldsymbol{\sigma}_2 \cdot \hat{\mathbf{k}}) \right\}. \quad (2.45)$$

The eight invariant amplitudes, g_0, \dots, f_- , are complex functions of the total energy E and the scattering angle, $\cos \theta = (\hat{\mathbf{q}}_i \cdot \hat{\mathbf{q}}_f)$. Three of the eight invariant amplitudes, h_- , f_+ and f_- , do not appear for the NN scattering due to the identity of two particles (h_- and f_-) and the time-reversal invariance (f_- and f_+). These three terms correspond to the non-central forces characteristic in the YN scattering; i.e., h_- corresponds to $LS^{(-)}$, f_+ to $S_{12}(\mathbf{r}, \mathbf{p})$, and f_- to $LS^{(-)}\sigma$, respectively [59]. In particular, the antisymmetric LS interactions, $LS^{(-)}$ and $LS^{(-)}\sigma$, involve the spin change between 0 and 1, together with the transition of the flavor-exchange symmetry $\mathcal{P} \neq \mathcal{P}'$. In the NN scattering this process is not allowed, since the flavor-exchange symmetry is uniquely specified by the conserved isospin: $\mathcal{P} = (-1)^{1-I}$. On the contrary, these interactions are in general all possible in the YN scattering, which gives an intriguing interplay of non-central forces.

The invariant amplitudes are expressed by the S -matrix elements through the partial-wave decomposition of the scattering amplitude Eq. (2.44). Expressing the invariant amplitudes as

$$M_{\gamma\alpha}(\mathbf{q}_f, \mathbf{q}_i; E) = \sum_{JM \ell \ell'}' 4\pi R_{\gamma S' \ell', \alpha S \ell}^J \sum_{mm'} \langle \ell' m' S' S'_z | JM \rangle \langle \ell m S S_z | JM \rangle Y_{\ell' m'}(\hat{\mathbf{q}}_f) Y_{\ell m}^*(\hat{\mathbf{q}}_i), \quad (2.46)$$

we obtain the partial-wave component $R_{\gamma S' \ell', \alpha S \ell}^J = (1/2i)(S_{\gamma S' \ell', \alpha S \ell}^J - \delta_{\gamma, \alpha} \delta_{S', S} \delta_{\ell', \ell})$ as follows:

$$R_{\gamma S' \ell', \alpha S \ell}^J = -\frac{\sqrt{\mu_\gamma \mu_\alpha q_f q_i}}{2\pi \hbar^2} T_{\gamma S' \ell', \alpha S \ell}^J(q_f, q_i; E) . \quad (2.47)$$

The formulas given in Appendix D of Ref. [44] are then used to reconstruct the invariant amplitudes by the solution of the LS-RGM equation (2.43). All the scattering observables are expressed in terms of these invariant amplitudes. For example, the differential cross section and the polarization of the scattered particle are given by

$$\begin{aligned} \frac{d\sigma}{d\Omega} &\equiv \sigma_0(\theta) = |g_0|^2 + |h_0 + h_-|^2 + |h_0 - h_-|^2 + |h_n|^2 + |h_k|^2 + |h_P|^2 + |f_+ + f_-|^2 + |f_+ - f_-|^2 , \\ P(\theta) &= 2 \operatorname{Im} [g_0(h_0 + h_-)^* + h_n(h_0 - h_-)^*] + 2 \operatorname{Im} [h_k(f_+ - f_-)^* - h_P(f_+ + f_-)^*] . \end{aligned} \quad (2.48)$$

The LS-RGM equation (2.40) is readily extended to the G -matrix equation by a replacement of the free propagator with the ratio of the angle-averaged Pauli operator and the energy denominator:

$$G_{\gamma\alpha}(\mathbf{p}, \mathbf{q}; K, \omega) = V_{\gamma\alpha}(\mathbf{p}, \mathbf{q}; E) + \sum_{\beta} \frac{1}{(2\pi)^3} \int d\mathbf{k} V_{\gamma\beta}(\mathbf{p}, \mathbf{k}; E) \frac{Q_{\beta}(k, K)}{e_{\beta}(k, K; \omega)} G_{\beta\alpha}(\mathbf{k}, \mathbf{q}; K, \omega) . \quad (2.49)$$

A detailed description of this formalism is given in Ref. [45]. The formula to calculate the Scheerbaum factor [63] for the s.p. spin-orbit potential from the G -matrix solution is given in Ref. [46]. The energy dependence of the quasipotential $V_{\gamma\alpha}(\mathbf{p}, \mathbf{q}; E)$ in Eq. (2.49) is dealt with as follows. The total energy of the two interacting particles in the nuclear medium is not conserved. Since we only need the diagonal G -matrices to calculate s.p. potentials and the nuclear-matter properties in the lowest-order Brueckner theory, we simply use $\varepsilon_{\gamma} = E_a^{\text{int}} - E_c^{\text{int}} + (\hbar^2/2\mu_{\alpha})q^2$ both in $V_{\gamma\alpha}(\mathbf{p}, \mathbf{q}; E)$ and $V_{\gamma\beta}(\mathbf{p}, \mathbf{k}; E)$ in Eq. (2.49). The meaning and the adequacy of this procedure are discussed in Ref. [55] in a simple model.

Calculations in the isospin basis is sufficient to obtain the main characteristics of the baryon-baryon interactions. For more detailed investigations of the CSB etc., we also solve the LS-RGM equation (2.43) in the particle basis to incorporate the pion-Coulomb correction. We use the empirical baryon masses and evaluate spin-flavor factors for the charged pions and the neutral pion separately. The other spin-flavor factors for heavier mesons and the FB interaction are generated from those in the isospin basis through the simple isospin relations. The Coulomb force is introduced at the quark level by using the quark charges. The exchange Coulomb kernel has the same structure as the color-Coulombic term of the FB interaction. All the necessary expressions for the spatial integrals are given in Ref. [42].

The standard technique by Vincent and Phatak [64] is employed to solve the Lippmann-Schwinger equation with the Coulomb force in the momentum representation. This technique requires the introduction of a cut-off radius R_C for the Coulomb interaction. In the RGM formalism, we have to introduce this cut-off at the quark level, in order to avoid the violation of the Pauli principle. The two-body Coulomb force assumed in the present calculation is therefore written as

$$U_{ij}^{CL} = Q_i Q_j e^2 \frac{1}{r_{ij}} \Theta(R_C - r_{ij}) , \quad (2.50)$$

where Q_i is the charge of the quark i in units of e , and Θ the Heaviside step function. The Coulomb contribution to the internal energies becomes zero for the positive charged particles like the proton and Σ^+ . The direct Coulomb potential is given by

$$V_D(R) = Z_1 Z_2 e^2 \frac{1}{r} \left\{ \operatorname{erf}(\beta R) - \frac{1}{2} [\operatorname{erf}(\beta(R + R_C)) + \operatorname{erf}(\beta(R - R_C))] \right\} , \quad (2.51)$$

where $Z_i e$ ($i = 1, 2$) is the charge of each baryon, $\beta = \sqrt{3}/(2b)$, and $\text{erf}(x) = (2/\sqrt{\pi}) \int_0^x e^{-t^2} dt$ stands for the error function. The exchange Coulomb kernel is also slightly modified from the pure Coulomb kernel. Note that, even in the np and nn systems, we have small contributions from the Coulomb interaction through the exchange Coulomb kernel. The value R_C should be sufficiently large to be free from any nuclear effect beyond R_C . Then the final S -matrix is calculated from the condition that the wave function obtained by solving the Lippmann-Schwinger equation with the cut-off Coulomb force is smoothly connected to the asymptotic Coulomb wave function. In principle, this procedure is correct only when the direct Coulomb potential has a sharp cut-off. We have developed a new method [65] which can be applied even when the cut-off is not sharp like Eq. (2.51). In this method, we introduce two extra radii R_{in} and R_{out} , which satisfy $R_{\text{in}} < R_C < R_{\text{out}}$. We choose R_{out} such that the direct Coulomb potential Eq. (2.51) becomes negligibly small for $r > R_{\text{out}}$. On the other hand, R_{in} is selected such that the Coulomb wave functions are approximately local solutions of Eq. (2.51), avoiding the effects of the nuclear force and the smooth transition of the cut-off effect. We solve a local-potential problem of Eq. (2.51) from R_{out} to R_{in} , and prepare two independent modified plane waves, $\tilde{u}_\ell(k, R_{\text{in}})$ and $\tilde{v}_\ell(k, R_{\text{in}})$. The standard procedure by Vincent and Phatak can now be applied to the S -matrix of the LS-RGM equation by using these $\tilde{u}_\ell(k, R_{\text{in}})$, $\tilde{v}_\ell(k, R_{\text{in}})$, in order to obtain the nuclear S -matrix with the Coulomb effect. We find that this procedure gives quite accurate result within the difference of less than 0.1 degree, unless the incident energies are extremely small. For the practical calculations, we have chosen $R_{\text{in}} - R_C - R_{\text{out}} = 6 - 8 - 12$ fm.

For the YN interaction, more consideration is required for the treatment of the threshold energies. Here we use the non-relativistic expressions for the threshold energies in the calculations with the isospin basis, while in those with the particle basis the relativistic kinematics is employed. We note that the mass difference of Σ^- and Σ^+ is about 8 MeV and is fairly large. The Λp system has the total charge $Z = 1$ and the $\Sigma^- p$ system $Z = 0$. In the YN systems, the direct Coulomb term exists only in the $\Sigma^+ p$ channel and the $\Sigma^- p$ channel. In calculating the EMEP contribution to the masses of the Σ isospin multiplet, we find a large cancellation between the neutral and charged pion contributions. In general, the pion-Coulomb correction is not sufficient to reproduce the empirical mass difference of various B_8 isospin multiplets. The disagreement of the calculated threshold energies with the empirical values is a common feature of any microscopic models. Fortunately, we have a nice method to remedy this flaw without violating the Pauli principle. As discussed in Sect. 2.1 and in Ref. [55], we only need to add a small correction term ΔG to the exchange kernel, in order to use the empirical threshold energies. The same technique is also applied to the reduced mass corrections.

2.4 Three-cluster Faddeev formalism using two-cluster RGM kernels

To apply realistic QM baryon-baryon interactions to few-baryon systems such as the hypertriton, we have to find a basic three-cluster equation formulated using microscopic two-cluster quark-exchange kernel of the RGM. This is non-trivial not only because the quark-exchange kernel is non-local and energy dependent, but also because RGM equations sometimes involve redundant components due to the effect of the antisymmetrization, the Pauli-forbidden states. Here we propose a simple three-cluster equation, which is similar to the three-cluster orthogonality condition model (OCM) [66], but employs the two-cluster RGM kernel as the interaction potential [67]. The three-cluster Pauli-allowed space is constructed by the orthogonality of the total wave functions to the pairwise Pauli-forbidden states. Although this definition of the three-cluster Pauli-allowed space is not exactly equivalent to the standard definition given by the three-cluster normalization kernel, this condition of the orthogonality is essential to achieve the equivalence of the proposed three-cluster equation and the Faddeev equations which employ a singularity-free T -matrix derived from the RGM kernel (the RGM T -matrix) [67].

Let us first consider a simple system composed of three identical spinless clusters, interacting via the two-cluster RGM kernel $V^{\text{RGM}}(\varepsilon) = V_D + G + \varepsilon K$. We assume that there is only one Pauli-forbidden

state $|u\rangle$ for each pair of the clusters, satisfying $K|u\rangle = |u\rangle$. Using the equivalence of Eq. (2.19) to Eq. (2.20), we can separate $V^{\text{RGM}}(\varepsilon)$ into two distinct parts as

$$V^{\text{RGM}}(\varepsilon) = V(\varepsilon) + v(\varepsilon) , \quad (2.52)$$

where

$$\begin{aligned} V(\varepsilon) &= (\varepsilon - H_0) - \Lambda(\varepsilon - H_0)\Lambda = \varepsilon|u\rangle\langle u| + \Lambda H_0\Lambda - H_0 , \\ v(\varepsilon) &= \Lambda V^{\text{RGM}}(\varepsilon)\Lambda = \Lambda (V_D + G + \varepsilon K) \Lambda . \end{aligned} \quad (2.53)$$

Note that $\Lambda V(\varepsilon)\Lambda = 0$ and $\Lambda v(\varepsilon)\Lambda = v(\varepsilon)$; namely, $v(\varepsilon)$ represents the net effect of $V^{\text{RGM}}(\varepsilon)$ in the Pauli-allowed space. Using these properties, we can express Eq. (2.19) or Eq. (2.20) as

$$\Lambda [\varepsilon - H_0 - v(\varepsilon)] \Lambda \chi = 0 . \quad (2.54)$$

The separation of $V^{\text{RGM}}(\varepsilon)$ in Eq. (2.52) enables us to deal with the energy dependence of the exchange RGM kernel independently in the Pauli-forbidden space and in the allowed space. Let us generalize Eq. (2.52) to

$$\mathcal{V}(\omega, \varepsilon) = V(\omega) + v(\varepsilon) . \quad (2.55)$$

We will see that the energy dependence involved in $V(\omega)$ can be eliminated by the orthogonality condition to the Pauli-forbidden state. Since the direct application of the T -matrix formalism to Eq. (2.19) leads to a singular off-shell T -matrix [55], we first consider the subsidiary equation

$$[\omega - H_0 - V^{\text{RGM}}(\varepsilon)] \chi = 0 , \quad (2.56)$$

with $\omega \neq \varepsilon$, and extract a singularity-free off-shell T -matrix starting from the standard T -matrix formulation for the “potential” $V^{\text{RGM}}(\varepsilon)$. A formal solution of the T -matrix equation

$$T(\omega, \varepsilon) = V^{\text{RGM}}(\varepsilon) + V^{\text{RGM}}(\varepsilon)G_0^{(+)}(\omega)T(\omega, \varepsilon) \quad (2.57)$$

with $G_0^{(+)}(\omega) = 1/(\omega - H_0 + i0)$ is given by

$$\begin{aligned} T(\omega, \varepsilon) &= \tilde{T}(\omega, \varepsilon) + (\omega - H_0)|u\rangle \frac{1}{\omega - \varepsilon} \langle u|(\omega - H_0) , \\ \tilde{T}(\omega, \varepsilon) &= T_v(\omega, \varepsilon) - \left[1 + T_v(\omega, \varepsilon)G_0^{(+)}(\omega) \right] |u\rangle \frac{1}{\langle u|G_v^{(+)}(\omega, \varepsilon)|u\rangle} \langle u| \left[1 + G_0^{(+)}(\omega)T_v(\omega, \varepsilon) \right] , \end{aligned} \quad (2.58)$$

where $T_v(\omega, \varepsilon)$ is defined by

$$T_v(\omega, \varepsilon) = v(\varepsilon) + v(\varepsilon)G_0^{(+)}(\omega)T_v(\omega, \varepsilon) . \quad (2.59)$$

The basic relationship, necessary for deriving the Faddeev equations of composite particles, is

$$G_0^{(+)}(\omega)T(\omega, \varepsilon) = G_0^{(+)}(\omega)\tilde{T}(\omega, \varepsilon) + |u\rangle \frac{1}{\omega - \varepsilon} \langle u|(\omega - H_0) , \quad (2.60)$$

with

$$G_0^{(+)}(\omega)\tilde{T}(\omega, \varepsilon) = G_\Lambda^{(+)}(\omega, \varepsilon)\mathcal{V}(\omega, \varepsilon) - |u\rangle\langle u| . \quad (2.61)$$

Here $G_\Lambda^{(+)}(\omega, \varepsilon)$ is given by

$$G_\Lambda^{(+)}(\omega, \varepsilon) = G_v^{(+)}(\omega, \varepsilon) - G_v^{(+)}(\omega, \varepsilon)|u\rangle \frac{1}{\langle u|G_v^{(+)}(\omega, \varepsilon)|u\rangle} \langle u|G_v^{(+)}(\omega, \varepsilon) , \quad (2.62)$$

with $G_v^{(+)}(\omega, \varepsilon) = 1/(\omega - H_0 - v(\varepsilon) + i0)$. The full T -matrix $T(\omega, \varepsilon)$ in Eq. (2.58) is singular at $\varepsilon = \omega$, while $\tilde{T}(\omega, \varepsilon)$ does not have such a singularity. For $\varepsilon \neq \omega$, $T(\omega, \varepsilon)$ satisfies the relationship

$$\langle u | G_0^{(+)}(\omega) T(\omega, \varepsilon) | \phi \rangle = \langle \phi | T(\omega, \varepsilon) G_0^{(+)}(\omega) | u \rangle = 0 \quad (2.63)$$

for the plane wave solution $|\phi\rangle$ with the energy ε , i.e., $(\varepsilon - H_0)|\phi\rangle = 0$. This is a direct consequence of more general relationship

$$\langle u | \left[1 + G_0^{(+)}(\omega) \tilde{T}(\omega, \varepsilon) \right] = 0 \quad , \quad \left[1 + \tilde{T}(\omega, \varepsilon) G_0^{(+)}(\omega) \right] | u \rangle = 0 \quad , \quad (2.64)$$

which follows from Eq. (2.61).

The three-body equation with the pairwise orthogonality conditions is expressed as

$$P \left[E - H_0 - V_\alpha^{\text{RGM}}(\varepsilon_\alpha) - V_\beta^{\text{RGM}}(\varepsilon_\beta) - V_\gamma^{\text{RGM}}(\varepsilon_\gamma) \right] P \Psi = 0 \quad , \quad (2.65)$$

where H_0 is the free three-body kinetic-energy operator and $V_\alpha^{\text{RGM}}(\varepsilon_\alpha)$ stands for the RGM kernel Eq. (2.52) for the α -pair, etc. The operator P projects on the Pauli-allowed space with $[3]$ symmetry [66]. More precisely, we solve the eigenvalue problem

$$\sum_\alpha |u_\alpha\rangle \langle u_\alpha| \Psi_\lambda \rangle = \lambda |\Psi_\lambda\rangle \quad (2.66)$$

in the model space with $[3]$ symmetry, $|\Psi_\lambda\rangle \in [3]$, and define P as

$$P = \sum_{\lambda=0} |\Psi_\lambda\rangle \langle \Psi_\lambda| \quad . \quad (2.67)$$

The two-cluster relative energy ε_α in the three-cluster system is self-consistently determined through

$$\varepsilon_\alpha = \langle P \Psi | h_\alpha + V_\alpha^{\text{RGM}}(\varepsilon_\alpha) | P \Psi \rangle \quad , \quad (2.68)$$

using the normalized three-cluster wave function $P\Psi$ with $\langle P\Psi | P\Psi \rangle = 1$. Here h_α is the free kinetic-energy operator for the α -pair. Expressing $P\Psi = \psi_\alpha + \psi_\beta + \psi_\gamma$ with the Faddeev components ψ_α etc., we can derive the Faddeev equations [67]

$$\psi_\alpha = G_0^{(+)}(E) \tilde{T}_\alpha^{(3)}(E, \varepsilon_\alpha) (\psi_\beta + \psi_\gamma) \quad . \quad (2.69)$$

Note that $\tilde{T}_\alpha^{(3)}(E, \varepsilon_\alpha)$ is essentially the non-singular part of the two-cluster RGM T -matrix Eq. (2.58):

$$\tilde{T}_\alpha^{(3)}(E, \varepsilon_\alpha) = \tilde{T}_\alpha(E - h_{\bar{\alpha}}, \varepsilon_\alpha) \quad , \quad (2.70)$$

and that the solution of Eq. (2.69) automatically satisfies $\langle u_\alpha | \psi_\alpha + \psi_\beta + \psi_\gamma \rangle = 0$ due to Eq. (2.64). Since we can also derive Eq. (2.65) from Eq. (2.69), these two equations are completely equivalent.

This three-cluster Faddeev formalism is applied in Ref. [67] to a toy model composed of three di-neutrons ($3d'$) and a more realistic model composed of three α -clusters. The di-neutron clusters are described with $(0s)^2$ h.o. wave functions with $\nu = 0.12 \text{ fm}^{-2}$ and a Serber-type Gaussian interaction is assumed between two neutrons. The Pauli-forbidden state between the two di-neutrons is an $N = 0$ ($0s$) state, where N is the total h.o. quanta for the relative motion. We adjusted the strength of the two neutron interaction such that $2d'$ has a zero-energy bound state, and obtained a $3d'$ bound state of about $E_{3d'} \approx -0.5 \text{ MeV}$. Using the self-consistent procedure for the energy parameter ε in the $d'd'$ RGM kernel, we have obtained a complete agreement between this Faddeev calculation and a variational calculation in terms of the translationally invariant h.o. basis.

In the 3α system, the structure of the 2α normalization kernel K is not that simple. The eigenvalue γ_N for K is given by $\gamma_N = 2^{2-N} - 3\delta_{N,0}$ for the even N . In the relative S -wave we have two Pauli-forbidden states, $(0s)$ and $(1s)$, while in the D -wave only one $(0d)$ h.o. state is forbidden. The relative motion between the two α -clusters starts from $N = 4$ h.o. quanta. The large value $\gamma_4 = 1/4$ in the Pauli-allowed space makes the self-consistent procedure through Eq. (2.68) very important. Because of this rather involved structure of the 2α Pauli-forbidden states, the Faddeev equations of the 3α system allow the existence of the redundant or trivial solutions in the Faddeev equation (2.69) [68]. These redundant solutions are generated from solving the overlap eigenvalue equation for the rearrangement

$$\langle u|S|uf^\tau\rangle = \tau|f^\tau\rangle, \quad (2.71)$$

where S is the permutation operator $S = (123) + (123)^2$ and $|uf^\tau\rangle = |u\rangle|f^\tau\rangle$ is a product of two functions corresponding to the two momentum Jacobi-coordinate vectors, \mathbf{k} and \mathbf{q} , respectively. The eigenstate with $\tau = -1$ gives a Faddeev component $\psi_0^\tau = G_0|uf^\tau\rangle$, which gives a vanishing total wave function $P\Psi = (1 + S)\psi^\tau = 0$ but satisfies the Faddeev equation (2.69) owing to the orthogonality relations of the RGM T -matrix Eq. (2.64). In the 3α system with the total angular momentum $L = 0$, we have two such solutions with $\tau = -1$. In spite of this complexity, we can eliminate these redundant components by slightly modifying the Faddeev equation in Eq. (2.69). For details, Ref. [68] should be referred to. Comparison between the Faddeev calculation and the variational calculation in the h.o. basis was carried out in the same condition, incorporating the cut-off Coulomb force with $R_C = 10$ fm. For the two-body effective interaction, we use the three-range Minnesota force [69] with the Majorana exchange mixture $u = 0.94687$. The h.o. width parameter, $\nu = 0.257 \text{ fm}^{-2}$, is assumed for the $(0s)^4$ α -clusters. The $\alpha\alpha$ phase shifts are nicely reproduced in the $\alpha\alpha$ RGM calculation, using this effective NN force. We have obtained $E_{3\alpha} = -9.592 \text{ MeV}$, $\varepsilon = 13.481 \text{ MeV}$, and $c_{(04)} = 0.971$, by taking the partial waves up to $\lambda = 8$ in the Faddeev calculation [70]. Here $c_{(04)}$ is the amplitude of the lowest shell-model component with the SU_3 (04) representation. The corresponding variational calculation using up to $N = 60$ h.o. quanta yields $E_{3\alpha} = -9.594 \text{ MeV}$, $\varepsilon = 13.480 \text{ MeV}$, and $c_{(04)} = 0.971$, which implies that the difference is only 1 - 2 keV. We have also compared the present Faddeev calculations of the 3α system with the fully microscopic 3α RGM or GCM calculations, using various NN effective forces [71]. We find that the present 3α ground-state energies are only 1.5 - 1.8 MeV higher than those of the microscopic calculations. This implies that the genuine three-cluster exchange effect, which is neglected in the present three-cluster formalism, is attractive in nature, and is not repulsive claimed in many semi-microscopic 3α models. Oryu *et al.* carried out 3α Faddeev calculation using 2α RGM kernel [72]. They obtained very large binding energy, $-E_{3\alpha} = 28.2 \text{ MeV}$ with no Coulomb force. Since the effect of the Coulomb force is at most 6 MeV, this 3α binding energy is extremely large. This may result from that they did not treat the εK term in the RGM kernel properly, and that the Pauli-forbidden components are not exactly eliminated.

The present three-cluster Faddeev formalism is also applied to the three-cluster OCM in Ref. [73]. For this application, we only need to replace $V^{\text{RGM}}(\varepsilon)$ in Eq. (2.52) with

$$V^{\text{OCM}}(\varepsilon) = \varepsilon|u\rangle\langle u| + \Lambda (h_0 + V^{\text{eff}}) \Lambda - h_0, \quad (2.72)$$

where h_0 is the free two-cluster kinetic-energy operator and V^{eff} is an appropriate effective potential which reproduces the properties of the two-cluster system. If the Pauli-forbidden state $|u\rangle$ is a real bound state of V^{eff} , satisfying $(\varepsilon_B - h_0 - V^{\text{eff}})|u_B\rangle = 0$, Eq. (2.72) is further simplified to

$$V^{\text{OCM}}(\varepsilon) = V^{\text{eff}} + (\varepsilon - \varepsilon_B)|u_B\rangle\langle u_B|. \quad (2.73)$$

In these cases, the corresponding OCM T -matrix $\tilde{T}(\omega, \varepsilon)$ defined in Eq. (2.58) becomes ε -independent. The Faddeev equation takes the same form as Eq. (2.69), but no self-consistency condition like Eq.

(2.68) is necessary. By this procedure, we can prove that the solutions of the pairwise three-cluster OCM equation (2.65) (with $V^{\text{RGM}}(\varepsilon)$ replaced by V^{eff}) are achieved by Kukulin's method of orthogonalizing pseudopotentials [74]. Here again, some complexity arises for the 3α system, when the deep $\alpha\alpha$ potential by Buck, Friedrich and Wheatly [75] is employed with the bound-state solutions for the Pauli-forbidden states. In this case, one of the redundant solutions with the dominant [21] $N = 4$ (40) component does not become completely redundant, but becomes an almost redundant Faddeev component with the eigenvalue $\tau \approx -0.999$ in Eq. (2.71). Such a solution allows a large admixture of the [3]-symmetric 3α component given by

$$\phi_{\tau}^{[3]} = \frac{(1+S)|uf^{\tau}\rangle}{\sqrt{3(1+\tau)}}, \quad (2.74)$$

which has a large overlap with the shell-model like compact configuration, $[[3] N = 8 (04)]$. The ground-state solution of the modified Faddeev equations or similar equations (see, for example, Eq. (22) of Ref. [76]) gives a large binding energy with this dominant configuration, and a small admixture of the redundant components will never be completely eliminated. On the other hand, if the Kukulin's method of orthogonalizing pseudopotentials is used to eliminate the redundant components completely, one would also repel such a component as $\phi_{\tau}^{[3]}$, resulting in a very small binding energy of the 3α ground state [77, 78, 79]. Refer to Ref. [76] for details.

3 Results and discussions

3.1 Two-nucleon system

As already discussed, the reliability of the YN and YY interaction model is judged from whether or not the NN data are reproduced in such a common framework that can be extended to the YN and YY systems. A motivation to upgrade the model FSS [40] to fss2 [42] is in a better description of the NN data by including the important effects of the V mesons and the momentum-dependent higher-order terms of the S - and V -meson central forces. For example, the 3D_2 phase shift in FSS is more attractive than experiment by 10° around $T_{\text{lab}} = 300$ MeV, because the one-pion tensor force is too strong. The strong one-pion tensor force is partially weakened in the standard OBEP's by the ρ -meson tensor force. We use the QLS force mainly from the ρ -meson exchange as a phenomenological ingredient of this cancellation. Furthermore, some phase shifts of other partial waves deviate from the empirical ones by a couple of degrees. Another improvement is required for the central attraction. The G -matrix calculation using the quark-exchange kernel explicitly [45] shows that the energy-independent attraction, dominated by the ϵ -meson exchange, is unrealistic, since in our previous models the s.p. potentials in symmetric nuclear matter show a strongly attractive behavior in the momentum region 5 - 20 fm^{-1} . This flaw is removed in Ref. [44] by introducing the momentum-dependent higher-order term of the flavor-singlet S -meson exchange potential, which was first carefully examined by Bryan and Scott [80]. In the higher energy region, the LS term of the S mesons also makes an appreciable contribution.

Figures 1(a) - 1(h) compare the np phase shifts and the mixing angles ε_J predicted by fss2 with those of SP99 by Arndt *et al.* [61]. For comparison, the FSS results are also shown with the dotted curves. The phase-shift parameters are shown for the partial waves up to $J = 4$ with the energies less than 350 MeV. More information is obtained from the QMPACK homepage [81]. For the non-relativistic energies less than $T_{\text{lab}} = 300$ MeV, the NN phase-shift parameters are almost perfectly reproduced, except for the 3D_3 state. The $\sqrt{\chi^2}$ values in Eq. (2.39) are calculated using the phase-shift analysis SP99 [61] and PWA93 [82] of the Nijmegen group. The fss2 gives $\sqrt{\chi^2} = 0.59^\circ$ and 0.60° for SP99 and PWA93, respectively. These are compared to the χ^2 values of CD-Bonn [47] and ESC04 [26]; $\sqrt{\chi^2} = 0.52^\circ$ (0.16°) and 1.16° (1.01°) for CD-Bonn and ESC04, respectively, when SP99 (PWA93) is used.

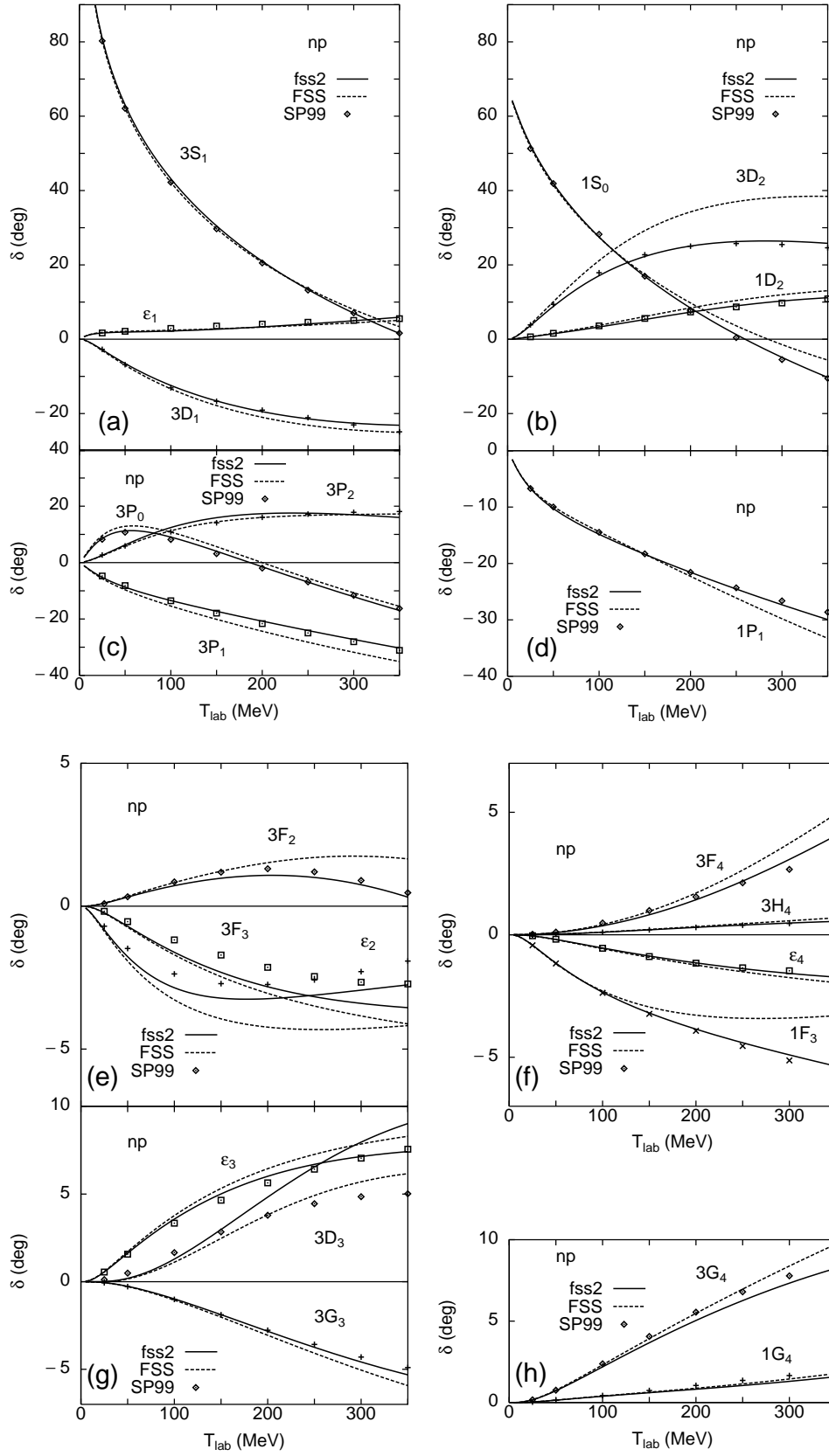


Figure 1: Calculated np phase shifts by $fss2$ in the isospin basis, compared with the phase-shift analysis SP99 by Arndt *et al.* [61] The dotted curves indicate the results given by FSS.

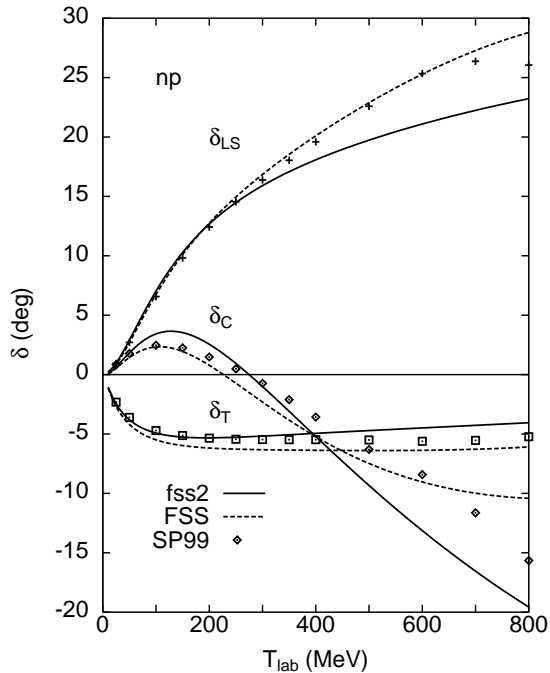


Figure 2: Decomposition of the 3P_J phase shifts for the np scattering to the central (δ_C), LS (δ_{LS}) and tensor (δ_T) components up to the energy $T_{\text{lab}} = 800$ MeV. The results given by fss2 (solid curves) and FSS (dashed curves) are compared with the decomposition of the empirical phase shifts SP99 [61].

For energies higher than 300 MeV, the inelastic process of the pion production takes place, and the effect of the ΔN channel becomes important. The inelasticity parameters determined from the phase shift analysis, however, show that they are still rather small even up to the energies $T_{\text{lab}} = 800$ MeV. We have therefore examined the results of the single-channel NN calculation up to 800 MeV in Ref. [42], in order to investigate a possible effect of the ΔN channel coupling. Up to this energy, the 3D_2 phase shift is well reproduced by the QLS component. Even in the other partial waves, the improvement of the phase-shift parameters is usually achieved. This includes 1) 3P_0 , 3P_1 , and 3G_4 phase shifts, 2) 3S_1 , 1S_0 , 1P_1 , 1F_3 , and 3H_4 phase shifts at higher energies $T_{\text{lab}} = 400 - 800$ MeV, and 3) some improvement in 3F_2 phase shift and ε_2 mixing parameter. On the other hand, 3P_2 and 3D_3 phase shifts turn out worse and 3F_4 phase shift is not much improved. The problem of fss2 lies in the 3P_2 and 3D_3 phase shifts at the intermediate and higher energies $T_{\text{lab}} = 300 - 800$ MeV. The empirical 3P_2 phase shift gradually decreases if we ignore the weak dispersion-like behavior. Our result, however, decreases too rapidly. Our 3D_3 phase shift is too attractive by $4^\circ - 6^\circ$. The disagreement of the 3D_3 phase shift and the deviation of the 3D_1 phase shift at higher energies suggests that our description of the central, tensor and LS forces in the 3E states requires further improvement. The insufficiency in the 3O partial waves is probably related to the imbalance of the central force and the LS force in the short-range region. The decomposition of the 3P_J phase shifts to the central, LS and tensor components, shown in Fig. 2, implies that the 3O central force is too repulsive at higher energies $T_{\text{lab}} \geq 400 - 500$ MeV. We find that whenever the discrepancy of the phase shifts between the calculation and the experiment is large, the inelasticity parameters are also very large. In particular, the inelasticity parameters of the 3P_2 , 1D_2 , and 3F_3 states rise very rapidly as the energy increases, and reach more than 20° at $T_{\text{lab}} = 800$ MeV. The elastic phase shift for each of these states shows a dispersion-like resonance behavior in the energy range from 500 MeV to 800 MeV. These are the well-known di-baryon resonances directly related to the ΔN threshold in the isospin $I = 1$ channel. The present single-channel calculation is not capable of describing these resonances, unlike the ${}^1S_0(NN) - {}^5D_0(N\Delta)$ CCRGM calculation in Ref. [83].

Figure 3 compares with experiment [61] the fss2 (solid curves) and FSS (dashed curves) predictions of the differential cross sections ($d\sigma/d\Omega$) and the polarizations ($P(\theta)$) for the elastic np scattering. The same observables for the elastic pp scattering are plotted in Fig. 4, and some other observables

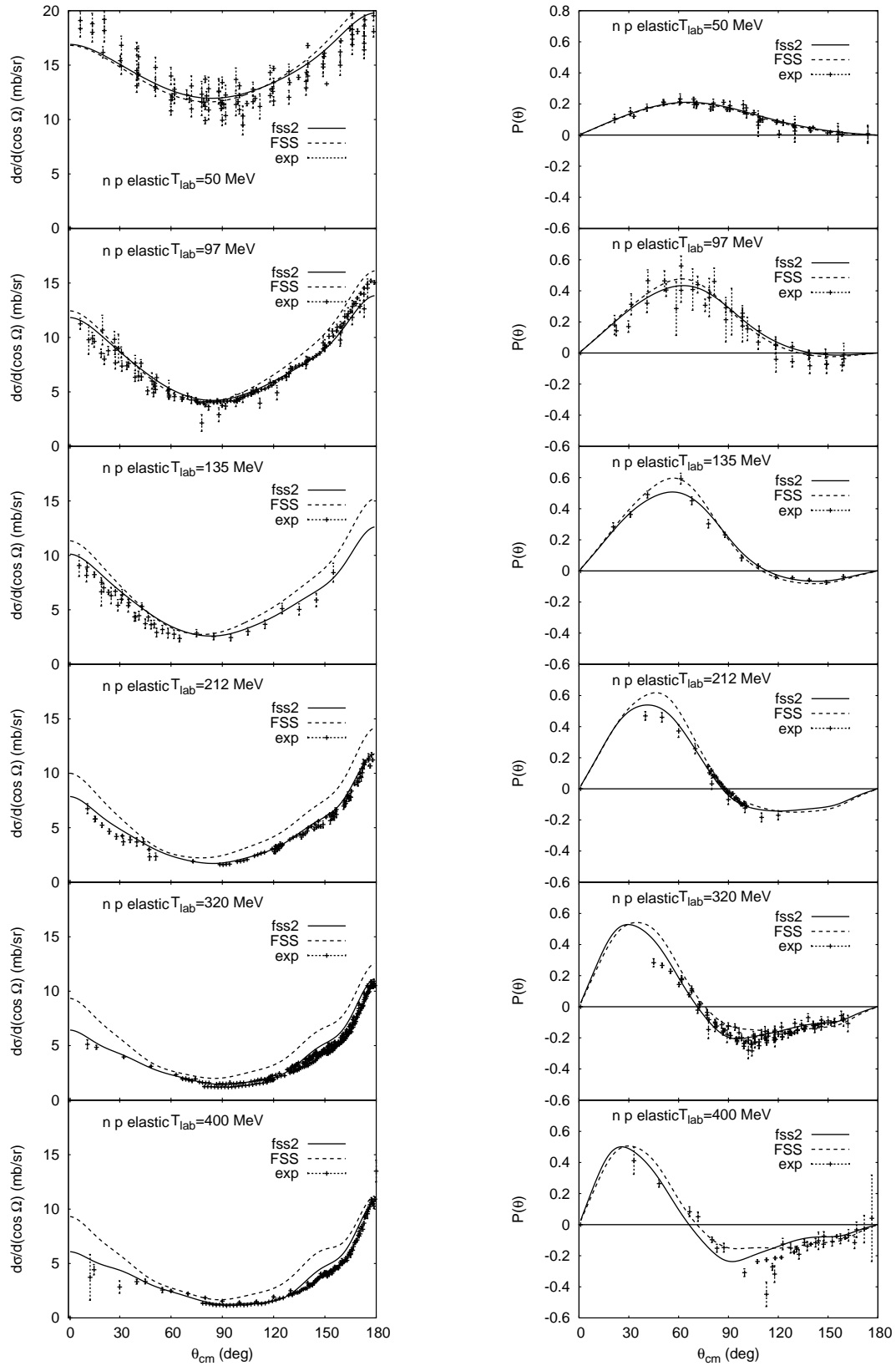


Figure 3: Calculated np differential cross sections and the polarization compared with the experiment [61]. Calculation is performed using fss2 (solid curves) and FSS (dashed curves) with the full pion-Coulomb correction included.

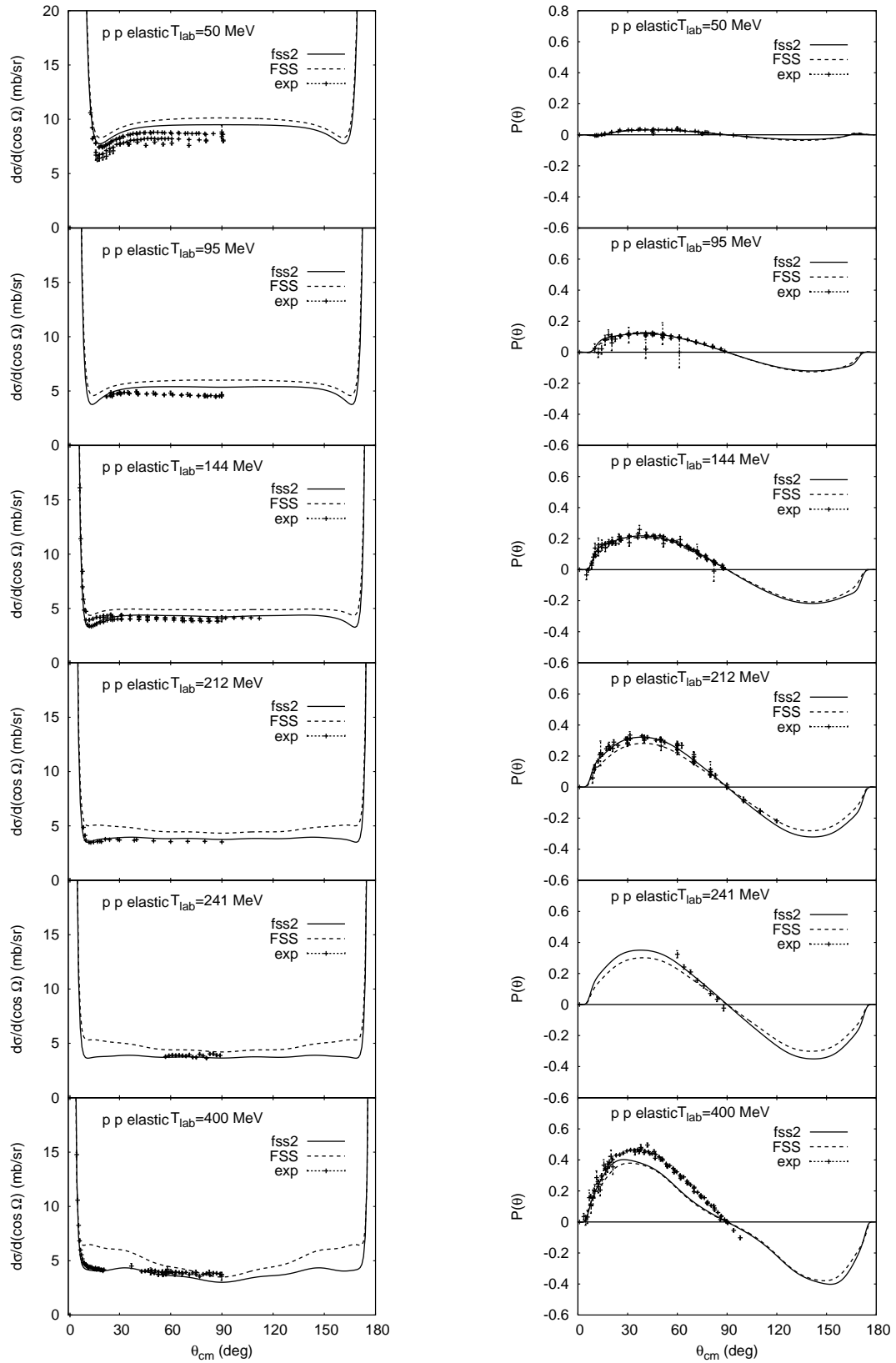


Figure 4: The same as Fig. 3 but for the pp differential cross sections and the polarization.

like the depolarization ($D(\theta)$), the vector analyzing powers ($A(\theta)$, $A'(\theta)$, $R(\theta)$), etc., in Figs. 5 and 6. These observables are obtained in the particle basis with the full Coulomb force incorporated. We find

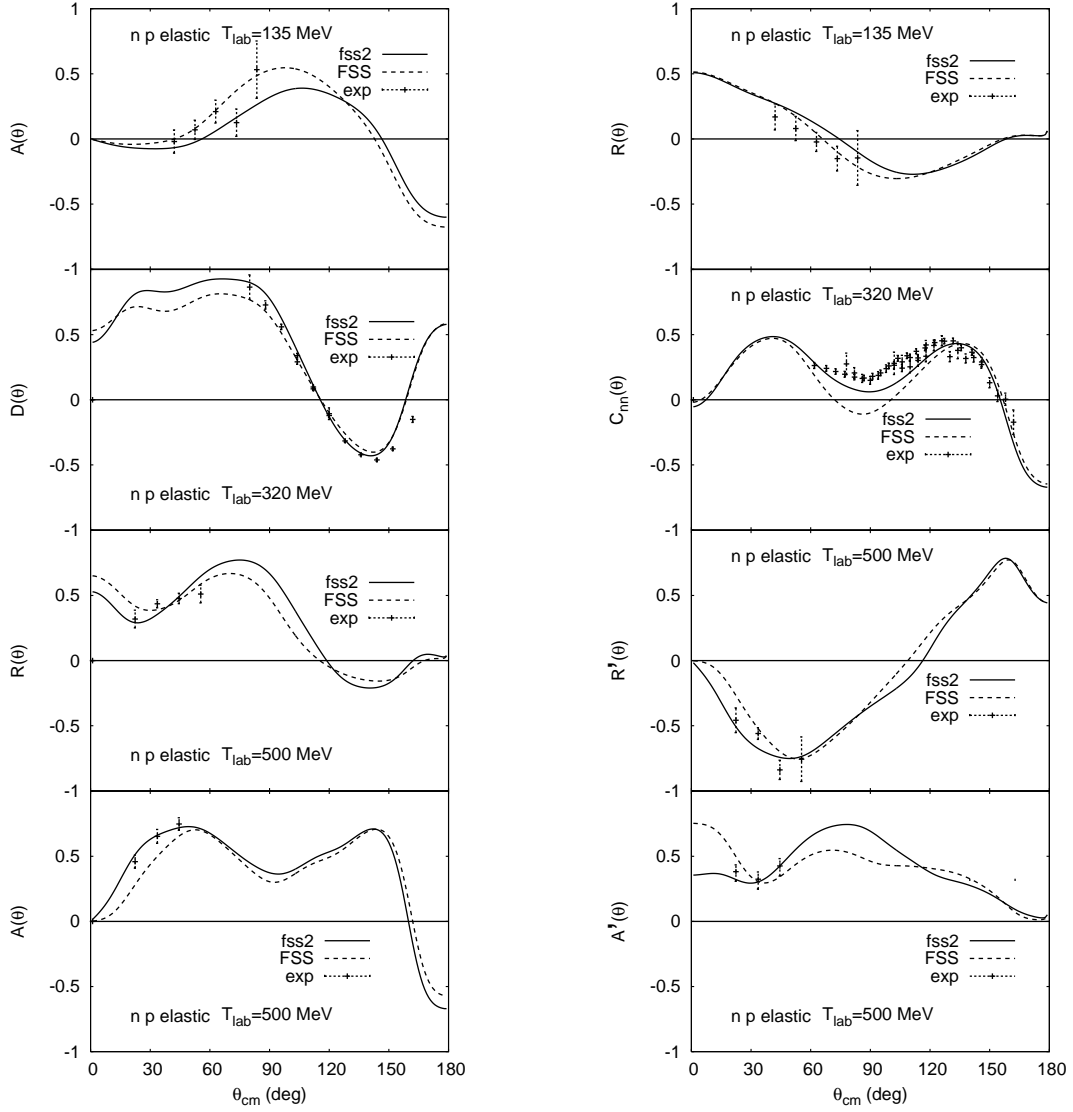


Figure 5: The same as Fig. 3 but for the other spin observables.

some improvement in the differential cross sections. First, the previous FSS overestimation of the np differential cross sections at the forward angle at $T_{\text{lab}} \geq 100$ MeV is corrected. Secondly, the bump structure of the np differential cross sections around $\theta_{\text{cm}} = 130^\circ$ at energies $T_{\text{lab}} = 300 - 800$ MeV has disappeared. The overestimation of the pp differential cross sections at $\theta_{\text{cm}} = 10^\circ - 30^\circ$ at energies $T_{\text{lab}} = 140 - 400$ MeV is improved. However, the essential difficulties of FSS, namely the oscillatory behavior of the np polarization around $\theta_{\text{cm}} = 110^\circ$ and that of the pp polarization around the symmetric angle $\theta_{\text{cm}} = 90^\circ$ for higher energies $T_{\text{lab}} \geq 400$ MeV are not resolved. Furthermore, the pp differential cross sections show a deep dip at angles $\theta_{\text{cm}} \leq 30^\circ$ and $\geq 150^\circ$ for $T_{\text{lab}} \geq 500$ MeV. The low-energy pp cross sections at $\theta_{\text{cm}} = 90^\circ$ for $T_{\text{lab}} \leq 100$ MeV are still overestimated.

In order to find a possible reason for the unfavorable oscillations of our polarizations, we compared in Fig. 3 of Ref. [42] the five independent pp invariant amplitudes at the highest energy $T_{\text{lab}} = 800$ MeV, predicted by fss2 and the phase-shift analysis SP99. They are composed of the real and imaginary parts of g_0 (spin-independent central), h_0 (LS), h_n ($(\boldsymbol{\sigma}_1 \cdot \hat{\mathbf{n}})(\boldsymbol{\sigma}_2 \cdot \hat{\mathbf{n}})$ -type tensor), h_k ($(\boldsymbol{\sigma}_1 \cdot \hat{\mathbf{k}})(\boldsymbol{\sigma}_2 \cdot \hat{\mathbf{k}})$ -type tensor), and h_P ($(\boldsymbol{\sigma}_1 \cdot \hat{\mathbf{P}})(\boldsymbol{\sigma}_2 \cdot \hat{\mathbf{P}})$ -type tensor) invariant amplitudes in Eq. (2.45). The result by SP99 was calculated using only the real parts of the empirical phase-shift parameters. Recalling

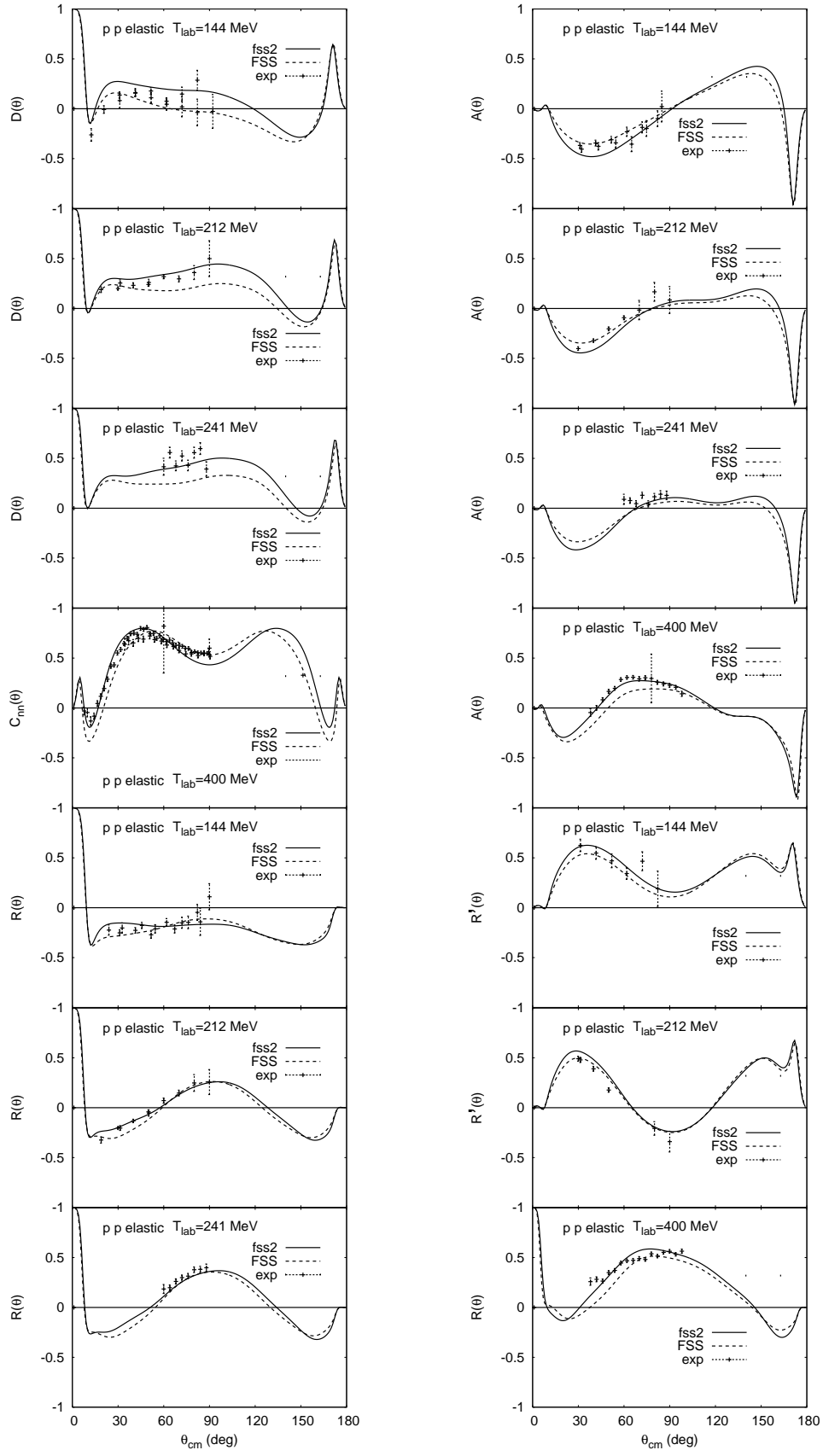


Figure 6: The same as Fig. 4 but for the other spin observables.

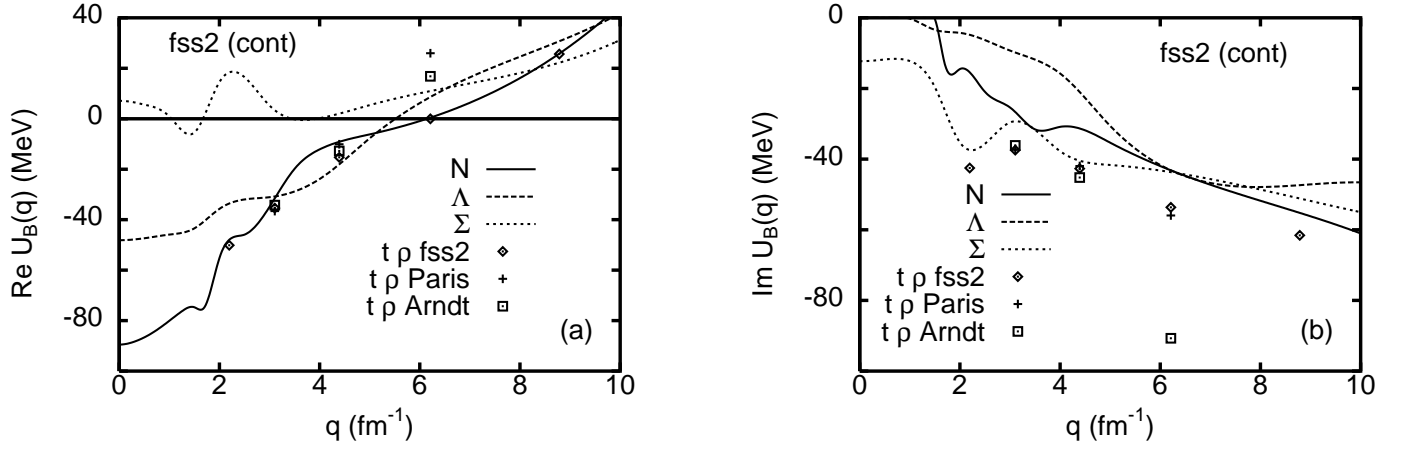


Figure 7: The momentum dependence of the s.p. potentials $U_B(q)$ predicted by the G -matrix calculation of fss2 in the continuous prescription for intermediate spectra: (a) The real part, $\text{Re } U_B(q)$. (b) The imaginary part, $\text{Im } U_B(q)$. The nucleon s.p. potentials obtained by the $t^\text{eff} \rho$ prescription are also shown for fss2, the Paris potential [84] and the empirical phase shifts SP99 [61]. The momentum points selected correspond to $T_\text{lab} = 100, 200, 400, 800$, and 1600 MeV for the NN scattering. The partial waves up to $J = 8$ are included in fss2 and the Paris potential, and $J = 7$ in SP99.

that the polarization is given by the cross term contribution of the central, LS , and tensor invariant amplitudes (i.e., $P(\theta) = 2 \text{Im} [(g_0 + h_n)(h_0)^*]$ from Eq. (2.48) since $h_- = f_\pm = 0$ for NN), we find that the disagreement in $\text{Im } h_n$ and $\text{Re } h_0$ is most serious. Since the oscillatory behavior of $\text{Im } h_n$ in SP99 also appears in $\text{Im } h_k$ and $\text{Im } h_P$, it is possible that this is an oscillation caused by the NN - ΔN channel coupling through the one-pion spin-spin and tensor forces. From the figure, we can also expect the underestimation of the differential cross sections at $\theta_\text{cm} \leq 30^\circ$ in this energy region. Namely, the imaginary part of g_0 is too small and the real part of g_0 is strongly reduced in fss2.

Another application of the invariant amplitudes is the $t^\text{eff} \rho$ prescription for calculating the s.p. potentials of the nucleons and hyperons in nuclear matter. It is discussed in Ref. [44] that the s.p. potentials predicted by the model FSS in the G -matrix calculation show fairly strong attractive behavior in the momentum interval $q = 5 - 20 \text{ fm}^{-1}$ for all the baryons. In particular, $U_N(q)$ in the continuous prescription becomes almost -80 MeV at $q = 10 \text{ fm}^{-1}$. This momentum interval corresponds to the incident-energy range $T_\text{lab} = 500 \text{ MeV} - 8 \text{ GeV}$ in the NN scattering. The $t^\text{eff} \rho$ prescription is a convenient way to evaluate the s.p. potentials in the asymptotic momentum region in terms of the spin-independent invariant amplitude at the forward angle $g_0(\theta = 0)$. Since the present model fss2 incorporates the momentum-dependent Bryan-Scott term, the asymptotic behavior of the s.p. potentials in the large momentum region is improved. We can see this in Fig. 7, where the s.p. potentials of N , Λ , and Σ calculated in the G -matrix approach are shown in the momentum range $q = 0 - 10 \text{ fm}^{-1}$. Figures 7(a) and 7(b) show the real and imaginary parts of $U_B(q)$, obtained in the continuous choice for intermediate spectra. The solid curves for the nucleon s.p. potential are compared with the results by the $t^\text{eff} \rho$ prescription with respect to the T -matrices of fss2, the Paris potential [84], and the empirical phase shifts SP99 [61]. The partial waves up to $J \leq 8$ are included in fss2 and the Paris potential, and $J \leq 7$ in SP99. The momentum points calculated correspond to the energies $T_\text{lab} = 100, 200, 400, 800$, and $1,600 \text{ MeV}$. We find that the real part of $U_N(q)$ nicely reproduces the result of the G -matrix calculation even at such a low energy as $T_\text{lab} = 100 \text{ MeV}$. On the other hand, the imaginary part by the $t^\text{eff} \rho$ prescription usually overestimates the exact result especially at lower energies.

The deuteron properties are calculated by solving the LS-RGM equation with respect to the relative wave functions $f_0(k)$ and $f_2(k)$ in the momentum representation (see Appendix B of Ref. [42]). The properly normalized wave functions in the Schödinger picture are not $f_\ell(k)$ but $F_\ell = \sqrt{N} f_\ell$, where N represents the normalization kernel [40]. The S -wave and D -wave wave functions in the coordinate representation, $u(R)$ and $w(R)$, are then obtained from the inverse Fourier transform of $F_\ell(k)$. This process is most easily carried out by expanding $F_\ell(k)$ in a series of Yukawa functions $\sqrt{2/\pi}k/(k^2 + \gamma_j^2)$ in the momentum representation (see Appendix D of Ref. [47]). We choose $\gamma_j = \gamma + (j-1)\gamma_0$ ($j = 1 - 11$) with $\gamma_0 = 0.9 \text{ fm}^{-2}$. The γ is the S -matrix pole $q = -i\gamma$, from which the deuteron energy ϵ_d is most accurately calculated by using the relativistic relation

$$M_n + M_p - \epsilon_d = \sqrt{M_n^2 - \gamma^2} + \sqrt{M_p^2 - \gamma^2} . \quad (3.1)$$

Figure 8 shows the deuteron wave function of fss2 in the coordinate and momentum representations, in comparison with that of the Bonn model-C potential [85] (dotted curves)¹. We find that the difference between the two models is very small. Table 3 compares various deuteron properties calculated in three different schemes: the isospin basis and the particle basis without or with the Coulomb force. They are also compared with the empirical values and the predictions by the Bonn model-C potential. The final value of the deuteron binding energy for fss2 is $\epsilon_d = 2.2309 \text{ MeV}$. If we use the non-relativistic energy expression,² $\epsilon_d = (\gamma^2/M_N)$ for $\gamma^2 = 0.053762 \text{ fm}^{-2}$ in the full calculation, we obtain $\epsilon_d = 2.2295 \text{ MeV}$ and the difference is 1.4 keV. The differences within the deuteron parameters calculated in the three different schemes are very small, except for the binding energy ϵ_d . In particular, the exchange Coulomb kernel due to the exact antisymmetrization at the quark level gives an attractive effect to the binding energy, and increases ϵ_d by 4.8 keV. This is even larger than the relativistic correction included in Eq. (3.1). The deuteron D -state probability is $P_D = 5.49 \%$ in fss2, which is slightly smaller than 5.88 % in FSS [40]. These values are close to the Bonn model-C value $P_D = 5.60 \%$ [85]. The asymptotic D/S state ratio η and the rms radius are very well reproduced. On the other hand, the quadrupole moment is too small by about 5 - 6%. There are some calculations [87, 88] which claim that the effect of the meson-exchange currents on the deuteron quadrupole moment is as large as $\Delta Q_d = 0.01 \text{ fm}^2$. It is noteworthy that the Bonn model-C almost reproduces the correct quadrupole moment, in spite of the fact that the D -state probability is very close to ours. (On the other hand, the quadrupole moment of

¹The results of the Bonn model-C potential in Fig. 8 and in Table 3 are based on the parameterized deuteron wave functions given in Table C.4 of Ref. [85].

²In Table 3, the value of ϵ_d in the isospin basis is calculated using this non-relativistic formula.

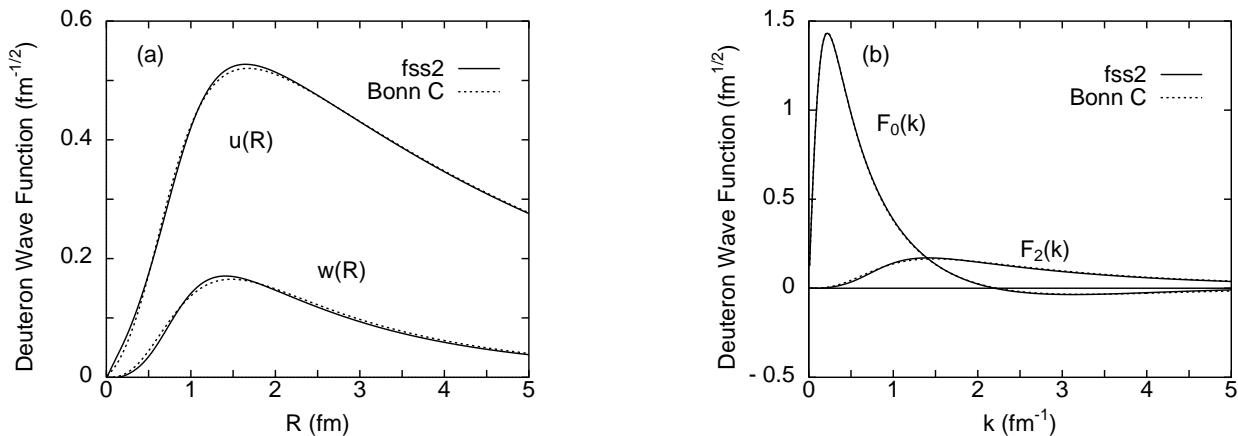


Figure 8: The deuteron wave functions predicted by fss2 (solid curves) and by Bonn model-C [85] in the coordinate (a) and momentum (b) representations.

Table 3: Deuteron properties by fss2 in three different calculational schemes, compared with the predictions of the Bonn model-C potential [85] and the experiment.

	isospin basis	particle basis		Bonn C	Expt.	Ref.
		Coulomb off	Coulomb on			
ϵ_d (MeV)	2.2250	2.2261	2.2309	fitted	2.224644 ± 0.000046	[86]
P_D (%)	5.490	5.490	5.494	5.60		
$\eta = A_D/A_S$	0.02527	0.02527	0.02531	0.0266	0.0256 ± 0.0004	[89]
rms (fm)	1.9598	1.9599	1.9582	1.968	1.9635 ± 0.0046	[86]
Q_d (fm ²)	0.2696	0.2696	0.2694	0.2814	0.2860 ± 0.0015	[90]
μ_d (μ_N)	0.8485	0.8485	0.8485	0.8479	0.85742	

CD-Bonn [47] is $Q_d = 0.270$ fm² with a smaller value $P_D = 4.85\%$.) For the magnetic moment, precise comparison with the experimental value requires a careful estimation of various corrections arising from the meson-exchange currents and the relativistic effect, etc.

Table 4 lists the S - and P -wave effective range parameters for the NN system, calculated in the three schemes. Since the pion-Coulomb correction is not sufficient to explain the full CIB effect existing in the np and pp 1S_0 states, a simple prescription to multiply the flavor-singlet S -meson coupling constant f_1^S by a factor 0.9949 is adopted to reduce too large attraction of the pp central force. (This prescription is applied only to the calculation in the particle basis.) The underlined values of the scattering length a in Table 4 indicate that they are fitted to the experimental values. We find that the pion-Coulomb correction in the np 1S_0 state has a rather large effect on a . The value $a = -23.76$ fm in the isospin basis changes to $a = -27.39$ fm due to the effect of the pion mass correction and the explicit use of the neutron and proton masses. It further changes to $a = -27.87$ fm due to the small effect of the exchange Coulomb kernel. These changes should, however, be carefully reexamined by readjusting the binding energy of the deuteron in Table 3. We did not carry this out, since the reduction of f_1^S to fit these values to the empirical value $a = -23.748 \pm 0.010$ fm does not help much to reproduce the CIB of the pp channel. This shortcoming might be related to the insufficient description of the low-energy pp differential cross sections around $\theta_{\text{cm}} = 90^\circ$, as seen in Fig. 4. It was also pointed out by the Nijmegen group [94] that the Coulomb phase shift should be improved by the effects of two-photon exchange, vacuum polarization, and magnetic moment interactions, in order to describe the 1S_0 phase shift precisely at energies less than 30 MeV. Neither of these effects, nor more sophisticated charge-symmetry breaking operators due to the interference of QED and QCD [95], are taken into account in the present calculation. The P -wave effective range parameters are also given in Table 4, to compare with a number of empirical predictions. The parameters of 3P_2 state are not given, since the effective range expansion of this partial wave requires a correction term related to the accidental p^5 low-energy behavior of OPEP [96].

3.2 Hyperon-nucleon interactions

3.2.1 The spin-flavor SU_6 symmetry in the $B_8 B_8$ interactions

Our $(3q)$ -cluster wave functions in the $(3q)$ -($3q$) RGM formalism are the strict SU_6 wave functions in the spin-flavor SU_6 QM. This fact and the complete antisymmetrization of quarks in the RGM framework make it possible to investigate interesting relationship of the various $B_8 B_8$ interactions under some plausible assumptions and special roles of pions. First it should be noted that our phenomenological confinement potential does not have any flavor dependence. The contribution of the r^2 -type confine-

Table 4: Effective range parameters of fss2 for the NN interactions. For the pp and nn systems, the calculation in the particle basis uses $f_1^S \times 0.9949$, in order to incorporate the effect of the charge-independence breaking (CIB). Unit of length is in $\text{fm}^{2\ell+1}$ (a), $\text{fm}^{-2\ell+1}$ (r) and $\text{fm}^{-2\ell}$ (P) for the partial wave ℓ . The experimental values are taken from [86], [91], [92], [93], [94], and [47].

		isospin basis	particle basis		Expt.
			Coulomb off	Coulomb on	
pp	1S_0	a	-17.80	<u>-7.810</u>	-7.819 ± 0.0026
		r	2.680	<u>2.581</u>	2.794 ± 0.0014
		P	0.061	-0.064	
pp	3P_0	a	-2.876	-3.117	$-4.82 \pm 1.11, -2.71 \pm 0.34$
		r	3.834	3.735	$7.14 \pm 0.93, 3.8 \pm 1.1$
		P	-0.011	-0.034	
pp	3P_1	a	1.821	1.992	$1.78 \pm 0.10, 1.97 \pm 0.09$
		r	-8.162	-7.5666	$-7.85 \pm 0.52, -8.27 \pm 0.37$
		P	0.001	0.001	
nn	1S_0	a	-18.04	-18.04	$-18.05 \pm 0.3, -18.9 \pm 0.4$
		r	2.677	2.677	2.75 ± 0.11
		P	0.061	0.061	
nn	3P_0	a	-2.881	-2.881	
		r	3.825	3.825	
		P	-0.011	-0.011	
nn	3P_1	a	1.823	1.823	
		r	-8.154	-8.155	
		P	0.001	0.001	
np	1S_0	a	<u>-23.76</u>	-27.39	-23.748 ± 0.010
		r	2.588	2.532	2.75 ± 0.05
		P	0.059	0.052	
np	3P_0	a	-2.740	-2.466	
		r	3.869	3.930	
		P	-0.013	-0.018	
np	3S_1	a	5.399	5.400	5.424 ± 0.004
		r	1.735	1.735	1.759 ± 0.005
		P	0.063	0.063	
np	1P_1	a	2.824	2.826	
		r	-6.294	-6.300	
		P	-0.006	-0.006	
np	3P_1	a	1.740	1.582	
		r	-8.198	-8.185	
		P	0.001	0.000	

ment potential to the baryon-baryon interaction is zero due to the subtraction of the internal energy contribution. The FB interaction involves the FSB only through the quark-mass dependence, but the effect is rather weak. Thus we can assume that our QM Hamiltonian is approximately SU_3 scalar.

On the other hand, the EMEP contribution is also approximately SU_3 scalar, except for the pion contribution. This is because the SU_3 relations of the coupling constants are automatically incorporated in the QM description. The usage of the empirical masses for the PS and V mesons breaks the SU_3 symmetry, together with the baryon masses. The S-meson masses are varied to fit the NN and YN data, but these are also assumed to be SU_3 symmetric in the first approximation. After all, our QM Hamiltonian with the EMEP's is approximately SU_3 scalar as a whole, except for the important roles of pions with the very small mass. If the Hamiltonian is approximately SU_3 scalar, we can expect that the baryon-baryon interactions with the same SU_3 representation should be very similar, since the dependence on the internal quantum numbers becomes negligible. From this discussion, we can correlate different $B_8 B_8$ interactions according to the SU_3 representation of the $B_8 B_8$ systems.

Table 5 illustrates how the two-baryon systems in the isospin basis, defined by Eq. (2.8), are classified as a combination of the SU_3 bases. Entirely different structure appears between the flavor-symmetric and antisymmetric cases. In the 1S_0 state, for example, we have several systems containing the (22) component dominantly. The S -state $B_8 B_8$ interactions for these systems are expected to be similar to that for the NN 1S_0 state. The $(11)_s$ component is completely Pauli forbidden for the most compact $(0s)^6$ configuration, and is characterized by the strong repulsion originating from the quark Pauli principle. The (00) component in the H -particle channel is attractive because of the color-magnetic interaction. On the other hand, in the NN sector the 3S_1 state with $I = 0$ is composed of the pure

Table 5: The relationship between the isospin basis and the flavor- SU_3 basis for the $B_8 B_8$ systems. The flavor- SU_3 symmetry is given by the Elliott notation $(\lambda\mu)$. The heading \mathcal{P} denotes the flavor-exchange symmetry, S the strangeness, and I the isospin.

S	$B_8 B_8 (I)$	$\mathcal{P} = +1$ (symmetric)	$\mathcal{P} = -1$ (antisymmetric)
		1E or 3O	3E or 1O
0	$NN (I = 0)$	—	(03)
	$NN (I = 1)$	(22)	—
-1	ΛN	$\frac{1}{\sqrt{10}}[(11)_s + 3(22)]$	$\frac{1}{\sqrt{2}}[-(11)_a + (03)]$
	$\Sigma N (I = 1/2)$	$\frac{1}{\sqrt{10}}[3(11)_s - (22)]$	$\frac{1}{\sqrt{2}}[(11)_a + (03)]$
	$\Sigma N (I = 3/2)$	(22)	(30)
-2	$\Lambda\Lambda$	$\frac{1}{\sqrt{5}}(11)_s + \frac{9}{2\sqrt{30}}(22) + \frac{1}{2\sqrt{2}}(00)$	—
	$\Xi N (I = 0)$	$\frac{1}{\sqrt{5}}(11)_s - \sqrt{\frac{3}{10}}(22) + \frac{1}{\sqrt{2}}(00)$	$(11)_a$
	$\Xi N (I = 1)$	$\sqrt{\frac{3}{5}}(11)_s + \sqrt{\frac{2}{5}}(22)$	$\frac{1}{\sqrt{3}}[-(11)_a + (30) + (03)]$
	$\Sigma\Lambda$	$-\sqrt{\frac{2}{5}}(11)_s + \sqrt{\frac{3}{5}}(22)$	$\frac{1}{\sqrt{2}}[(30) - (03)]$
	$\Sigma\Sigma (I = 0)$	$\sqrt{\frac{3}{5}}(11)_s - \frac{1}{2\sqrt{10}}(22) - \sqrt{\frac{3}{8}}(00)$	—
	$\Sigma\Sigma (I = 1)$	—	$\frac{1}{\sqrt{6}}[2(11)_a + (30) + (03)]$
	$\Sigma\Sigma (I = 2)$	(22)	—
-3	$\Xi\Lambda$	$\frac{1}{\sqrt{10}}[(11)_s + 3(22)]$	$\frac{1}{\sqrt{2}}[-(11)_a + (30)]$
	$\Xi\Sigma (I = 1/2)$	$\frac{1}{\sqrt{10}}[3(11)_s - (22)]$	$\frac{1}{\sqrt{2}}[(11)_a + (30)]$
	$\Xi\Sigma (I = 3/2)$	(22)	(03)
-4	$\Xi\Xi (I = 0)$	—	(30)
	$\Xi\Xi (I = 1)$	(22)	—

(03) state, and the deuteron is bound in this channel owing to the strong one-pion tensor force. This SU_3 state in the flavor-antisymmetric case is converted to the (30) state in the side of more negative strangeness. Since the (30) state is almost Pauli forbidden with the eigenvalue $\mu = 2/9$ of the normalization kernel, the interaction is strongly repulsive. Therefore, the $\Xi\Xi$ interaction is not so attractive as NN , since they are combinations of (22) and (30). The other SU_3 state $(11)_a$ turns out to have very weak interaction. After all, the strangeness $S = -2$ sector is most difficult, since it is a turning point of the strangeness. It is also interesting to see that the $\Xi\Sigma$ channel with $I = 3/2$ should be fairly attractive, since the channel contains the same (22) and (03) SU_3 states as the NN system.

Figure 9(a) shows fss2 predictions for the 1S_0 phase shifts of various $B_8 B_8$ interactions having the pure (22) configuration. The corresponding phase-shift equivalent local potentials at $p_{\text{lab}} = 200 \text{ MeV}/c$, derived by the WKB-RGM technique [97, 98], are depicted in Fig. 10(b). Although the $\Sigma\Sigma$ interaction with isospin $I = 2$ is very similar to the NN interaction, the other interactions generally get weaker as more strangeness is involved. This is a combined effect of both the FSB in the quark sector and the EMEP contributions. In particular, the $\Xi\Xi$ interaction shows the lowest rise of the phase shift, which is less than 30° . Accordingly, the $\Xi\Xi$ total cross sections become much smaller than the other systems, as seen in Fig. 9(b). This figure also shows the total cross sections of the np and $\Xi^-\Sigma^-$ scatterings, in which the flavor-symmetric states have the SU_3 (22) representation and the antisymmetric states (03) representation. The larger cross sections of the np scattering are due to the very strong effect of pions. There is no pion effect in the exchange Feynman diagram for the $\Xi^-\Sigma^-$ scattering. More detailed analysis shows that the NN interaction is the strongest and has the largest cross sections among any combinations of the B_8 's.

This kind of analysis is also applicable to the flavor-antisymmetric configurations. Figure 10(a) shows the phase-shift behavior of the 3S_1 states for the $NN(I = 0)$ system with (03), $\Xi\Sigma(I = 3/2)$ with (03), $\Xi N(I = 0)$ with $(11)_a$, $\Sigma N(I = 3/2)$ with (30), and $\Xi\Xi(I = 0)$ with (30). First we find that the (03) states are attractive similarly to the (22) state. The existence of the deuteron in the $NN(I = 0)$ system is due to the very strong tensor force of the one-pion exchange. Next, the $(11)_a$ state represented by the $\Xi N(I = 0)$ system is weakly attractive, and the phase-shift rise is only 5° . Finally, the (30) states represented by the $\Sigma N(I = 3/2)$ and $\Xi\Xi(I = 0)$ systems are both repulsive, but the repulsion of the $\Xi\Xi(I = 0)$ state is slightly weaker than that of the $\Sigma N(I = 3/2)$ state due to the FSB.

It should be kept in mind that the systematics based on the relationship in Table 5 serves as a guide and the deviation from the pure SU_3 symmetric rules is very much model dependent. For example, the model FSS gives 1S_0 bound states for the $\Sigma\Sigma(I = 2)$, $\Xi\Sigma(I = 3/2)$, and $\Xi\Xi(I = 1)$ systems with

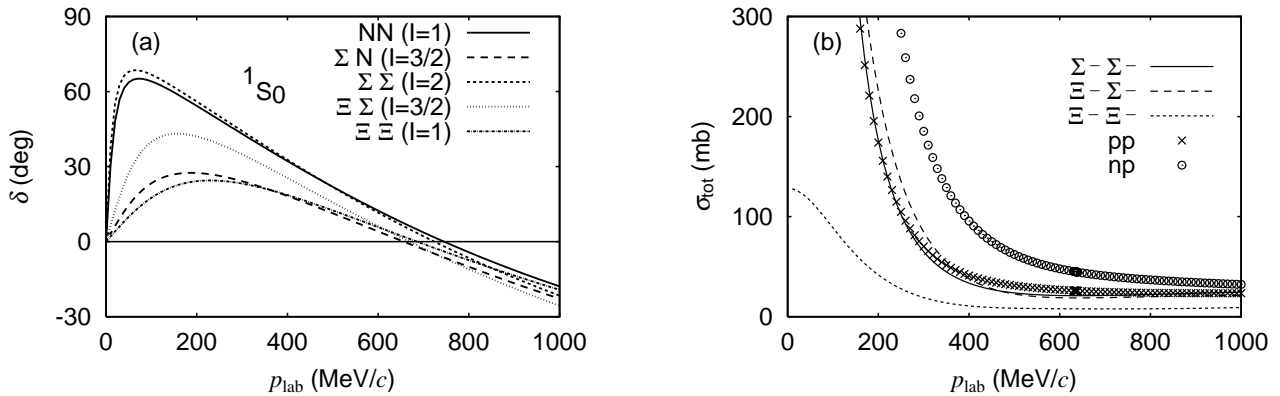


Figure 9: (a) 1S_0 phase shifts for the $B_8 B_8$ interactions with the pure (22) state, predicted by fss2. (b) Total elastic cross sections for the pure (22) state (pp , $\Sigma^-\Sigma^-$, $\Xi^-\Xi^-$) and for the (22)+(03) states (np , $\Xi^-\Sigma^-$), predicted by fss2. The Coulomb force is neglected.

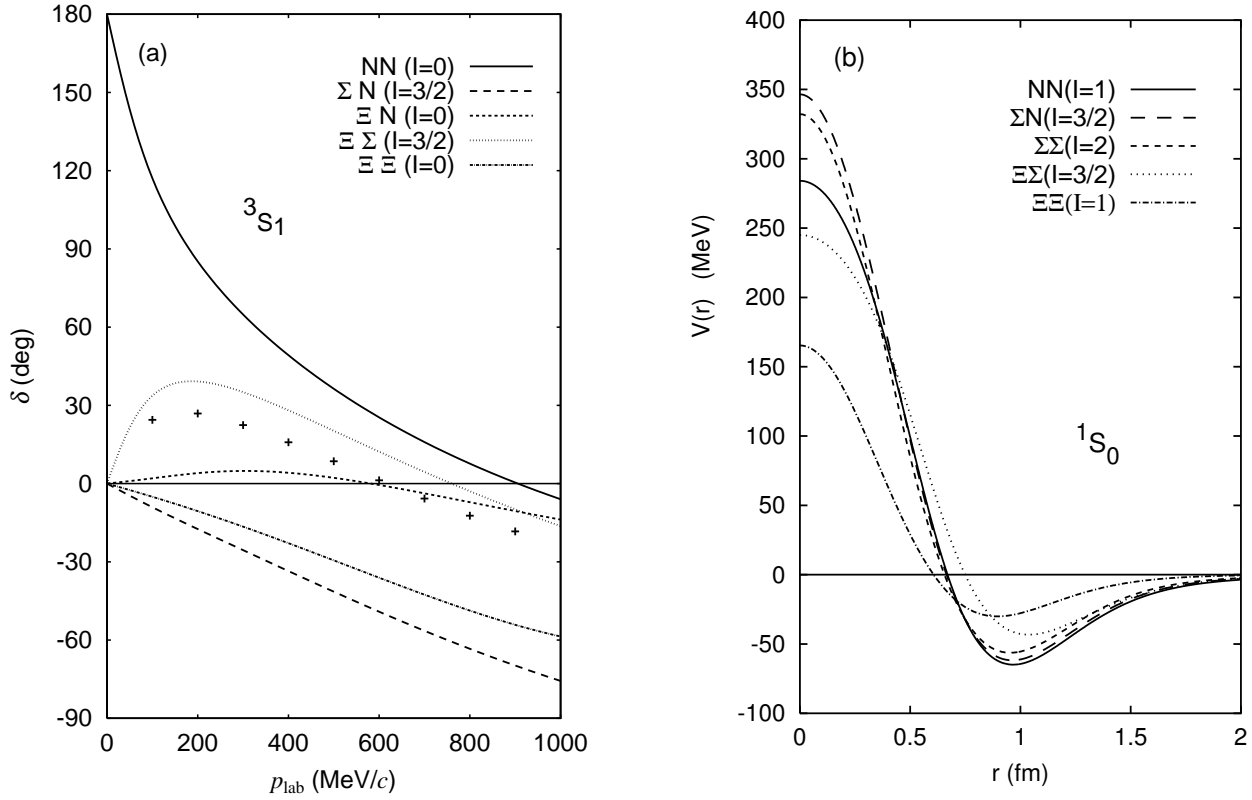


Figure 10: (a) 3S_1 phase shifts for some $B_8 B_8$ interactions, predicted by fss2. The SU_3 configurations are (03) for $NN(I=0)$ and $\Xi\Sigma(I=3/2)$, $(11)_a$ for $\Xi N(I=0)$, (30) for $\Sigma N(I=3/2)$ and $\Xi\Xi(I=0)$. The 3S_1 $NN(I=0)$ phase shift predicted only by the central interaction is also shown by crosses. (b) 1S_0 phase-shift equivalent local potentials of $NN(I=1)$, $\Sigma N(I=3/2)$ with $\theta_S = 33.3295^\circ$ (see Table 2), $\Sigma\Sigma(I=2)$, $\Xi\Sigma(I=3/2)$, and $\Xi\Xi(I=1)$ systems predicted by fss2 at $p_{\text{lab}} = 200$ MeV/c.

the pure (22) representation. This is due to the imbalanced reduction in the short-range repulsion of the color-magnetic interaction and the intermediate-range attraction of the flavor-singlet scalar-meson exchange EMEP with increasing strangeness. Since no such bound states are observed experimentally, the above discussions based on the model fss2 seem to be more reliable and give an important guide line to construct realistic models for the $B_8 B_8$ interactions.

3.2.2 $\Sigma^+ p$ system

Sine the S -wave phase shifts of the $\Sigma N(I=3/2)$ system are already given in Figs. 9(a) and 10(a), we only show the P -wave phase shifts in Fig. 11. The phase shifts given by FSS are also shown for comparison. The 1E and 3O states of the $\Sigma N(I=3/2)$ system belong to the (22) representation in the flavor SU_3 symmetry, in exactly the same as the isospin $I=1$ NN system. The phase-shift behavior of these partial waves therefore resembles that of the NN system, as long as the effect of the FSB is not significant. Figure 9(a) shows that the attraction in the 1S_0 state is much weaker than that of the NN system, and the phase-shift peak is about 26° around $p_\Sigma = 200$ MeV/c. The 3P_J phase shifts show the characteristic energy dependence observed in the NN phase shifts, which is caused by different roles of the central, tensor and LS forces. The appreciable difference in the two models fss2 and FSS appears only in the 3P_2 state. It is discussed in Ref. [99] that the attractive behavior of the 3P_2 phase shift is closely related to the magnitude of the $\Sigma^+ p$ polarization $P(\theta)$ at the intermediate energies. The more attractive the phase-shift behavior, the larger $P(\theta = 90^\circ)$. In Fig. 12(a), the polarization observable for

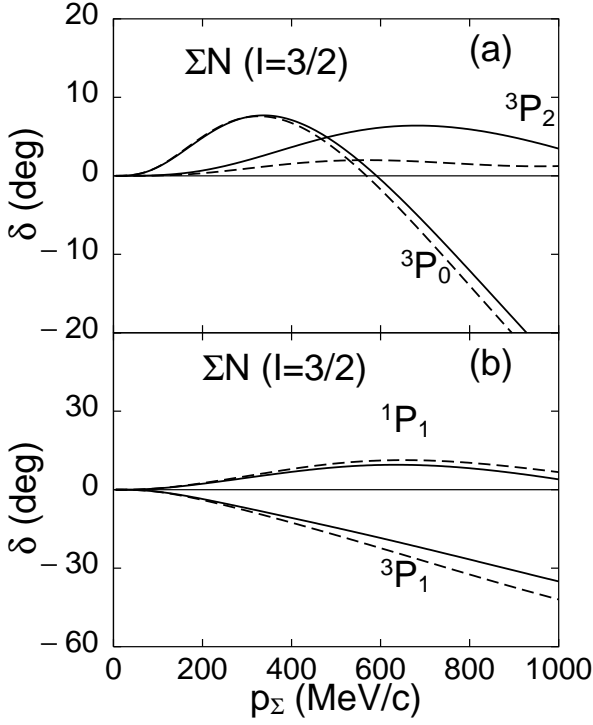


Figure 11: The P -wave phase shifts of the $\Sigma N(I = 3/2)$ system, predicted by fss2 (solid curves) and FSS (dashed curves).

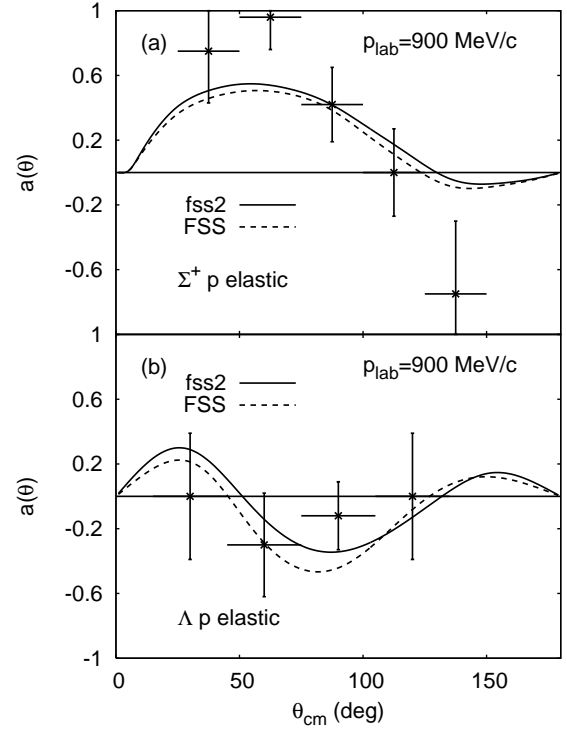


Figure 12: $\Sigma^+ p$ (a) and Λp (b) asymmetries at $p_\Sigma = 900$ MeV/c, predicted by fss2 and FSS. The experimental data are taken from [100, 101].

the $\Sigma^+ p$ elastic scattering at $p_\Sigma = 900$ MeV/c is shown for the models fss2 and FSS. The experimental data [100] imply the asymmetry parameter $a^{\text{exp}} = 0.44 \pm 0.2$ at $p_\Sigma = 800 \pm 200$ MeV/c, which is not inconsistent with our QM predictions provided that the scattering angle is not specified. More recent data [101] at $p_\Sigma = 700 - 1,100$ MeV/c are plotted in Fig. 12(a).

On the other hand, the 3E and 1O states of the $\Sigma N(I = 3/2)$ system have the (30) symmetry. We have no information on the properties of these states from the NN interaction. In our QM framework, however, there is very little ambiguity in the phase shifts of these states. Since the $(0s)^6$ configuration in the 3S_1 state is almost Pauli forbidden, the interaction in the 3S_1 state is strongly repulsive. On the other hand, the 1P_1 phase shift is weakly attractive, which is caused by the exchange kinetic-energy kernel owing to the Pauli principle.

The effective range parameters of the YN scattering in the single-channel analysis are given in Table 6 with some empirical values. For the $\Sigma^+ p$ system, the empirical values given in Ref. [48] should be compared with the results in the particle-basis calculation including the Coulomb force. We find a reasonable agreement both in the 1S_0 and 3S_1 states.

3.2.3 ΛN system

The total cross section for the Λp elastic scattering predicted by fss2 in the isospin basis is displayed in Fig. 19(e) later, together with the previous result given by FSS. The both models reproduce experimental data equally well in the low momentum region $p_\Lambda \leq 300$ MeV/c. The total cross section has a cusp structure at the ΣN threshold due to the strong $\Lambda N - \Sigma N(I = 1/2)$ $^3S_1 - ^3D_1$ coupling caused by the tensor force of the OPEP. To see the dominant role of the tensor force of the $\Lambda N - \Sigma N$ coupling in more detail, we show the 3S_1 and 1S_0 phase shifts in Fig. 13 calculated in the isospin basis. A cusp structure at the ΣN threshold is apparent in the 3S_1 channel, while very small in the 1S_0 channel. In both models,

Table 6: 1S_0 (a_s , r_s) and 3S_1 (a_t , r_t) effective range parameters of fss2 for B_8B_8 interactions. Unit of length is in fm. The experimental values are taken from [48] for Σ^+p , and from [108] and [109] for Λp .

isospin basis			particle basis		Expt.
			Coulomb off	Coulomb on	
Σ^+p	a_s	-2.51	-2.48	-2.28	-2.42 ± 0.30
	r_s	4.92	5.03	4.68	3.41 ± 0.30
	a_t	0.729	0.727	0.826	0.709 ± 0.001
	r_t	-1.22	-1.31	-1.52	-0.783 ± 0.003
Λp	a_s	-2.59	-2.59	-2.59	-1.8, -2.0
	r_s	2.83	2.83	2.83	2.8, 5.0
	a_t	-1.60	-1.60	-1.60	-1.6, -2.2
	r_t	3.01	3.00	3.00	3.3, 3.5
$\Sigma^+\Sigma^+$	a_s	-85.3	-63.7	-9.72	
	r_s	2.34	2.37	2.26	
$\Lambda\Lambda$	a_s	-0.821	-0.808	-0.814	
	r_s	3.78	3.83	3.80	
Ξ^0p	a_s	0.324	0.327	0.326	
	r_s	-8.93	-9.19	-9.23	
	a_t	-0.207	-0.203	-0.204	
	r_t	26.2	27.5	27.4	
$\Xi^0\Lambda$	a_s	-1.08	-1.07	-1.08	
	r_s	3.55	3.58	3.57	
	a_t	0.262	0.263	0.263	
	r_t	2.15	2.14	2.14	
$\Xi^-\Sigma^-$	a_s	-4.63	-4.70	-3.46	
	r_s	2.39	2.37	2.04	
	a_t	-3.48	-3.52	-2.81	
	r_t	2.52	2.52	2.24	
$\Xi^-\Xi^0$	a_s	-1.43	-1.43	-1.43	
	r_s	3.20	3.17	3.17	
	a_t	3.20	3.20	3.20	
	r_t	0.218	0.218	0.217	
$\Xi^-\Xi^-$	a_s		-1.43	-1.35	
	r_s		3.21	2.70	

the attraction in the 1S_0 state is stronger than that in the 3S_1 state. However, the relative strengths of attraction in the 1S_0 and 3S_1 states are different. The model FSS gives $\delta(^1S_0) - \delta(^3S_1) \approx 30^\circ$ at $p_\Sigma \approx 200$ MeV/c, while fss2 $\delta(^1S_0) - \delta(^3S_1) \approx 10^\circ$. The difference of $\delta(^1S_0) - \delta(^3S_1) \lesssim 10^\circ$ is required from many few-body calculations [102, 103, 104, 105, 106] of the s -shell Λ -hypernuclei. In Sect. 3.4.2, we will show Faddeev calculations for the hypertriton [107], using fss2, which predict that the desirable difference is only 0 - 2° .

As seen in Fig. 19(e) later, FSS predicts especially large enhancement of the total cross sections around the cusp at the ΣN threshold. This is due to a rapid increase of the ΛN 3P_1 - ΛN 1P_1 transition

around the threshold. Figure 14 displays the S -matrix $S_{ij} = \eta_{ij}e^{2i\delta_{ij}}$ for the ΛN - $\Sigma N(I = 1/2)$ 1P_1 - 3P_1 channel coupling for fss2 (upper) and FSS (lower). The FSS shows that the transmission coefficient η_{21} , which corresponds to the ΛN $^1P_1 \rightarrow \Lambda N$ 3P_1 transition, increases very rapidly around the ΣN threshold as the energy increases. This increase of the η_{21} (and the resultant decrease of the reflection coefficient η_{11}) is a common feature of our models. The strength of the transition, however, has some model dependence. The transition is stronger in FSS than in fss2. The behavior of the diagonal phase shifts is largely affected by the strength of the 1P_1 - 3P_1 channel coupling (which is directly reflected in η_{21}). The model fss2 yields a broad resonance in the ΣN 3P_1 channel, while the FSS with stronger channel coupling yields no resonance in this channel. Instead, a step-like resonance appears in the ΛN 1P_1 channel. The location of the resonance is determined by the strength of the $LS^{(-)}$ force and the strength of the attractive central force in the $\Sigma N(I = 1/2)$ channel. In the QM, the central attraction by the S mesons is enhanced by the exchange kinetic-energy kernel, which is attractive in the ΣN 3P_1 channel due to the effect of the Pauli principle. The LS and $LS^{(-)}$ forces also contribute to increase this attraction. In FSS, a single channel calculation for the $\Sigma N(I = 1/2)$ system yields a resonance in the 3P_1 state. When the channel coupling to the ΛN system is introduced, this resonance moves to the ΛN channel due to the strong $LS^{(-)}$ force generated from the FB interaction. On the other hand, the role of the FB $LS^{(-)}$ force becomes less significant in fss2, since the S -meson exchange includes only the LS contribution and no $LS^{(-)}$ contribution. This is the reason the resonance remains in the ΣN 3P_1 channel in fss2.

In spite of these quantitative differences in the coupling strength, the essential mechanism of the ΛN - $\Sigma N(I = 1/2)$ 1P_1 - 3P_1 channel coupling is the same for all of our models. It is induced by the strong FB $LS^{(-)}$ force, which directly connects the two SU_3 configurations with the $(11)_s$ and $(11)_a$ representations in the P -wave $I = 1/2$ channel. In order to determine the detailed phase-shift behavior of each channel, including the position of the P -wave resonance, one has to know the strength of the $LS^{(-)}$ force and the strength of the attractive central force in the $\Sigma N(I = 1/2)$ channel. This is possible only by the careful analysis of rich experimental data for the Λp and $\Sigma^- p$ scattering observables in the ΣN threshold region. The asymmetry parameter data for the Λp elastic scattering at $p_\Lambda = 700$ - 1,100 MeV/c are plotted in Fig. 12(b) [101].

Let us discuss another important feature of the ΛN phase shifts induced by the P -wave coupling due to the $LS^{(-)}$ force. The ΛN 1P_1 and 3P_1 phase shifts in Fig. 14 show weakly attractive behavior below the ΣN threshold. This is due to the dispersion-like (or step-like for the ΛN 1P_1 state in FSS) resonance behavior with a large width. This attraction in the P state can be observed by the forward to

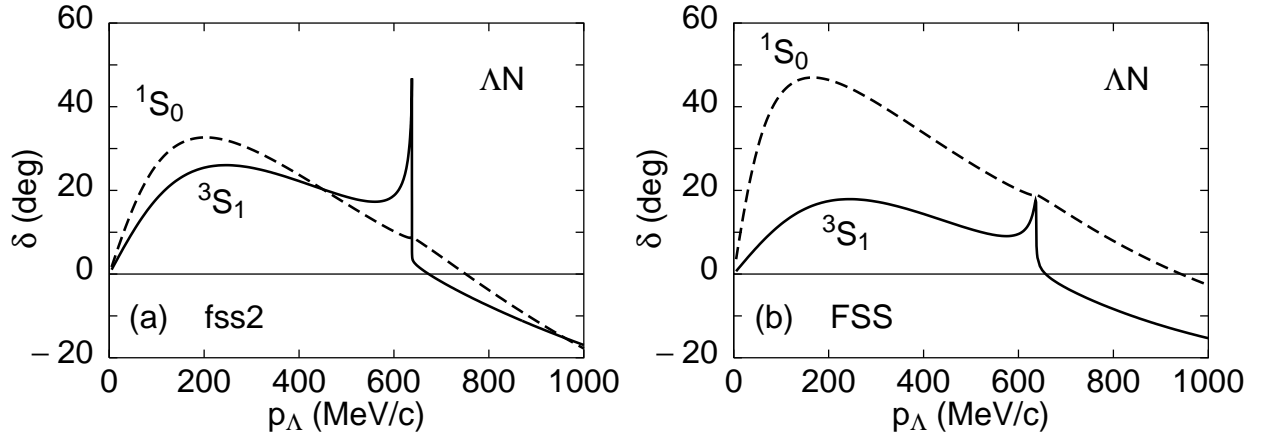


Figure 13: The ΛN 3S_1 and 1S_0 phase shifts calculated by fss2 (a) and by FSS (b).

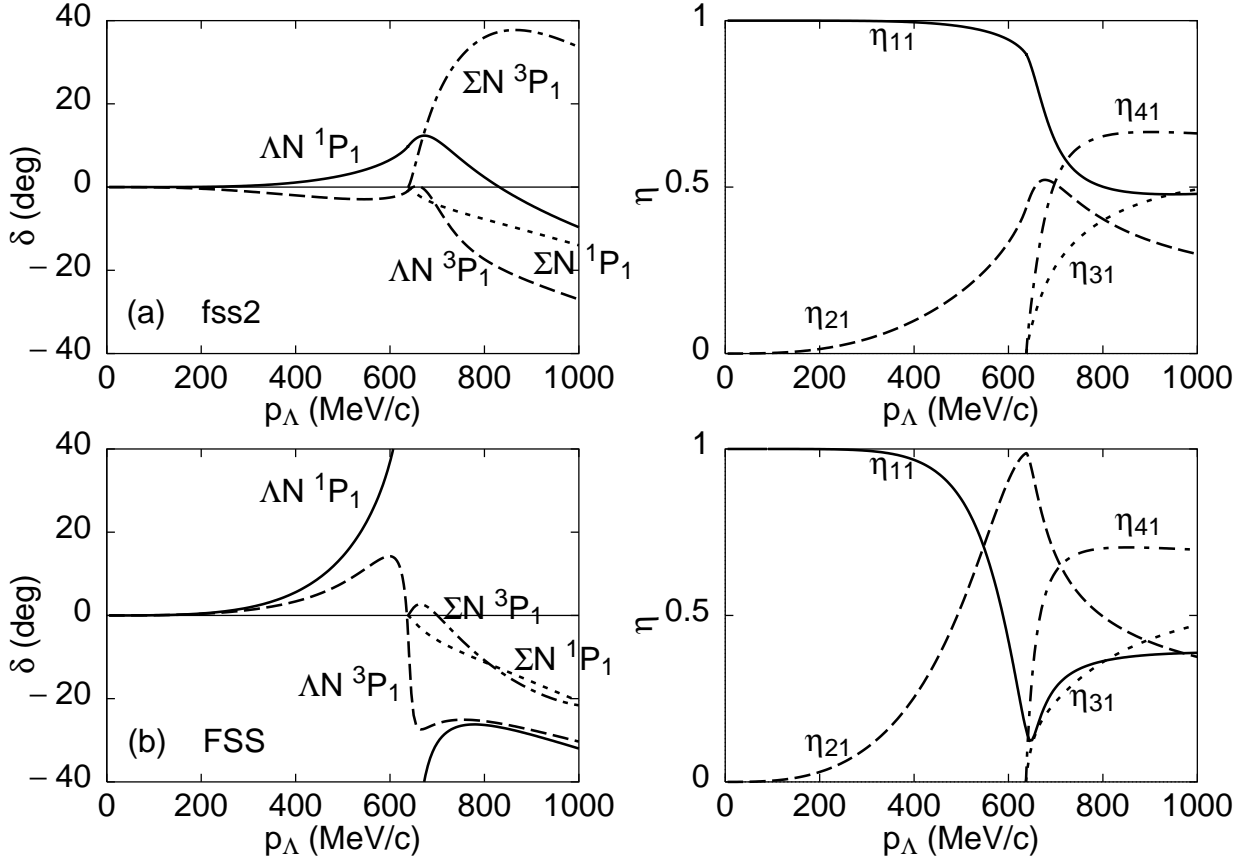


Figure 14: The S -matrix of the ΛN - $\Sigma N(I = 1/2)$ 1P_1 - 3P_1 CC system, predicted by fss2 (upper) and FSS (lower) in the isospin-basis. The diagonal phase shifts δ_{ii} (left-hand side), and the reflection and transmission coefficients η_{ij} (right-hand side) defined by $S_{ij} = \eta_{ij}e^{2i\delta_{ij}}$ are displayed. The channels are specified by 1: ΛN 1P_1 , 2: ΛN 3P_1 , 3: ΣN 1P_1 and 4: ΣN 3P_1 .

backward ratio (F/B) of the Λp differential cross sections. Both fss2 and FSS give $F/B > 1$ below the ΣN threshold [41], which implies that the P -state ΛN interaction is weakly attractive as suggested by Dalitz *et al.* [111]. A shell-model analysis of $^{13}_\Lambda\text{C}$ seems to support the attractive P -wave ΛN interaction [112]. In our QM interaction, this attraction originates from the strong ΛN - $\Sigma N(I = 1/2)$ 1P_1 - 3P_1 coupling due to the FB $LS^{(-)}$ force [41].

Some comments are in order with respect to particle-basis calculations of the Λp and Λn scatterings. From the energy spectrum of the $^3_\Lambda\text{H}$ - $^3_\Lambda\text{He}$ isodoublet Λ -hypernuclei, it is inferred that the Λp interaction is more attractive than the Λn interaction. This CSB may have its origin in the different threshold energies of the ΣN particle channels and the Coulomb attraction in the $\Sigma^- p$ channel for the Λn system. The former effect increases the cross sections of the Λp interaction and the latter the Λn interaction. However, the full calculation including the pion-Coulomb correction using the correct threshold energies yields very small difference in the S -wave phase shifts. In the energy region up to $p_\Lambda = 200$ MeV/c, the Λp phase shift is more attractive than the Λn phase shift only by less than 0.2° in the 1S_0 state, and by less than 0.4° in the 3S_1 state. This can also be seen from the results of the Λp and Λn effective range parameters in the particle basis. On the other hand, a rather large effect of CSB is found in the $\Sigma^- p$ channel as discussed in the next subsection. This is because the CSB effect is enhanced by the strong ΛN - $\Sigma N(I = 1/2)$ channel-coupling effect in the 3S_1 - 3D_1 state.

3.2.4 Σ^-p system

Since the Σ^-p system is expressed as $|\Sigma^-p\rangle = -\sqrt{2/3}|\Sigma N(I = 1/2)\rangle + \sqrt{1/3}|\Sigma N(I = 3/2)\rangle$ in the isospin basis, it is important to know first the phase-shift behavior of the $\Sigma N(I = 1/2)$ system. The SU_3 decomposition of the $\Sigma N(I = 1/2)$ state, that is, $\Sigma N(I = 1/2) = [3(11)_s - (22)]/\sqrt{10}$ for 1E and 3O and $\Sigma N(I = 1/2) = [(11)_a + (03)]/\sqrt{2}$ for 3E and 1O (see Table 5), is very useful to know the QM prediction for the phase-shift behavior in the isospin basis. Since the $(11)_s$ SU_3 state is completely Pauli forbidden, the $\Sigma N(I = 1/2)$ 1S_0 phase shift is strongly repulsive due to the exchange kinetic-energy kernel [40]. On the other hand, the $\Sigma N(I = 1/2)$ 3S_1 phase shift is expected to be attractive similarly to the ΛN 3S_1 phase shift, in so far as the effect of the FSB is not important. (Note that $\Lambda N = [-(11)_a + (03)]/\sqrt{2}$ for 3E and 1O states.) Unfortunately, the last condition is applicable only to the central force, since the one-pion tensor force introduces considerable complexities in the $\Sigma N(I = 1/2)$ - ΛN 3S_1 - 3D_1 CC problem. The strength of the $\Sigma N(I = 1/2)$ central attraction, discussed in the preceding subsection, should therefore be examined carefully after this S -wave and D -wave channel coupling is properly treated.

Figure 15 displays the 1S_0 phase shift and the S -matrix of the ΛN - $\Sigma N(I = 1/2)$ 3S_1 - 3D_1 CC state. The upper figures are the predictions by fss2, while the lower ones by FSS. The 1S_0 phase shift shows very strong Pauli repulsion, similarly to the $\Sigma N(I = 3/2)$ 3S_1 phase shift (see Fig. 10(a)). The $\Sigma N(I = 1/2)$ 3S_1 phase shift predicted by fss2 starts from 180° at $p_\Sigma = 0$, decreases moderately down to about 160° in the region $p_\Sigma \leq 100$ MeV/c. Then it rapidly decreases to about 80° at around

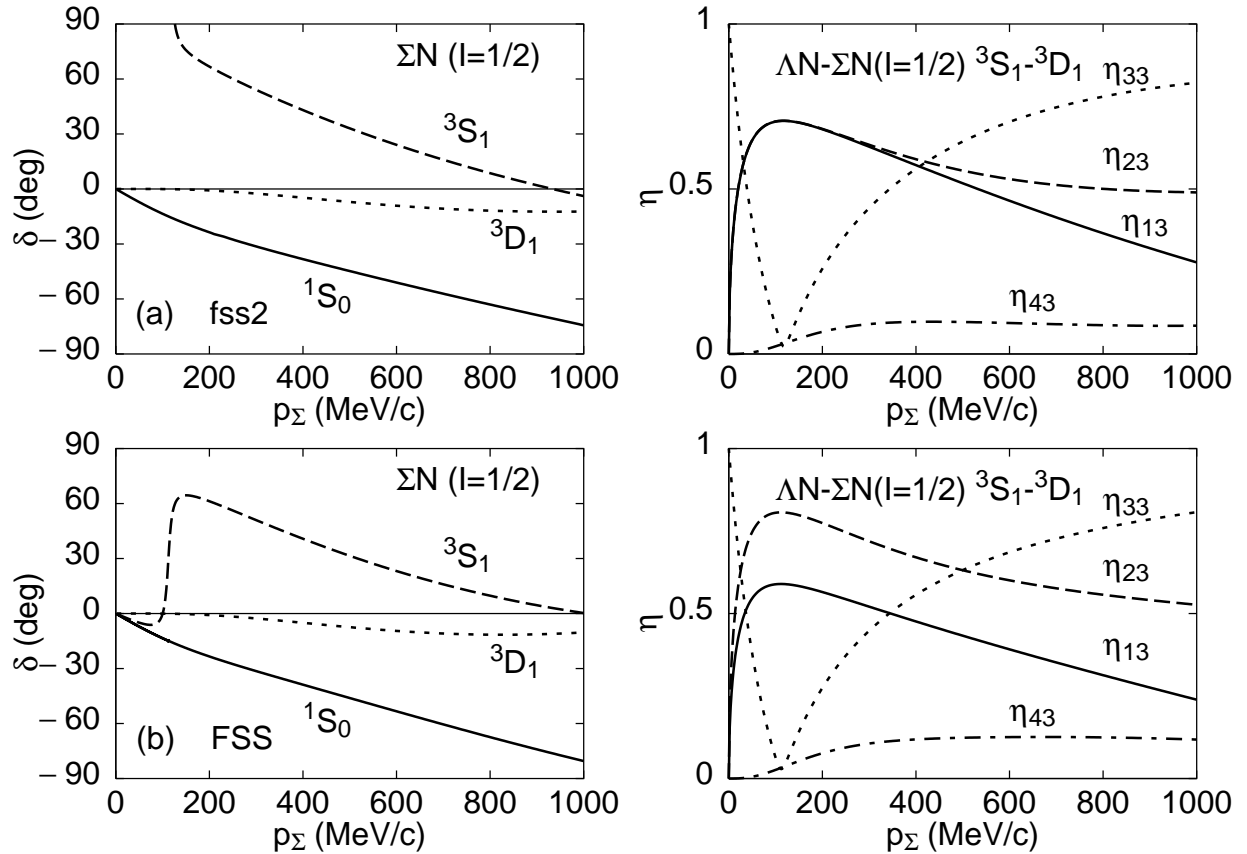


Figure 15: The same as Fig. 14 but for the 1S_0 phase shift and for the S -matrix of the ΛN - $\Sigma N(I = 1/2)$ 3S_1 - 3D_1 CC state. In the latter system, the channels are specified by 1: ΛN 3S_1 , 2: ΛN 3D_1 , 3: ΣN 3S_1 and 4: ΣN 3D_1 . The upper figures display the results by fss2, while the lower by FSS.

$p_\Sigma = 120 \text{ MeV}/c$. Beyond this momentum, a moderate decrease follows again. The situation in FSS is rather different. The 3S_1 phase shift predicted by FSS starts from 0° at $p_\Sigma = 0$, and shows a clear resonance behavior in the region $100 < p_\Sigma < 120 \text{ MeV}/c$. The peak value of the phase shift is about 60° . In spite of the very different behavior of the diagonal phase shifts predicted by fss2 and FSS, the S -matrices are found to be very similar to each other. This can be seen from the Argand diagram showing the energy dependence of the $\Sigma N(I = 1/2) ^3S_1$ S -matrix element $S_{33} = \eta_{33}e^{2i\delta_{33}}$. This implies that the strength of the central attraction in the $\Sigma N(I = 1/2)$ channel is almost the same as in fss2 and FSS.

The very strong reduction of $\eta_{33} = |S_{33}|$ in Fig. 15 is related to the large enhancement of the transmission coefficients, η_{13} and η_{23} , from the $\Sigma N(I = 1/2) ^3S_1$ ($i = 3$) to the $\Lambda N ^3S_1$ ($i = 1$) and $\Lambda N ^3D_1$ ($i = 2$) channels around $p_\Sigma = 120 \text{ MeV}/c$. These transmission coefficients are directly connected to the $\Sigma^-p \rightarrow \Lambda n$ reaction cross sections (which we call $\sigma(C)$), and the driving force for this transition is the one-pion tensor force. If we calculate the partial-wave contributions to this reaction cross section at $p_\Sigma = 160 \text{ MeV}/c$, the sum of the contributions from the transitions $^3S_1 \rightarrow ^3S_1$ and $^3S_1 \rightarrow ^3D_1$ amounts to about 120 mb both in fss2 and FSS, which is much larger than the contribution (3.5 mb) from the transition $^1S_0 \rightarrow ^1S_0$. This is in accordance with the analysis of the Λp system in the preceding subsection. Namely, there is a large cusp structure in the 3S_1 phase shift at the ΣN threshold, while a very small cusp in the 1S_0 channel. There is, however, some quantitative difference in the detailed feature of this tensor coupling between fss2 and FSS. In fss2, η_{13} and η_{23} are almost equal to each other in the momentum region where the experimental data exist ($110 \leq p_\Sigma \leq 160 \text{ MeV}/c$), whereas $\eta_{13} < \eta_{23}$ holds in FSS. The details of the cross section of the process C indicate that $\sigma(^3S_1 \rightarrow ^3S_1) \approx \sigma(^3S_1 \rightarrow ^3D_1)$ in fss2, while $\sigma(^3S_1 \rightarrow ^3S_1) < \sigma(^3S_1 \rightarrow ^3D_1)$ in FSS.

It is important to take into account the pion-Coulomb correction for more detailed evaluation of Σ^-p cross sections. In Ref. [113], we incorporated the Coulomb force of the Σ^-p channel correctly in the particle basis, but the threshold energies of the $\Sigma^0 n$ and Λn channels were not treated properly. As was discussed in Sec. 2.1, we can deal with the empirical threshold energies and the reduced masses in the RGM formalism, keeping the correct effect of the Pauli principle. Since the threshold energies and reduced masses are calculated from the baryon masses, these constitute a part of the pion-Coulomb correction in the YN interaction. Although the pion-Coulomb correction may not be the whole story of the CSB, it is certainly a first step to improve the accuracy of the model predictions calculated in the isospin basis. We can expect that the small difference of the threshold energies becomes important more and more for the low-energy Σ^-p scattering. In particular, the charge-exchange total cross section $\Sigma^-p \rightarrow \Sigma^0 n$ (which we call $\sigma(B)$) does not satisfy the correct $1/v^2$ law in the zero-energy limit, if the threshold energies of the Σ^-p and $\Sigma^0 n$ channels are assumed to be equal. We therefore used the prescription [114] to multiply the factor (k_f/k_i) , in order to get $\sigma(B)$ from the cross section calculated by ignoring the difference of the threshold energies. Here k_i and k_f are the relative momentum in the initial and final states, respectively. We will see below that this prescription is not accurate and overestimates both $\sigma(B)$ and $\sigma(C)$.

3.2.5 The inelastic capture ratio at rest in the low-energy Σ^-p scattering

The largest effect of the pion-Coulomb correction appears in the calculation of the Σ^-p inelastic capture ratio at rest, r_R [113]. This observable is defined by [114]

$$r_R = \frac{1}{4} r_{S=0} + \frac{3}{4} r_{S=1} \quad \text{with} \quad r_{S=0,1} \equiv \frac{\sigma_{(S=0,1)}(B)}{\sigma_{(S=0,1)}(B) + \sigma_{(S=0,1)}(C)} \Big|_{p_{\Sigma^-}=0}. \quad (3.2)$$

This quantity is the ratio of the production rates of the Σ^0 and Λ particles when a Σ^- particle is trapped in an atomic orbit of the hydrogen and interacts with the proton nucleus. For the accurate evaluation

Table 7: Σ^-p zero-energy total cross sections $k_i\sigma_S$ (mb fm⁻¹) for each spin-state ($S = 0$ and 1) and $k_i\sigma_T$ for reactions B: $\Sigma^-p \rightarrow \Sigma^0n$ and C: $\Sigma^-p \rightarrow \Lambda n$. The divergent factor C_0 is taken out in the Coulomb case. The inelastic capture ratio r_R at rest and r_F in flight are also given. Two versions of our quark model, FSS and fss2, are used.

	FSS without Coulomb				fss2 without Coulomb			
	B	C	r_S, r_F	r_R	B	C	r_S, r_F	r_R
$k_i\sigma_0$	56.1	5.8	0.906	0.448	61.1	6.2	0.908	0.443
$k_i\sigma_1$	68.8	164	0.296		66.7	165	0.289	
$k_i\sigma_T$	65.6	124	0.346		65.3	125	0.343	
	FSS with Coulomb				fss2 with Coulomb			
	B	C	r_S, r_F	r_R	B	C	r_S, r_F	r_R
$(C_0)^{-1}k_i\sigma_0$	44.4	4.7	0.904	0.447	48.1	5.01	0.906	0.442
$(C_0)^{-1}k_i\sigma_1$	39.7	94.9	0.295		38.3	94.6	0.288	
$(C_0)^{-1}k_i\sigma_T$	40.9	72.3	0.361		40.7	72.2	0.361	

of r_R , we first determine the effective range parameters of the low-energy S -matrix using the multi-channel effective range theory [113]. The calculations are performed by using the particle basis with and without the Coulomb force. The scattering-length matrices are employed in Table 7 to calculate r_R . Compared to the empirical values $r_R = 0.33 \pm 0.05$ [115], 0.474 ± 0.016 [116] and 0.465 ± 0.011 [117], we find that $r_R = 0.442$ predicted by fss2 is slightly smaller than the recent values between 0.45 and 0.49. The contribution from each spin state is also listed in Table 7. We find $r_{S=0} \approx 0.9$, which indicates that the $\sigma(C)$ is very small in comparison with the $\sigma(B)$ in the spin-singlet state. On the other hand, $r_{S=1} \approx 0.29$ implies that most of the ΣN - ΛN channel coupling takes place in the spin-triplet state. Here again the one-pion tensor force is very important in the $\Sigma N(I = 1/2)$ - ΛN 3S_1 - 3D_1 CC problem. We also find that the effect of the Coulomb force plays a minor role for this ratio [113].

The Σ^-p inelastic capture ratio in flight r_F , predicted by fss2 in the full calculation, is illustrated in Fig. 16. Unlike r_R , this quantity is defined directly using the total cross sections $\sigma_T(B) = (1/4)\sigma_0(B) + (3/4)\sigma_1(B)$ and $\sigma_T(C) = (1/4)\sigma_0(C) + (3/4)\sigma_1(C)$:

$$r_F = \frac{\sigma_T(B)}{\sigma_T(B) + \sigma_T(C)} . \quad (3.3)$$

This quantity is sensitive to the relative magnitudes of the $\Sigma^-p \rightarrow \Sigma^0n$ and $\Sigma^-p \rightarrow \Lambda n$ total cross sections. In the momentum region of $p_\Sigma \geq 100$ MeV/ c , the r_F calculated in the particle basis changes

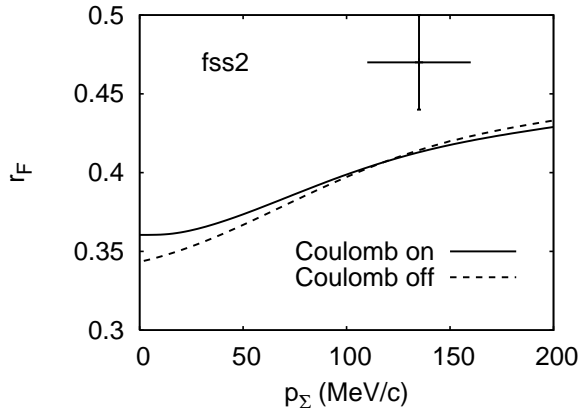


Figure 16: Σ^-p inelastic capture ratio in flight r_F , predicted by fss2, as a function of the incident momentum p_Σ . Calculation is made in the particle basis with (solid curve) and without (dashed curve) the Coulomb force.

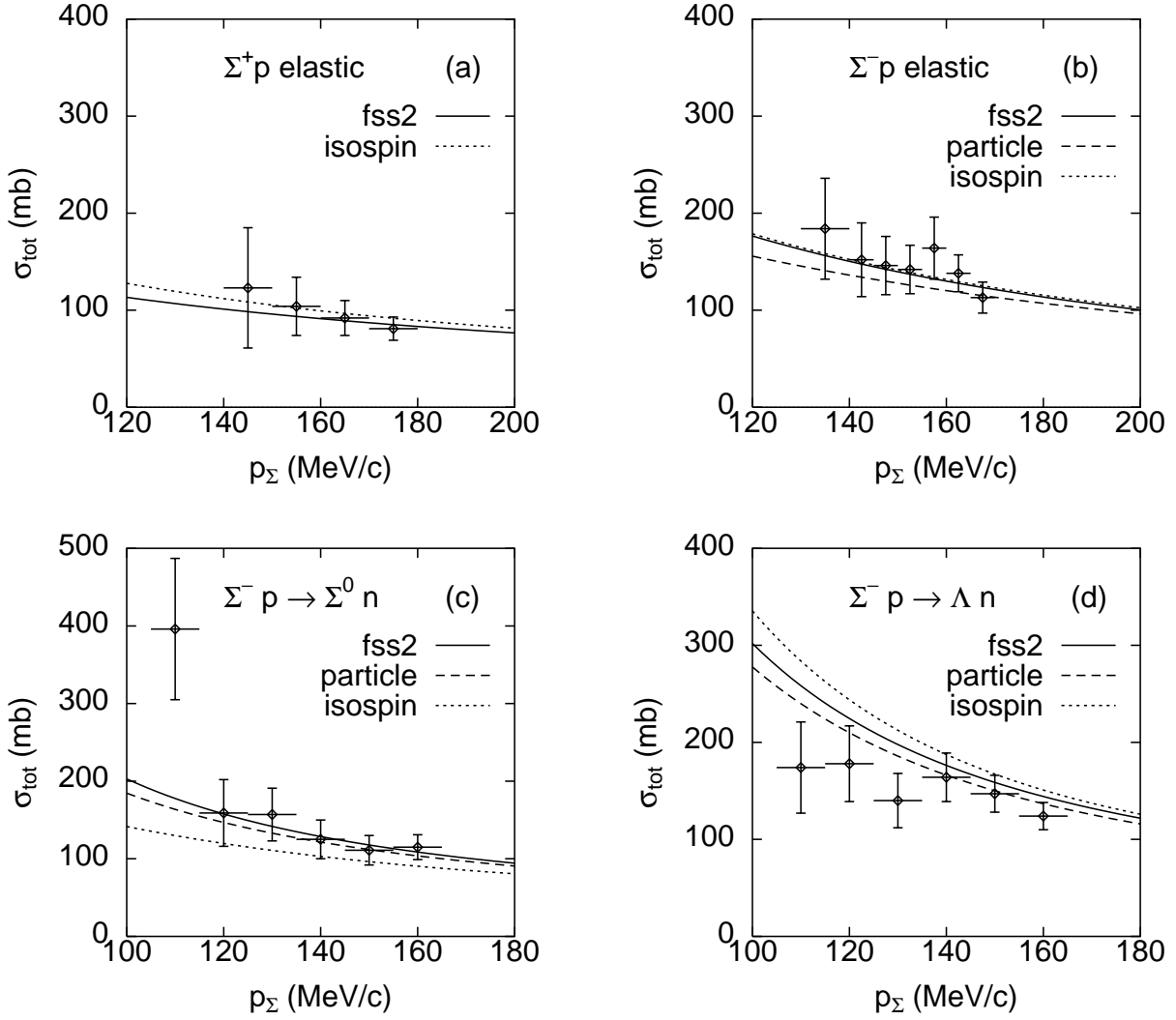


Figure 17: Calculated low-energy Σ^+p and Σ^-p scattering total cross sections by fss2, compared with experimental data: (a) Σ^+p elastic. (b) Σ^-p elastic. (c) $\Sigma^-p \rightarrow \Sigma^0n$ charge-exchange. (d) $\Sigma^-p \rightarrow \Lambda n$ reaction cross sections. Predictions in the particle basis without the Coulomb force (dashed curves), and those in the isospin basis (dotted curves) are also shown. The experimental data are taken from [119] for (a) and (b), and from [118] for (c) and (d).

little, irrespective of whether the Coulomb force is included or not. The empirical value of r_F averaged in the interval $p_{\Sigma} = 110 - 160$ MeV/c is $r_F = 0.47 \pm 0.03$ [118], as shown in Fig. 16 by a cross. The prediction of fss2, $r_F = 0.42$, is too small, which is the same feature as observed in FSS ($r_F = 0.41$) [113]. The main reason for this disagreement is that our $\Sigma^-p \rightarrow \Lambda n$ cross sections are too large.

3.2.6 YN cross sections

Figure 17 displays the low-energy Σ^-p and Σ^+p cross sections predicted by fss2. The results of three different calculations are shown; they are in the particle basis including the Coulomb force (solid curves), in the particle basis without the Coulomb force (dashed curves), and in the isospin basis (dotted curves). The effect of the correct threshold energies and the Coulomb force is summarized as follows. In the Σ^+p scattering, the effect of the repulsive Coulomb force reduces the total cross sections by 11 - 6 mb in

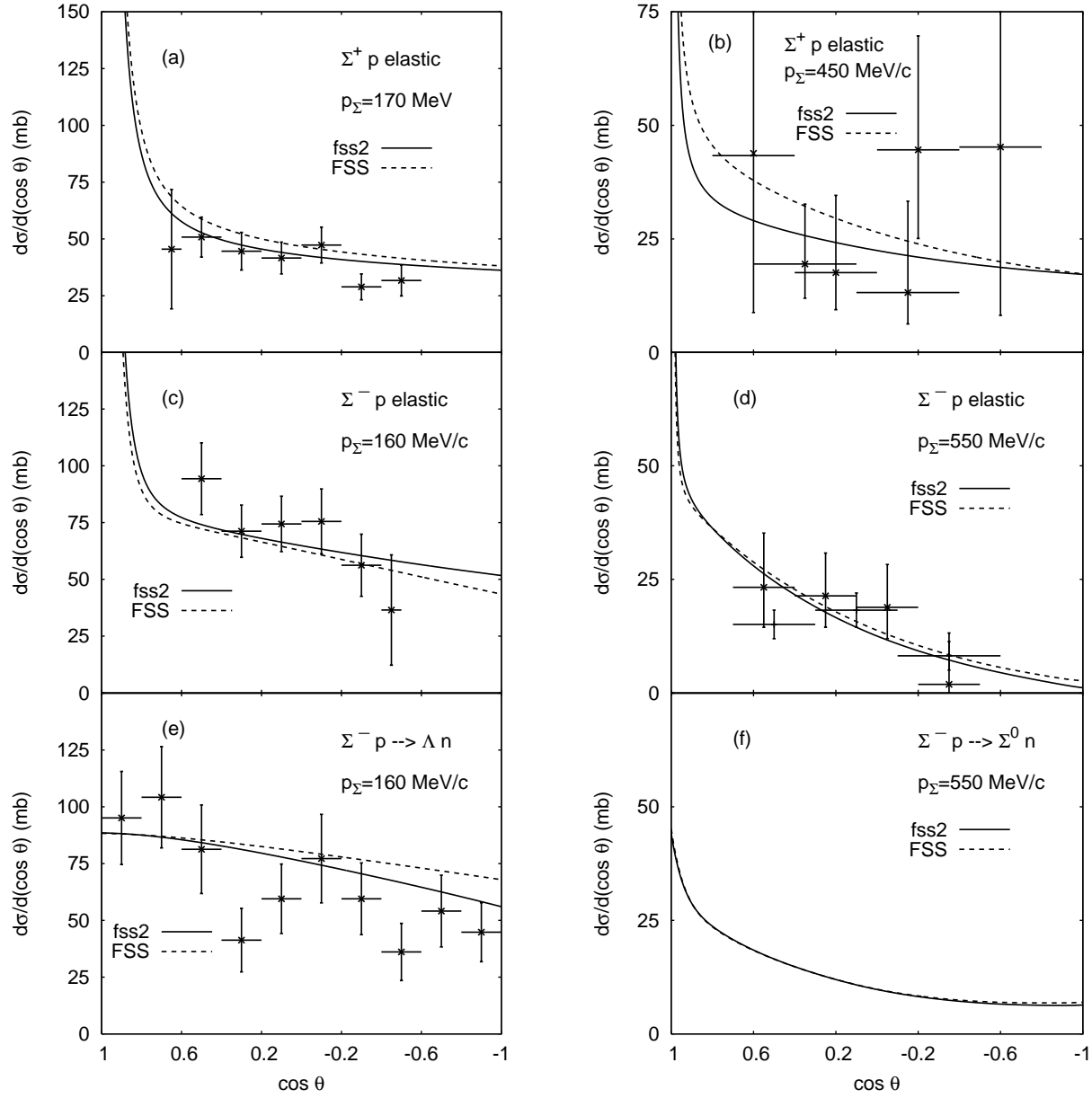


Figure 18: Calculated Σ^+p and Σ^-p differential cross sections by fss2 (solid curves) and FSS (dashed curves), compared with the experimental angular distributions: (a) Σ^+p elastic scattering at $p_\Sigma = 170$ MeV/c. (b) The same as (a) but at $p_\Sigma = 450$ MeV/c. (c) Σ^-p elastic scattering at $p_\Sigma = 160$ MeV/c. (d) The same as (c) but at $p_\Sigma = 550$ MeV/c. (e) $\Sigma^-p \rightarrow \Lambda n$ differential cross sections at $p_\Sigma = 160$ MeV/c. (f) $\Sigma^-p \rightarrow \Sigma^0 n$ differential cross sections at $p_\Sigma = 550$ MeV/c. The experimental data are taken from [118] for (a), from [120, 121] for (b), from [119] for (c) and (e), and from [122] for (d).

the momentum range $p_\Sigma = 140 - 180$ MeV/c. On the other hand, the attractive Coulomb force in the incident Σ^-p channel increases all the cross sections. An important feature of the present calculation is the effect of using the correct $\Sigma^0 n$ threshold energy. It certainly increases the $\Sigma^-p \rightarrow \Sigma^0 n$ charge-exchange cross section, but the prescription to multiply the factor (k_f/k_i) overestimates this effect. The real increase is about $1/2 - 2/3$ of this estimation. Furthermore, we find that this change is accompanied with the fairly large decrease of the Σ^-p elastic and $\Sigma^-p \rightarrow \Lambda n$ reaction cross sections. Apparently, this effect is due to the conservation of the total flux. The net effect of the Coulomb and threshold energies

becomes almost zero for the Σ^-p elastic scattering. The charge-exchange reaction cross section largely increases, and the $\Sigma^-p \rightarrow \Lambda n$ reaction cross section decreases moderately. The result of fss2 agrees with the experimental data reasonably well, although the $\Sigma^-p \rightarrow \Lambda n$ total reaction cross sections are somewhat too large.

Figure 18 compares the differential cross sections calculated by fss2 and FSS with experiment. For Σ^+p and Σ^-p elastic differential cross sections, the recent data taken at KEK [120, 121, 122] are also compared. The agreement between theory and experiment is satisfactory. We display in Fig. 19 the total cross sections of the NN and YN scatterings in a wide energy range. The solid curves denote the fss2 results, while the dashed curves the FSS ones. The “total” cross sections in the charged channels, pp , Σ^+p , and Σ^-p , are calculated by integrating the differential cross sections over the angles from $\cos\theta_{\min} = 0.5$ to $\cos\theta_{\max} = -0.5$. In the NN total cross sections, the effect of the inelastic channel is rather small up to $T_{\text{lab}} = 400$ MeV. For the YN total cross sections, the pion-Coulomb correction is important only for the charged channels and the low-energy $\Sigma^-p \rightarrow \Sigma^0 n$ reaction cross sections.

3.2.7 G -matrix calculations

Figure 20 shows various saturation curves for symmetric nuclear matter calculated using the QTQ prescription or the continuous prescription for intermediate spectra. The results with the Paris potential [84] and the Bonn B potential [123] are also shown for comparison. Since the short-range part of our QM interaction is described mainly by the quark-exchange mechanism, its non-local character is entirely different from the phenomenological or V-meson exchange pictures in the standard meson-exchange models. In spite of this large difference the saturation point of the QM interaction does not deviate much from the Coester band, which is similar to other realistic meson-exchange potentials.

The momentum dependence of the nucleon, Λ , and Σ s.p. potentials $U_B(q)$ obtained with the continuous prescription is shown in Fig. 21 at three densities $\rho = 0.5\rho_0$, $0.7\rho_0$ and ρ_0 , where $\rho_0 = 0.17 \text{ fm}^{-3}$ is the normal nucleon density. (These densities correspond to $k_F = 1.07$, 1.2 and 1.35 fm^{-1} , respectively.) The results of the Nijmegen soft-core potential NSC89 [124] calculated by Schulze *et al.* [125] are also shown. The corresponding figures of the s.p. potentials calculated by FSS are given in Figs. 2 - 5 of Ref. [45]. We see that the nucleon s.p. potential $U_N(q)$ given by fss2 is very similar to that of FSS except for the higher momentum region $q \geq 3 \text{ fm}^{-1}$. As already discussed, too attractive behavior of FSS in this momentum region is corrected in fss2, owing to the effect of the momentum-dependent Bryan-Scott terms involved in the S-meson and V-meson exchange EMEP's. The saturation curve in Fig. 20 shows that this improvement of the s.p. potential in the high-momentum region is favorable to move the saturation density to the lower side, as long as the calculation is carried out with the continuous prescription. On the other hand, the saturation curve with the QTQ prescription alters significantly between FSS and fss2. The fss2 prediction with the QTQ prescription is very similar to that of the Bonn model-B potential. It is interesting to note that the fss2 result is rather close to Bonn model-C for the deuteron properties (see Table 3), but to model-B for the nuclear saturation properties. The model-B has a weaker tensor force than the model-C, which is a favorable feature for the nuclear saturation properties.

Figures 21(b) and 21(c) display the momentum dependence of the Λ and Σ s.p. potentials in nuclear matter, which are obtained from the QM G -matrices of fss2. We find that the $U_\Lambda(q)$ predicted by fss2 and FSS (shown in Fig. 3 of [45]) are again very similar for $q \leq 2 \text{ fm}^{-1}$. The depth of the $U_\Lambda(q)$ at $q = 0$ is 48 MeV (fss2) and 46 MeV (FSS) in the continuous prescription. This value is slightly more attractive than the value expected from the experimental data of Λ -hypernuclei [126]. On the other hand, the Σ s.p. potential is repulsive in the QM, reflecting the characteristic repulsion in the $^3S_1 + ^3D_1$ channel of the isospin $I = 3/2$ state (the Pauli repulsion). The depth of the $U_\Sigma(q)$ at $q = 0$ is 8 MeV (fss2) and 20 MeV (FSS). The repulsive feature of the Σ s.p. potential is supported by Dabrowski's analysis [127] of the (K^-, π^\pm) experimental data at BNL [128]. Recently, inclusive (π^-, K^+) spectra corresponding to

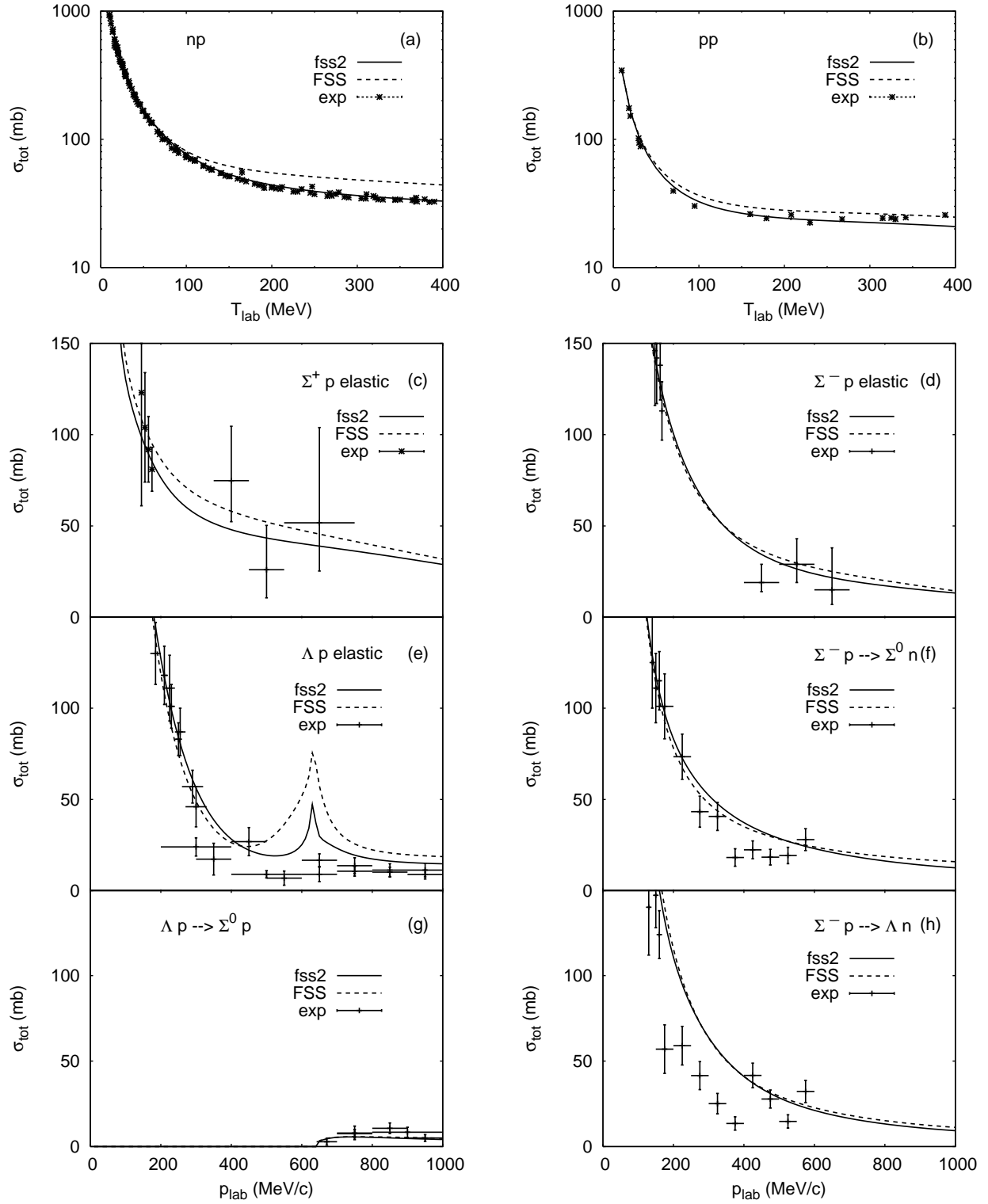


Figure 19: Calculated NN and YN total cross sections by fss2 (solid curves) and FSS (dashed curves), compared with the experimental data. The calculations are made in the particle basis. The experimental data are taken from [61] for NN , from [108, 109, 110] for Λp , from [118, 120, 121] for $\Sigma^+ p$, and from [117, 119, 122] for $\Sigma^- p$ scattering.

the Σ formation were measured at KEK [129, 130] with better accuracy. These data are satisfactorily reproduced using a repulsive Σ -nucleus potential whose strength is about 30 MeV [131].

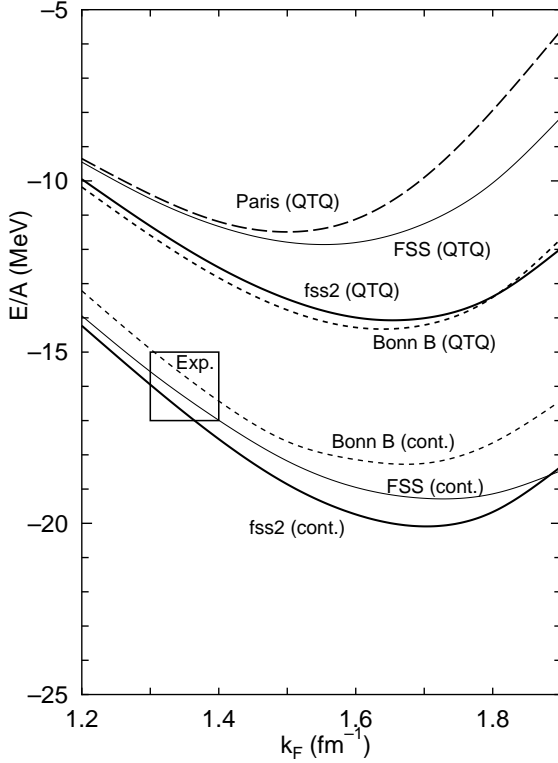


Figure 20: Nuclear matter saturation curves obtained for fss2 and FSS, together with the results of the Paris potential [84] and the Bonn model-B (Bonn B) potential [85]. The choice of the intermediate spectra is specified by “QTQ” and “cont.” for the *QTQ* prescription and the continuous choice, respectively. The result for the Bonn B potential in the continuous choice is taken from the non-relativistic calculation in Ref. [123].

The partial wave contributions to $U_\Lambda(q=0)$ and $U_\Sigma(q=0)$ in symmetric nuclear matter at $k_F = 1.35 \text{ fm}^{-1}$ are tabulated in Table 8, together with the results of FSS [45] and NSC89 [125]. For the Λ s.p. potential, the characteristic feature of fss2 in comparison with FSS appears in the less attractive 1S_0 state and in the more attractive 3S_1 state. The partial wave contributions of fss2 is very similar to those of NSC89, except for the $^3S_1 + ^3D_1$ contribution. The extra attraction of fss2, compared to NSC89, in the Λ s.p. potential comes mainly from this channel (15 - 16 MeV). This is probably because the tensor coupling is stronger in fss2 than in NSC89. A minor excess of the attraction comes from the $^1P_1 + ^3P_1$ and $^3P_2 + ^3F_2$ states (2 - 3 MeV). In $U_\Sigma(q=0)$, the reduction of repulsion from 20 MeV in FSS

Table 8: Λ and Σ s.p. potentials in nuclear matter with $k_F = 1.35 \text{ fm}^{-1}$, calculated from fss2 (FSS [45]) G -matrices in the continuous prescription for intermediate spectra. Predictions of the Nijmegen soft-core potential NSC89 [124] are also shown for comparison [125].

	$U_\Lambda(0)$ [MeV]		$U_\Sigma(0)$ [MeV]			
	fss2 (FSS)	NSC89	fss2 (FSS)		NSC89	
I	1/2	1/2	1/2	3/2	1/2	3/2
1S_0	-14.8 (-20.1)	-15.3	6.7 (6.1)	-9.2 (-8.8)	6.7	-12.0
$^3S_1 + ^3D_1$	-28.4 (-21.2)	-13.0	-23.9 (-20.2)	41.2 (48.2)	-14.9	6.7
$^1P_1 + ^3P_1$	2.1 (0.4)	3.6	-6.5 (-7.0)	3.3 (4.0)	-3.5	3.9
3P_0	-0.4 (0.5)	0.2	2.9 (3.0)	-2.2 (-2.3)	2.6	-2.0
$^3P_2 + ^3F_2$	-5.7 (-4.6)	-4.0	-1.6 (-1.3)	-2.5 (-1.2)	-0.5	-1.9
subtotal			-23.8 (-21.0)	31.3 (40.8)	-9.8	-5.5
total	-48.2 (-46.0)	-29.8	7.5 (19.8)		-15.3	

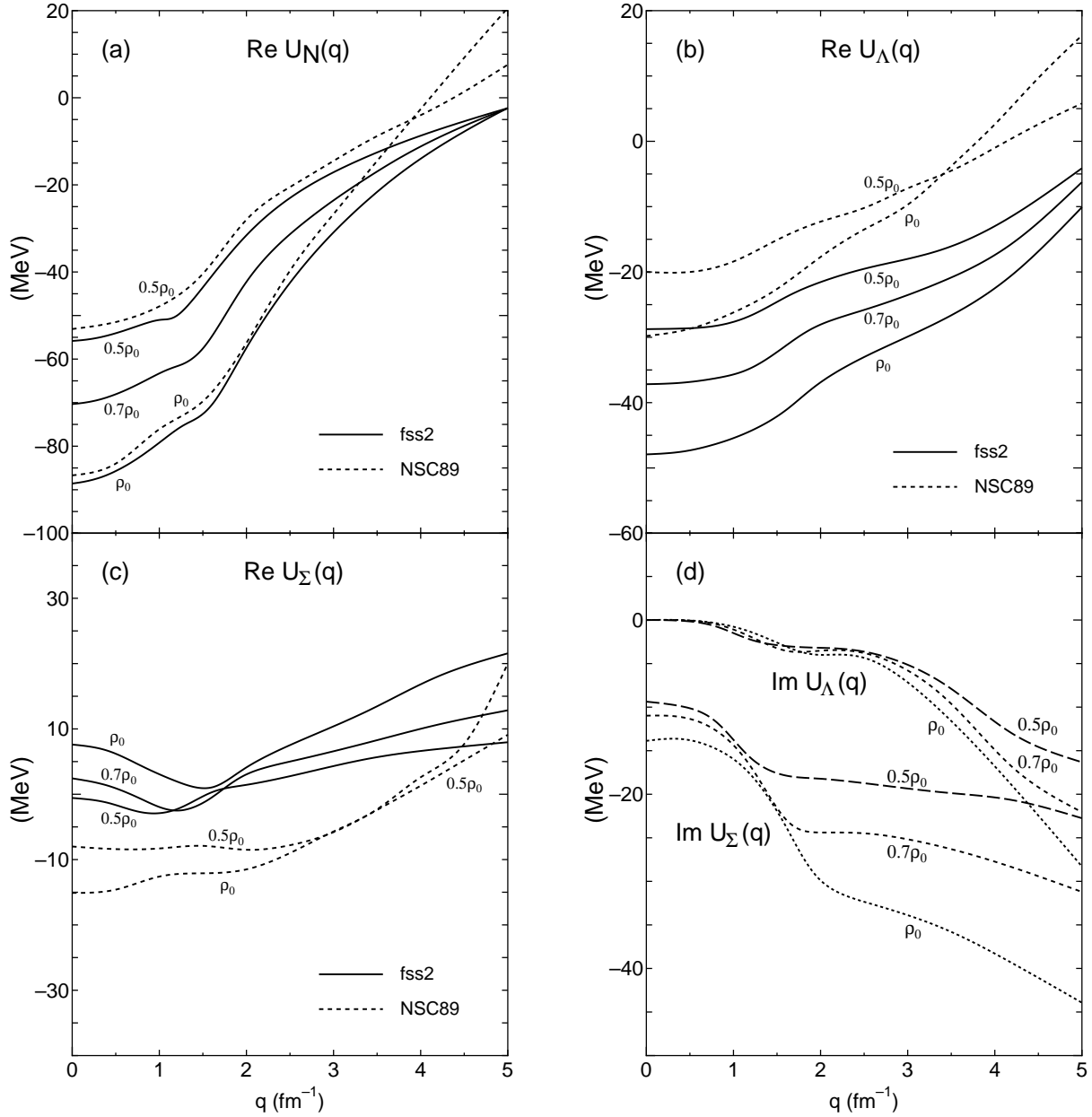


Figure 21: (a) The nucleon s.p. potential $U_N(q)$ in nuclear matter in the continuous choice for intermediate spectra. Predictions by fss2 for three densities $\rho = 0.5\rho_0$, $0.7\rho_0$ and ρ_0 are shown. Here the normal density ρ_0 corresponds to $k_F = 1.35 \text{ fm}^{-1}$. The dashed curve is the result achieved by Schulze *et al.* [125] with the Nijmegen soft-core NN potential NSC89 [124]. (b) The same as (a) but for the Λ s.p. potential $U_\Lambda(q)$. (c) The same as (a) but for the Σ s.p. potential $U_\Sigma(q)$. (d) The same as (b) and (c), but for the imaginary part of the Λ and Σ s.p. potentials $U_B(q)$ predicted by fss2.

to 8 MeV in fss2 is mainly brought about by the 7 MeV reduction of the $I = 3/2 \ ^3S_1 + ^3D_1$ repulsion and by the 4 MeV increase of the $I = 1/2 \ ^3S_1 + ^3D_1$ attraction. The latter feature is again related to the strong tensor coupling in fss2. On the other hand, the repulsive contribution of the $I = 3/2 \ ^3S_1 + ^3D_1$ state in NSC89 is very weak, since this channel has a broad resonance around $p_\Sigma = 500 - 800 \text{ MeV}/c$. (See Fig. 1 of [99].) It is interesting to note that the attractive contributions to the Λ and Σ s.p. potentials from the $I = 1/2 \ ^3S_1 + ^3D_1$ state is more than 10 MeV stronger in fss2 than in NSC89.

Table 9: Decomposition of the Scheerbaum factors obtained by fss2 at $k_F = 1.35 \text{ fm}^{-1}$ into various contributions. The values in parentheses are given by FSS. The unit is MeV fm^5 .

	$I = 1/2$		$I = 3/2$	
	odd	even	odd	even
LS	-19.1 (-17.1)	-0.2 (0.6)	—	—
$S_\Lambda LS^{(-)}$	7.9 (12.7)	0.3 (0.3)	—	—
total	-11.1 (-3.5)			
LS	1.3 (2.7)	-0.3 (0.1)	-12.4 (-11.9)	-1.5 (-1.5)
$S_\Sigma LS^{(-)}$	-9.6 (-10.5)	-0.4 (-0.6)	-0.4 (0.1)	-0.1 (-0.0)
total	-23.3 (-21.8)			

Although NSC89 is considered to have a strong ΛN - ΣN coupling, the ΛN - ΣN coupling of fss2 is even stronger. The imaginary parts of the Λ and Σ s.p. potentials are shown in Fig. 21(d) for fss2. These results are similar to those of FSS (see Fig. 4 of ref. [45]). In particular, $\text{Im } U_\Sigma(q=0)$ at $k_F = 1.35 \text{ fm}^{-1}$ is -14.4 MeV in fss2 and -18.4 MeV in FSS. These results are in accord with the calculations by Schulze *et al.* [125] for NSC89.

Using the G -matrix solution of fss2, we can calculate the Scheerbaum factor S_B [63], which represents the strength of the s.p. spin-orbit potential defined as [46]

$$U_B^{\ell s}(r) = -\frac{\pi}{2} S_B \frac{1}{r} \frac{d\rho(r)}{dr} \boldsymbol{\ell} \cdot \boldsymbol{\sigma}. \quad (3.4)$$

The value of S_B is momentum-dependent, but here we only discuss $S_B(q=0)$. The QM description of the YN interaction contains the antisymmetric spin-orbit ($LS^{(-)}$) component, and the large cancellation between the LS and $LS^{(-)}$ contributions in the ΛN isospin $I = 1/2$ channel leads to a small s.p. spin-orbit potential for the Λ -hypernuclei. The FSS gives a ratio $S_\Lambda/S_N \leq 1/10$ [46]. The cancellation of these two contributions is less prominent in fss2, since the S-meson EMEP yields the ordinary LS component but no $LS^{(-)}$ component (see Sec. 2.2). Since the total strength of the LS force is fixed in the NN scattering, the FB contribution of the LS force is somewhat reduced. This can easily be seen from the simple formula given in Eq. (52) of [46], which shows that in the Born approximation the FB LS contribution to the Scheerbaum factor is determined only by a single strength factor $\alpha_S x^3 m_{ud} c^2 b^5$ with $x = (\hbar/m_{ud}cb)$. The value of this factor is 29.35 MeV fm^5 for fss2, which is just $3/5$ of the FSS value 48.91 MeV fm^5 . The density dependence of S_B is found to be rather weak. At the normal density ρ_0 with $k_F = 1.35 \text{ fm}^{-1}$, we obtain $S_N = -42.4$, $S_\Lambda = -11.1$, $S_\Sigma = -23.3$ (MeV fm^5) for fss2, resulting in $S_\Lambda/S_N \approx 0.26$ and $S_\Sigma/S_N \approx 0.55$. The ratios S_Λ/S_N and S_Σ/S_N become slightly smaller for lower densities. Table 9 lists the contributions from the LS and $LS^{(-)}$ components in the even- and odd-parity states as well as $I = 1/2$ and $I = 3/2$ channels for $k_F = 1.35 \text{ fm}^{-1}$. The parenthesized figures are the predictions by FSS. A prominent difference between fss2 and FSS appears only in the 3O contribution of S_Λ . Namely, the 5 MeV reduction of the 3O $LS^{(-)}$ contribution and the 2 MeV enhancement of the 3O LS contribution, which explains the change from $S_\Lambda = -3.5$ in FSS to $S_\Lambda = -11.1$ in fss2. In the recent experiment at BNL, very small spin-orbit splitting is reported in the energy spectra of ${}^9_\Lambda\text{Be}$ and ${}^{13}_\Lambda\text{C}$ [132, 133]. A theoretical calculation of these ΛN spin-orbit splittings using OBEP ΛN interactions is carried out in Ref. [134]. More detailed analysis of the $\alpha\alpha\Lambda$ system for ${}^9_\Lambda\text{Be}$ is made in Sec. 3.5.1, in the three-cluster Faddeev formalism using our QM ΛN interaction [135, 136].

3.3 Interactions for other octet-baryons

3.3.1 $S = -2$ systems

[$\Lambda\Lambda$ system]

Although the direct measurement of $\Lambda\Lambda$ scattering is not possible, the observation of double- Λ hypernuclei gives an important information on the $\Lambda\Lambda$ interaction. Several candidates of double- Λ hypernuclei are already found [137, 138, 139, 140]. Among them, the sequential decay process of ${}^6_{\Lambda\Lambda}\text{He}$ (NAGARA event), found in the emulsion/scintillating-fiber hybrid experiment at KEK, has given a definite value for the binding energy of the two- Λ hyperons, $B_{\Lambda\Lambda}$, without ambiguities arising from the possibilities of excited states. The $\Lambda\Lambda$ interaction energy extracted from $\Delta B_{\Lambda\Lambda}({}^6_{\Lambda\Lambda}\text{He}) = B_{\Lambda\Lambda}({}^6_{\Lambda\Lambda}\text{He}) - 2B_{\Lambda}({}^5_{\Lambda}\text{He})$ is $\Delta B_{\Lambda\Lambda}({}^6_{\Lambda\Lambda}\text{He}) = 1.01 \pm 0.20^{+0.18}_{-0.11}$ MeV [137]. This value is considerably small compared with a similar measure of the ΛN interaction strength, $\Delta B_{\Lambda N}({}^5_{\Lambda}\text{He}) = B_{\Lambda N}({}^5_{\Lambda}\text{He}) - B_{\Lambda}({}^4_{\Lambda}Z) - B_N({}^4\text{He}) = B_{\Lambda}({}^5_{\Lambda}\text{He}) - B_{\Lambda}({}^4_{\Lambda}Z) = 1.73 \pm 0.04$ MeV, where $B_{\Lambda}({}^4_{\Lambda}Z)$ stands for a proper spin and charge average over the binding energies of the 0^+ and 1^+ states in ${}^4_{\Lambda}\text{H}$ and ${}^4_{\Lambda}\text{He}$ [141].

We display in Figs. 22 and 23 the 1S_0 phase shifts of the $\Lambda\Lambda$ - ΞN - $\Sigma\Sigma$ system with isospin $I = 0$, calculated by FSS and fss2, respectively. The $\Lambda\Lambda$ - ΞN CC effect gives a step-like resonance (FSS) and a cusp (fss2) at the ΞN threshold region. The coupling effect to the $\Sigma\Sigma$ channel also gives cusps at the $\Sigma\Sigma$ threshold. The $\Lambda\Lambda$ 1S_0 phase shift rises up to about 40° for FSS and 18° for fss2. The $\Lambda\Lambda$ T -matrix of FSS yields $\Delta B_{\Lambda\Lambda} \approx 3.7$ MeV and that of fss2 ≈ 1.4 MeV, as will be shown in the Faddeev calculations of the ${}^6_{\Lambda\Lambda}\text{He}$ system. (See Table 17.) Another estimate of $\Delta B_{\Lambda\Lambda}({}^6_{\Lambda\Lambda}\text{He})$, using the CC G -matrices by fss2, yields $\Delta B_{\Lambda\Lambda} = 1.12 - 1.24$ MeV, if the Brueckner rearrangement energy of the α -cluster is properly taken into account [142]. These calculations indicate that fss2 is more appropriate than FSS, at least for the strength of the $\Lambda\Lambda$ attraction in ${}^6_{\Lambda\Lambda}\text{He}$.

It is important to understand the origin of the attraction of the 1S_0 $\Lambda\Lambda$ interaction. In the single-channel calculation, it is convenient to display this interaction in terms of the effective local potential used in Refs. [97, 35, 98], based on the WKB-RGM approximation. Figure 24 shows the phase-shift equivalent local potentials at $p_{\text{lab}} = 200$ MeV/ c for the 1S_0 states of NN , ΛN and $\Lambda\Lambda$ systems, obtained

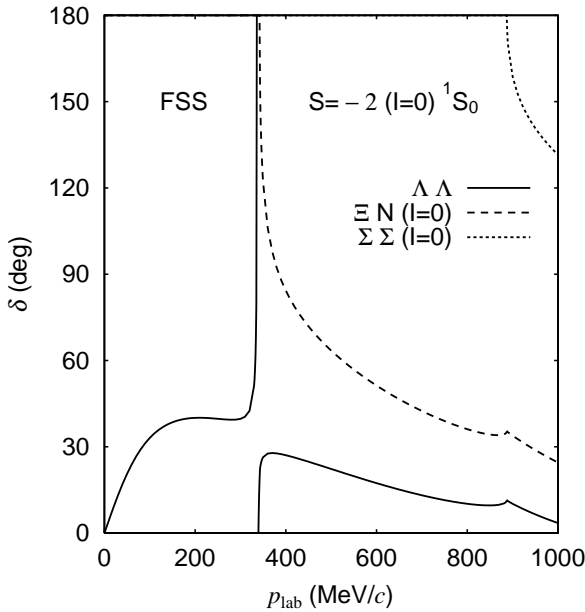


Figure 22: ${}^1S_0(I = 0)$ phase shifts, predicted by FSS, in the $\Lambda\Lambda$ - ΞN - $\Sigma\Sigma$ CC system.

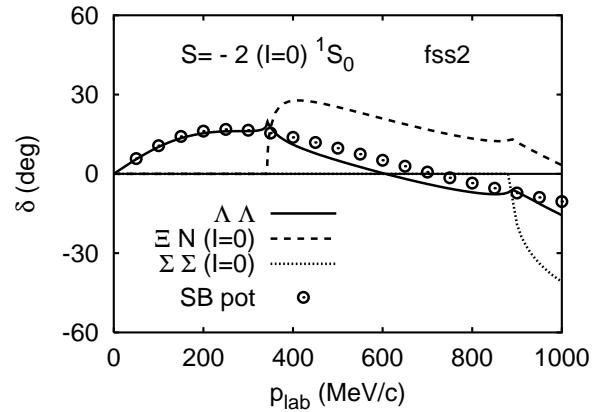


Figure 23: The same as Fig. 22, but for fss2. The single-channel phase shift of the $\Lambda\Lambda$ channel, predicted by the SB effective potential in Eq. (3.12), is also shown in circles.

by solving the transcendental equation of the single-channel RGM kernel of fss2. The single-channel 1S_0 phase shifts given by these local potentials are depicted in Fig. 25. In the low-energy region, our QM gives the attractive $\Lambda\Lambda$ and ΛN interactions which are similar to the NN one, in accordance with the discussion based on the flavor- SU_3 symmetry [98]. The different strengths of the attraction in the NN , ΛN and $\Lambda\Lambda$ systems originate from the S-meson nonet exchange, i.e., the SU_3 relations of the spin-flavor factors. On the other hand, the short-range repulsion arising mainly from the color-magnetic term of the FB interaction receives a strong effect of the FSB through the mass ratio of the s - and ud -quarks. Since the color-magnetic term contains the quark-mass dependence, $1/(m_i m_j)$, the short-range repulsion is diminished drastically if the mass ratio $\lambda = (m_s/m_{ud})$ deviates largely from unity. Consequently, the characteristics of the potential is determined by the subtle balance of the two reductions; one by the FSB in the short-range repulsion generated from the color-magnetic term and the other by the SU_3 relations in the medium-range attraction generated from the S-meson nonet exchange. The reduction of the attraction from the NN to ΛN channels suggests that the reduction of the medium-range attraction is larger than that of the short-range repulsion in fss2. This feature is also reflected when we extend the present framework from the ΛN to $\Lambda\Lambda$ systems. The relative strength of the attraction for the diagonal 1S_0 potentials of the NN , ΛN and $\Lambda\Lambda$ systems follows the relationship

$$|v_{\Lambda\Lambda}| < |v_{\Lambda N}| < |v_{NN}|. \quad (3.5)$$

This feature for the two-baryon systems including the Λ -particle is also seen in NSC97 [143].

The full 1S_0 potentials are obtained by taking into account the effect of the ΛN - ΣN channel coupling for the ΛN system and the $\Lambda\Lambda$ - ΞN - $\Sigma\Sigma$ coupling for the $\Lambda\Lambda$ system. First let us discuss the CC effect in the 1S_0 state without the EMEP. The exchange kinetic-energy, color-Coulombic and momentum-dependent Breit retardation terms do not contribute to the $\Lambda\Lambda$ - ΞN 1S_0 transition potential, because

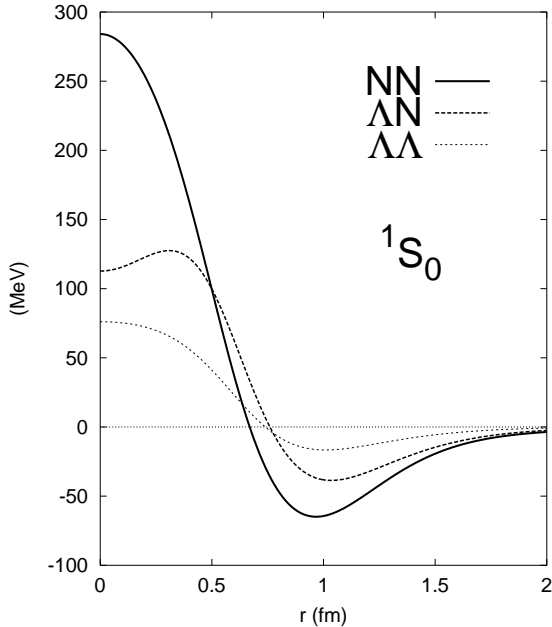


Figure 24: The 1S_0 phase-shift equivalent local potentials of single-channel NN (solid curve), ΛN (dashed curve) and $\Lambda\Lambda$ (dotted curve) systems, predicted by fss2 at $p_{\text{lab}} = 200$ MeV/ c .

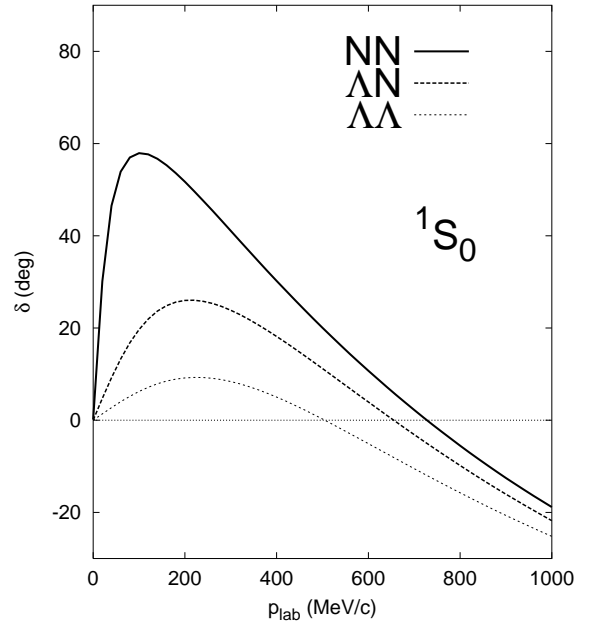


Figure 25: NN , ΛN and $\Lambda\Lambda$ 1S_0 phase shifts given by the phase-shift equivalent local potentials in Fig. 24 in the single-channel calculation.

the spin-flavor-color factors of these terms are exactly zero, as well as that of the exchange normalization kernel. Therefore the contribution from the FB interaction to this coupling potential is solely from the color-magnetic term. This coupling potential gives the sharp cusp structure for the $\Lambda\Lambda$ phase shift and the step-like resonance for the ΞN phase shift, as seen in Fig. 19 of Ref. [11]. If the coupling to the $\Sigma\Sigma$ channel is taken into account, the resonance in the ΞN channel grows up due to the strong attraction in the $\Sigma\Sigma$ channel and moves to the $\Lambda\Lambda$ channel. The actual resonance behavior is, however, sensitive to the FSB. If one neglects the FSB and set $\lambda = 1$, the CC calculation of FSS without EMEP yields a bound state of the binding energy 31 MeV, which corresponds to the H -dibaryon predicted by Ref. [144]. An introduction of the large FSB reduces the $\Lambda\Lambda$ - ΞN CC effect.

Next, we introduce EMEP's acting between quarks, and investigate how they influence the features of the channel coupling. The strange-meson exchange contributes to the $\Lambda\Lambda$ - ΞN diagram through the direct and exchange kernels in the RGM framework, whereas the non-strange-meson exchanges can contribute only through the exchange kernel. As the result, the dominant contribution from the EMEP's to the $\Lambda\Lambda$ - ΞN coupling potential is from the strange-meson exchange. This contribution has a sign opposite to that of the color-magnetic term [98, 145] and diminishes the coupling effect by the FB interaction discussed above. It turns out that the strange S meson, κ , gives the most important contribution to the $\Lambda\Lambda$ - ΞN 1S_0 coupling potential. The effect of the κ -meson exchange becomes more important as the mass becomes smaller. It should also be stressed that the spin-flavor factors of EMEP's are explicitly calculated in our QM baryon-baryon interactions. The contribution from the exchange RGM kernel of the EMEP's to the $\Lambda\Lambda$ - ΞN 1S_0 coupling matrix elements is also appreciable, as largely as about one third of the corresponding direct kernel in fss2. Namely, the following three features of the EMEP reduce the $\Lambda\Lambda$ - ΞN CC effect in the present framework; 1) the introduction of the S-meson nonet including the κ meson, 2) the comparatively small κ -meson mass, and 3) the introduction of the EMEP's not at the baryon level but at the quark level.

The above discussion explains why the $\Lambda\Lambda$ - ΞN CC effect of fss2 is smaller than other several QM's [146, 144, 147, 148]. It is related with the more realistic feature including the S-meson nonet (with $m_\kappa = 936$ MeV/ c^2) and the large FSB (with $\lambda = 1.5512$). After all, the $\Lambda\Lambda$ interaction of fss2 with the full CC effect satisfies the relationship of Eq. (3.5). This feature of the $\Lambda\Lambda$ interaction leads to the conclusion that no bound state is possible in fss2. (For FSS, the relationship Eq. (3.5) is modified to $|v_{\Lambda\Lambda}| \approx |v_{\Lambda N}| < |v_{NN}|$, but it is still insufficient to produce a bound state.) Clearly a realistic QM baryon-baryon interaction constructed by supplementing EMEP's to the FB interaction can no longer predict a deeply bound H -dibaryon state.

In Ref. [149], the $\Lambda\Lambda$ interaction is examined in the chiral constituent quark model, which is tightly constrained by the description of the non-strange sector and the strange meson and baryon spectra. They found an attractive $\Lambda\Lambda$ interaction due to the mechanism that the short-range repulsion from the Goldstone-boson and gluon exchanges are considerably reduced in the $\Lambda\Lambda$ interaction in comparison with the NN interaction. The reduction of the short-range repulsion produced from the Goldstone-boson exchange might have some relevance in the systems with more strangeness.

[ΞN interaction]

The SU_3 classification in Table 5 is useful to discuss the characteristics of the ΞN interaction. Let us first discuss the phase-shift behavior of the flavor-symmetric 1S_0 state in the single-channel calculation. The color-magnetic term is repulsive in the (22) state and attractive in the flavor-singlet (00) state. Since the weights of the (22) and (00) components in the $\Xi N(I = 0)$ 1S_0 state are comparable, the net contribution of the color-magnetic term is small in the $I = 0$ ΞN interaction due to the cancellation between these two components. The $\Xi N(I = 0)$ 1S_0 interaction is, therefore, characterized by the EMEP contribution. It turns out that the EMEP contribution produces an attractive $\Xi N(I = 0)$ 1S_0 interaction. The situation is different in the $I = 1$ state. In this channel, the leading SU_3 component

is $(11)_s$, for which the most compact $(0s)^6$ configuration gives a Pauli-forbidden state. This gives a repulsive interaction in the $\Xi N(I=1) {}^1S_0$ channel. As to the flavor-antisymmetric ${}^3S_1 - {}^3D_1$ state, the $\Xi N(I=0)$ interaction is found to be weakly attractive, characterizing the property of the pure SU_3 $(11)_a$ state. The $\Xi N(I=1)$ interaction is repulsive because of the almost-forbidden $(0s)^6$ configuration of the (30) state. It is concluded that the ΞN interaction is attractive in the $I=0$ channel, whereas it is repulsive in the $I=1$ channel [98]. The attraction of the $\Xi N(I=0) {}^1S_0$ state is strongest, and the repulsion of $\Xi N(I=1) {}^1S_0$ state is strongest.

The CC effect on the $\Lambda\Lambda$ and $\Sigma\Sigma$ configurations takes place in the $I=0 {}^1S_0$ state, while that on $\Sigma\Lambda$ in the $I=1$ state. In the former case, the attractive feature of the ΞN interaction does not change essentially. On the other hand, the effect of the channel coupling on the $\Sigma\Lambda$ configuration with $I=1$ changes rather drastically the result of the single-channel calculation. Figure 26 displays the phase shifts of the 1S_0 and 3S_1 states, calculated for the full ΞN – $\Sigma\Lambda$ – $\Sigma\Sigma$ CC system with $I=1$. In both cases, the phase shifts exhibit a prominent cusp structure at the $\Sigma\Lambda$ threshold around $p_{\text{lab}} = 600$ MeV/c and they almost vanish below the $\Sigma\Lambda$ threshold. This drastic change is due to the strong CC effect caused by the large ΞN – $\Sigma\Lambda$ coupling matrix elements. Although the effect of ΞN – $\Sigma\Lambda$ coupling predicted by the FB interaction is moderate [10], the introduction of the EMEP's reinforces it since the strange-meson exchange can contribute to the ΞN – $\Sigma\Lambda$ coupling through both of the direct and exchange Feynman diagrams [150].

Figure 27 shows the Ξ^-p and Ξ^0p total cross sections predicted by FSS (left) and fss2 (right). The calculation is made in the particle basis, including the pion-Coulomb corrections. Both of the isospin $I=0$ and $I=1$ channels contribute to the Ξ^-p cross sections, while only the channel with $I=1$ contributes to Ξ^0p (or Ξ^-n). The Ξ^0p (and Ξ^-n) total cross sections with the pure $I=1$ component are predicted to be very small below the $\Sigma\Lambda$ threshold. This behavior of the Ξ^-n total cross sections is essentially the same as the Nijmegen result [143]. On the other hand, the Ξ^-p total cross sections exhibit a typical channel-coupling behavior which is similar to that of the Σ^-p total cross sections. These features demonstrate that the $\Sigma\Lambda$ channel coupling is very important for the correct description of scattering observables, resulting in the strong isospin dependence of the ΞN interaction. It is interesting to find that the contribution of the strange-meson exchange reduces the $\Lambda\Lambda(I=0)$ – $\Xi N(I=0)$ channel coupling, while it strengthens the $\Xi N(I=1)$ – $\Sigma\Lambda(I=1)$ coupling in the QM including the FB interaction and the EMEP's. This is quite different from the OBEP models, in which both $\Lambda\Lambda$ – ΞN and ΞN – $\Sigma\Lambda$ coupling potentials are generated only from the strange-meson exchanges. Figure 27 also includes the in-medium experimental Ξ^-N total cross section around $p_{\text{lab}} = 550$ MeV/c [151], where σ_{Ξ^-N} (in

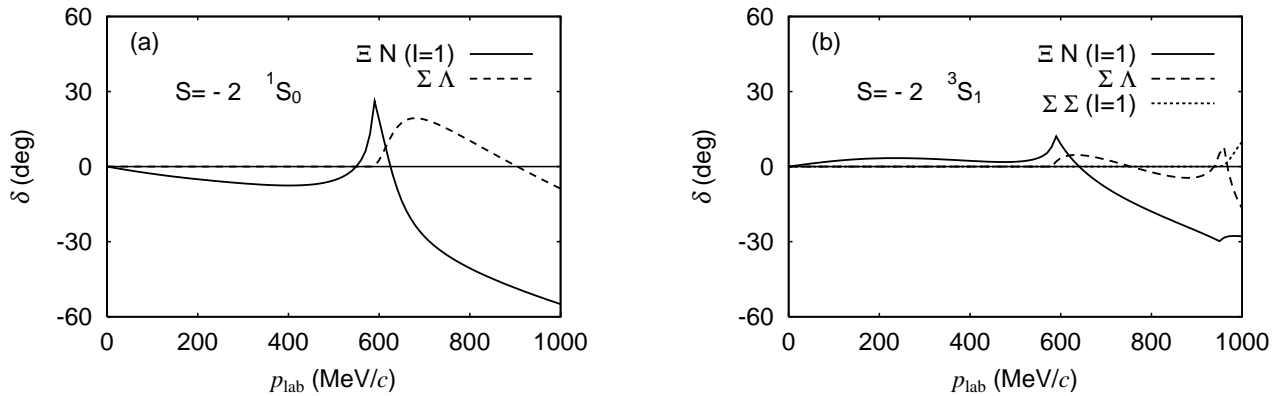


Figure 26: (a) 1S_0 phase shifts in the ΞN – $\Sigma\Lambda$ CC system with $I=1$, predicted by fss2. (b) 3S_1 phase shifts in the ΞN – $\Sigma\Lambda$ – $\Sigma\Sigma$ CC system with $I=1$, predicted by fss2.

medium) = $30 \pm 6.7_{-3.6}^{+3.7}$ mb is given. Another analysis using the eikonal approximation [152] gives $\sigma = 20.9 \pm 4.5_{-2.4}^{+2.5}$ mb, as shown by the black square in Fig. 27. The analysis also estimates the cross section ratio $\sigma_{\Xi^- p} / \sigma_{\Xi^- n} = 1.1_{-0.7-0.4}^{+1.4+0.7}$ mb. A more recent experimental analysis [153] for the low-energy $\Xi^- p$ elastic and $\Xi^- p \rightarrow \Lambda\Lambda$ total cross sections in the range of 0.2 GeV/c to 0.8 GeV/c shows that the former is less than 24 mb at 90% confidence level and the latter of the order of several mb, respectively. These results seem to favor the predictions by fss2. However, we definitely need more experimental data with high statistics. A theoretical evaluation of the in-medium cross sections is also necessary.

The P -wave phase shifts of the $\Lambda\Lambda(I=0)$, $\Xi N(I=0)$ and $\Xi N(I=1)$ scatterings are illustrated in Fig. 28 for FSS and in Fig. 29 for fss2. A step-like resonance appears in the 3P_0 states of the $\Lambda\Lambda$ channel (FSS) and the $\Xi N(I=0)$ channel (fss2). The origin of these resonances is the $\Xi N(I=0)$ 3P_0 resonance produced by the non-central forces, i.e., the tensor and LS forces. This resonance is not clearly seen in the $\Xi^- p$ total cross sections in Fig. 27, due to the small statistical weight of $J=0$. The shift of the $\Xi N(I=0)$ resonance to the $\Lambda\Lambda$ channel for FSS resembles the situation in the $\Sigma N(I=1/2)$ 3P_1 resonance, discussed in Sec. 3.2.3. If the step-like resonance in the $\Sigma N(I=1/2)$ 3P_1 channel moves to the ΛN 1P_1 channel by the ΛN - ΣN channel coupling, the Λp total cross section is enhanced in the cusp region [37, 40]. Similarly, the step-like resonance in the $\Lambda\Lambda$ 3P_0 channel due to the $\Lambda\Lambda$ - ΞN channel coupling leads to the enhanced $\Lambda\Lambda$ total cross sections by FSS in the momentum region $p_{\text{lab}} \approx 400$ MeV/c. The total cross section curves for the $\Lambda\Lambda$ scattering clearly show this situation, as displayed in Fig. 30.

[$\Sigma\Sigma$ interaction]

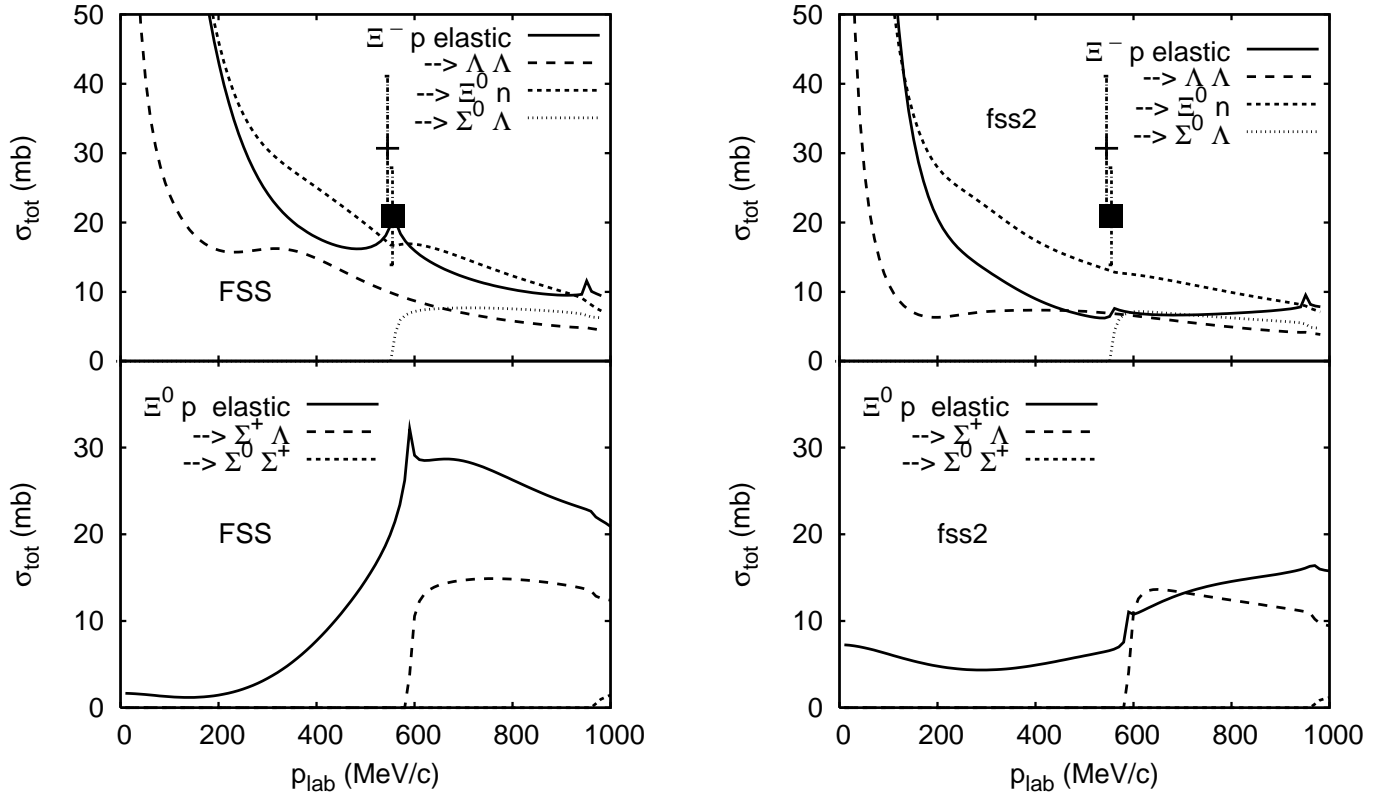


Figure 27: $\Xi^- p$ and $\Xi^0 p$ total cross sections predicted by FSS (left panels) and fss2 (right panels). The calculation is made in the particle basis, including the pion-Coulomb corrections.

The properties of the single-channel $\Sigma\Sigma$ interactions are extensively studied in Ref. [98]. The $\Sigma\Sigma(I = 0)$ interaction in the 1S_0 state is strongly attractive due to the color-magnetic interaction. The central force of the $\Sigma\Sigma(I = 1)$ interaction in the 3S_1 state is repulsive due to the Pauli effect. Since these $I = 0$ and 1 $\Sigma\Sigma$ configurations couple to other two-baryon continua, a direct experimental confirmation of these single-channel properties is not easy. On the other hand, the $I = 2$ $\Sigma\Sigma$ channel does not couple to any other two-baryon channels. Since the $\Sigma\Sigma(I = 2)$ 1S_0 state consists of the pure

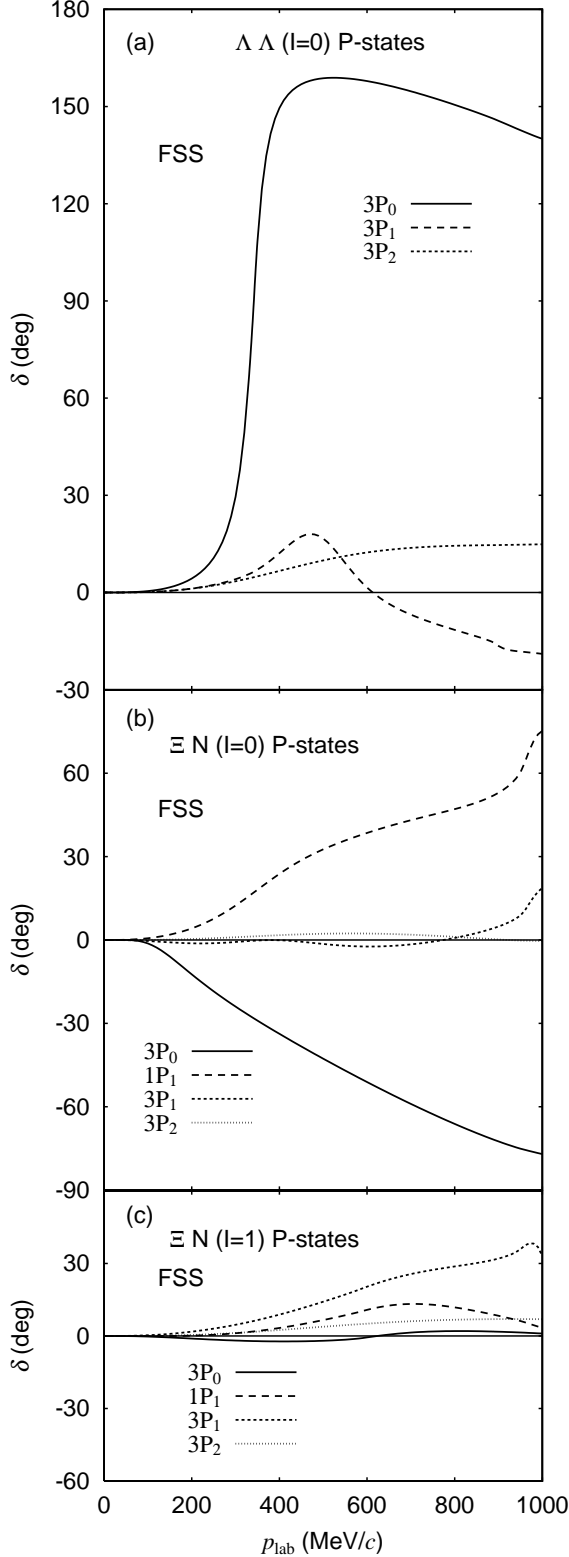


Figure 28: (left) The P -wave phase shifts of the (a) $\Lambda\Lambda(I = 0)$, (b) $\Xi N(I = 0)$ and (c) $\Xi N(I = 1)$ scatterings, predicted by FSS.

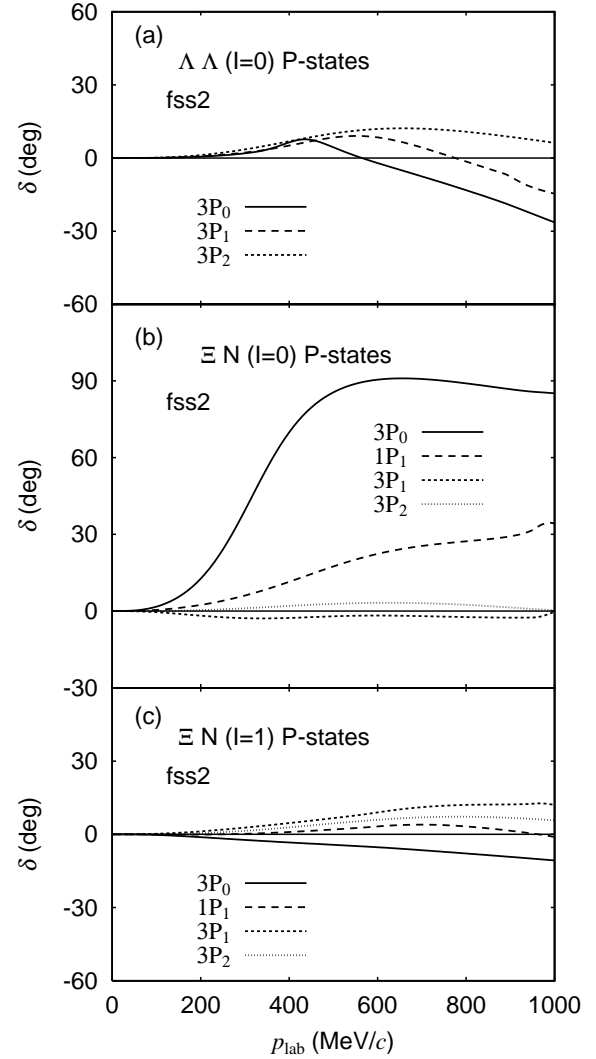


Figure 29: (above) The same as Fig. 28 but for fss2.

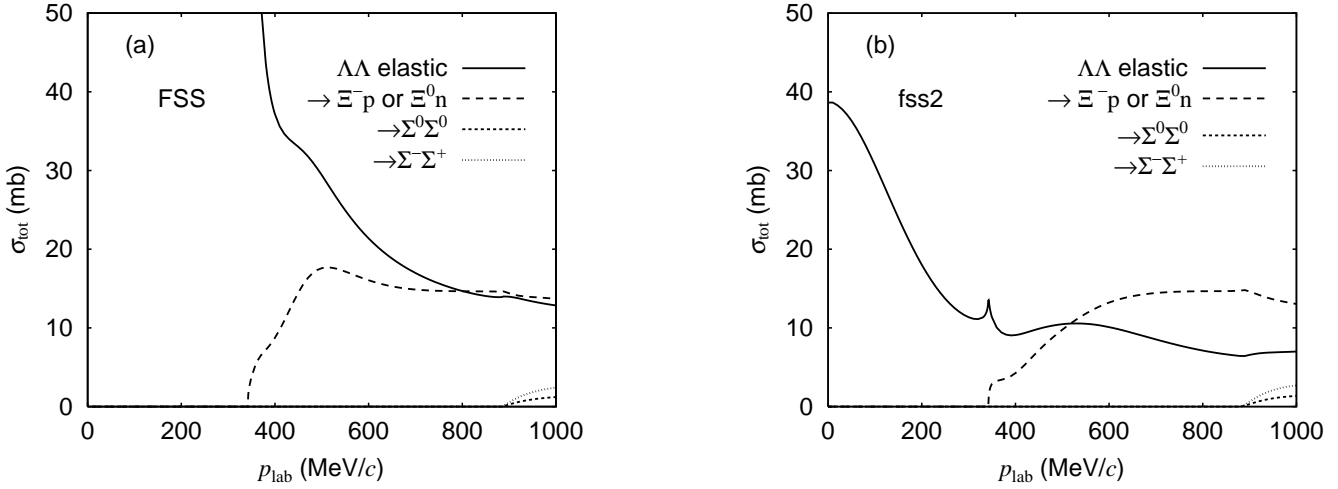


Figure 30: Total cross sections for the $\Lambda\Lambda$ scattering, predicted by FSS (a) and by fss2 (b).

(22) state, the behavior of this interaction is similar to that of the NN 1S_0 state. Figure 9(a) shows that this is indeed the case for fss2 and the 1S_0 phase shifts of the NN and $\Sigma\Sigma(I = 2)$ channels are very similar. Consequently, the $\Sigma^-\Sigma^-$ and pp total cross sections in Fig. 9(b) are almost equal.

3.3.2 $S = -3$ systems

[$\Xi\Lambda$ interaction]

As discussed in Sec. 3.2.1, the $\Xi\Lambda$ – $\Xi\Sigma$ interactions are most easily understood on the analogy of the ΛN – ΣN interactions. The replacement of N with Ξ induces the transition from the (03) to (30) SU_3 symmetry. This implies that the attractive feature of the spin-triplet deuteron channel is no longer taken over to the $\Xi\Lambda$ – $\Xi\Sigma(I = 1/2)$ CC system. Figures 31(a) and 31(b) illustrate this situation clearly for the 1S_0 and 3S_1 phase shifts predicted by fss2. For the flavor-symmetric 1S_0 state, the SU_3 contents of the $\Xi\Lambda$ – $\Xi\Sigma(I = 1/2)$ state are exactly the same as those of the ΛN – $\Sigma N(I = 1/2)$. Thus the $\Xi\Lambda$ and $\Xi\Sigma(I = 1/2)$ phase shifts are very similar to the ΛN and $\Sigma N(I = 1/2)$ phase shifts, respectively, with a slight decrease of the magnitude due to the FSB. On the other hand, the flavor-antisymmetric 3S_1 state of the $\Xi\Lambda$ and $\Xi\Sigma(I = 1/2)$ channels yields very similar repulsive phase shifts, related to the strong repulsion of the pure (30) $\Sigma N(I = 3/2)$ interaction. The fact that the magnitude of the repulsion is almost half of the latter is consistent with the weakly attractive nature of the SU_3 $(11)_a$ $\Xi N(I = 0)$ 3S_1 interaction (see Fig. 10(a)). The $\Xi\Lambda$ – $\Xi\Sigma$ channel coupling gives a very small cusp at the $\Xi\Sigma$ threshold both in the 1S_0 and 3S_1 states. It should be stressed that, in the 3S_1 state, the $\Xi\Lambda$ interaction does not resemble the ΛN interaction even qualitatively, since the ΛN 3S_1 state consists of the $(11)_a$ and (03) components, while the $\Xi\Lambda$ 3S_1 state consists of $(11)_a$ and (30) components.

It is reported through Faddeev calculations of light $\Xi\Lambda$ hypernuclei that ${}_{\Xi\Lambda}^6\text{He}$ makes the onset of nuclear stability for Ξ hyperons [154]. These authors, however, used an attractive $\Xi\Lambda$ effective force which simulates the strongly attractive $\Xi\Lambda$ interaction predicted by the Nijmegen soft-core NSC97 model [155, 143]. In view of the relationship between the $\Xi\Lambda$ and ΛN channels for 1S_0 and of the repulsive $\Xi\Lambda$ interaction for 3S_1 , it is very unlikely that fss2 predicts ${}_{\Xi\Lambda}^6\text{He}$ as a lightest particle-stable $S = -3$ hypernucleus.

[$\Xi\Sigma$ interaction]

As discussed above, the $\Xi\Sigma$ interactions with $I = 1/2$ are repulsive for both 1S_0 and 3S_1 states for the kinematical reason. The former is due to the $(11)_s$ Pauli-forbidden state and the latter due to the almost-forbidden (30) component. One cannot expect the strong $\Xi\Lambda$ – $\Xi\Sigma$ coupling by the one-pion exchange tensor force unlike the ΛN – ΣN channel coupling, since the SU_3 relation of the meson-baryon coupling yields $f_{\Xi\Xi\pi}/f_{NN\pi} = 2\alpha_m - 1 = -1/5$ for the magnetic-type pseudoscalar coupling with $\alpha_m = 2/5$ (the SU_6 relation). These features are clearly seen in the phase shifts drawn in Figs. 31(a) and 31(b).

On the other hand, the $\Xi\Sigma$ interactions with $I = 3/2$ are attractive for both 1S_0 and 3S_1 states. Table 5 shows that the 1S_0 state has the pure (22) symmetry, shared with the NN 1S_0 state, and the 3S_1 state has the (03) symmetry of the NN 3S_1 state. Of prime importance are the FSB and the fact that the $\Xi\Sigma$ system is composed of two non-identical particles. For the pion-exchange contributions, the SU_3 relations of the coupling constants are also important. The $\Xi\Sigma(I = 3/2)$ 1S_0 phase shift in Fig. 9(a) shows that the effect of the FSB is fairly large for fss2 and the phase-shift rise is about 40–50°. On the other hand, the similar magnitude of the attraction of the $\Xi\Sigma(I = 3/2)$ 3S_1 phase shift (Fig. 10(a)) is mainly related to the role of the exchange Feynman diagram, which is entirely different from the NN system. Unlike the (03) state in NN , the (03) state in $\Xi\Sigma(I = 3/2)$ is only moderately attractive, since the $\Xi\Sigma$ system does not allow the strong one-pion exchange in the exchange Feynman diagram. The reduction of the attraction in the direct Feynman diagram is also expected from the SU_3 relations for the $\Xi\Xi\pi$ coupling. In summary, the $\Xi\Sigma$ interaction predicted by the QM baryon-baryon interaction has a large isospin dependence like the ΣN interaction, namely, the repulsive behavior in the $I = 1/2$ state and the attractive behavior in the $I = 3/2$ state. In particular, fss2 predicts no bound state in the $\Xi^-\Sigma^-$ 1S_0 state.

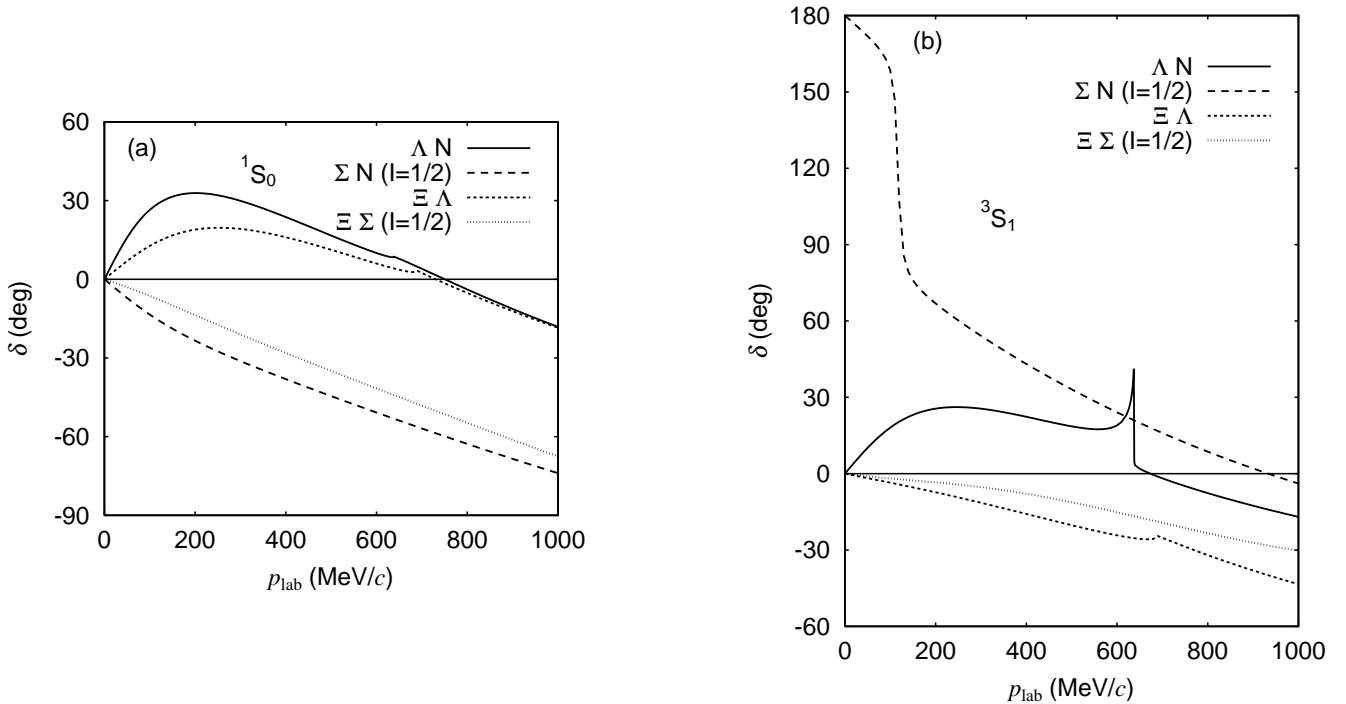


Figure 31: (a) 1S_0 phase shifts for the ΛN , $\Sigma N(I = 1/2)$, $\Xi\Lambda$, and $\Xi\Sigma(I = 1/2)$ interactions, predicted by fss2. (b) The same as (a) but for the 3S_1 state.

3.3.3 $S = -4$ systems

The SU_3 classification of the $\Xi\Xi$ system shows that the $I = 0$ system is represented by the pure (30) symmetry, while the $I = 1$ system by the pure (22) symmetry. We see in Figs. 10(a) and 9(a) that the $\Xi\Xi(I = 0)$ interaction is repulsive like the $\Sigma N(I = 3/2)$ one in the 3S_1 state and the $\Xi\Xi(I = 1)$ interaction is attractive like the $NN(I = 1)$ one in the 1S_0 state. In both cases, the effect of the FSB is appreciable. The prediction by fss2 gives no bound state in the $\Xi^0\Xi^0\ ^1S_0$ state. The $\Xi\Xi$ total cross sections are not so large as the NN ones, as seen in Fig. 9(b).

3.4 Triton and hypertriton Faddeev calculations

3.4.1 Three-nucleon bound state

Since our QM B_8B_8 interaction describes the short-range repulsion very differently from the meson-exchange potentials, it is interesting to examine the three-nucleon system predicted by fss2 and FSS. Here we solve the Faddeev equation for ^3H in the framework discussed in Sec. 2.4 directly using the QM RGM kernel in the isospin basis [156]. For the NN system, we have no Pauli-forbidden state. However, the energy dependence of the two-cluster RGM kernel should be treated properly through the self-consistency condition (2.68). Our Faddeev calculation is the full 50-channel calculation, including all the angular momentum up to $J = 6$ for the NN interaction, and the triton energy converges almost completely as seen in Table 10 [157]. The fss2 prediction, -8.52 MeV, seems to be overbound compared to the experimental value $E^{\text{exp}}(^3\text{H}) = -8.482$ MeV. In fact, this is not the case, since the present calculation is carried out using the np interaction. The charge dependence of the NN interaction indicates that the 1S_0 interaction of the nn system is less attractive than that of the np system. The effect of the charge dependence is estimated to be -0.19 MeV for the triton binding energy [85, 158]. If we take this into account, our result is still 0.15 MeV less bound.

For a realistic calculation of the ^3H binding energy, it is essential to use such an NN interaction that reproduces both the correct D -state probability P_D of the deuteron and the effective range parameters of the 1S_0 scattering [159]. Since all the realistic NN interactions reproduce the NN phase shifts more or less correctly, the strength of the central attraction is counterbalanced with that of the tensor force. Namely, if the interaction has a weaker tensor force, then it should have a stronger central attraction. Generally speaking, the effect of the tensor force is reduced in the nuclear many-body systems compared to the bare two-nucleon collision. Namely, the NN interaction with a weaker tensor force is favorable in order to obtain sufficient binding energies of the nuclear many-body systems. The weak tensor force, however, causes various problems such as a too small deuteron quadrupole moment Q_d and the disagreement of the mixing parameter ε_1 of the $^3S_1 + ^3D_1$ coupling.

The correlation between the triton binding energy, $B_t = -E(^3\text{H})$, and the D -state probability of the deuteron is plotted in Fig. 32 for fss2 and FSS as well as many other Faddeev calculations using modern realistic meson-exchange potentials. In the traditional meson-exchange potentials, the calculated points are located on a straight line, which is similar to the Coester line for the saturation point of symmetric nuclear matter. For example, the Reid soft-core potential (RSC) [160] gives $P_D = 6.5\%$ and predicts too small ^3H binding energy, $B_t = 7.35$ MeV. A series of the Bonn potentials reproduce the NN phase shifts very accurately, but they tend to have a rather weak tensor force [85]. The model C has the strongest tensor force, $P_D = 5.61\%$, yielding $B_t = 7.99$ MeV. The value P_D becomes smaller for models B and A, and the value of B_t becomes larger accordingly. The following results are given in Ref. [85]: model-B ($P_D = 5.0\%$, $B_t = 8.13$ MeV), model-A ($P_D = 4.4\%$, $B_t = 8.32$ MeV). These results are all obtained in the 34 channel calculations (including the NN total angular momentum $J \leq 4$), and by using the np interaction. In fact, the effects of the charge dependence and the charge asymmetry are important for the detailed discussion. The most recent Faddeev calculation employing the CD-Bonn potential [47] incorporates these effects, and predicts $B_t = 8.014$ MeV [162] for $P_D = 4.85\%$. The

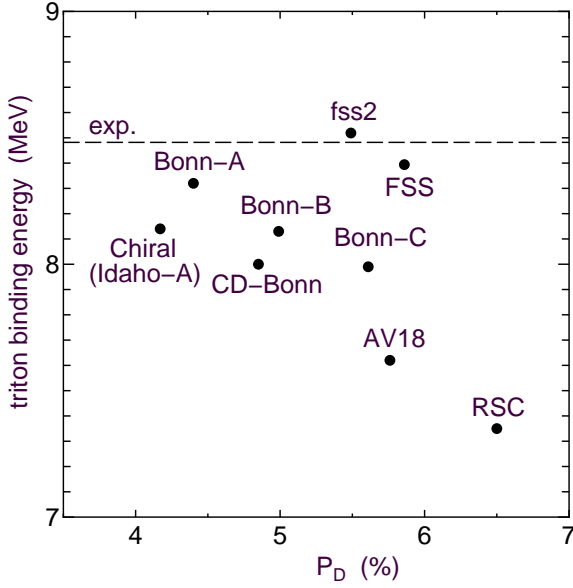


Figure 32: Calculated ${}^3\text{H}$ binding energies B_t as a function of the deuteron D -state probability P_D . All the calculations are made in the isospin basis, using the np interaction, except for the CD-Bonn potential. The calculated values are taken from [85] (RSC, Bonn-A, B, C), from [163] (AV18 [161], CD-Bonn [47]), and from [164] (Chiral). The experimental value, $B_t = 8.482$ MeV, is shown by the dashed line.

present status of the ${}^3\text{H}$ binding energy calculation is summarized as follows: more than 0.5 MeV is missing for any realistic two-nucleon interactions [163].

On the other hand, our result of the P_D value is 5.49 % for fss2 and 5.86 % for FSS. The deuteron quadrupole moment Q_d is 0.270 fm 2 for fss2 and 0.283 fm 2 for FSS. Our results of the effective range parameters listed in Tables 4 are not as perfect as those of the meson-exchange potentials, but the deuteron binding energy and the scattering length a_s for the 1S_0 state are fitted in determining our

Table 10: The three-nucleon bound state properties predicted by the Faddeev calculation with fss2 and FSS. The np interaction is used in the isospin basis. The heading “No. of channels” implies the number of two-nucleon channels included; n_{max} is the dimension of the diagonalization for the Faddeev equation; ε_{NN} the NN expectation value determined self-consistently; $E({}^3\text{H})$ the ground-state energy; and $\sqrt{\langle r^2 \rangle_{{}^3\text{H}}}$ ($\sqrt{\langle r^2 \rangle_{{}^3\text{He}}}$) the charge rms radius for ${}^3\text{H}$ (${}^3\text{He}$), including the proton and neutron size corrections through Eq. (3.6). The Coulomb force and the relativistic corrections are neglected.

model	No. of channels	n_{max}	ε_{NN} (MeV)	$E({}^3\text{H})$ (MeV)	$\sqrt{\langle r^2 \rangle_{{}^3\text{H}}}$ (fm)	$\sqrt{\langle r^2 \rangle_{{}^3\text{He}}}$ (fm)
fss2	2 (S)	2,100	2.361	-7.807	1.80	1.96
	5 (SD)	5,250	4.341	-8.189	1.75	1.92
	10 ($J \leq 1$)	10,500	4.249	-8.017	1.76	1.94
	18 ($J \leq 2$)	18,900	4.460	-8.439	1.72	1.90
	34 ($J \leq 4$)	35,700	4.488	-8.514	1.72	1.90
	50 ($J \leq 6$)	112,500	4.492	-8.519	1.72	1.90
FSS	2 (S)	2,100	2.038	-7.675	1.83	1.99
	5 (SD)	5,250	3.999	-8.034	1.78	1.95
	10 ($J \leq 1$)	10,500	3.934	-7.909	1.78	1.97
	18 ($J \leq 2$)	18,900	4.160	-8.342	1.74	1.93
	34 ($J \leq 4$)	35,700	4.175	-8.390	1.74	1.92
	50 ($J \leq 6$)	112,500	4.177	-8.394	1.74	1.92

QM parameters in the isospin basis. Under these circumstances, the results of fss2 and FSS in Fig. 32 seem to indicate that they form another $B_t - P_D$ line deviating from the traditional meson-exchange potentials. After the correction by the charge dependence of the NN interaction, our ${}^3\text{H}$ binding energies are smaller than the experimental value by merely 0.15 MeV for fss and 0.28 MeV for FSS. If we attribute these differences to the effect of the three-nucleon force, it is by far smaller than the generally accepted values, 0.5 - 1 MeV [163], obtained with the meson-theoretical NN interactions. A remarkable point of our results is that we can reproduce enough binding energy of the triton without reducing the deuteron D -state probability.

Table 10 lists the charge rms radii of ${}^3\text{H}$ and ${}^3\text{He}$, predicted by fss2 and FSS. The finite size corrections of the nucleons are made through

$$\begin{aligned}\langle r^2 \rangle_{3\text{H}} &= [R_C({}^3\text{H})]^2 + (0.8502)^2 - 2 \times (0.3563)^2, \\ \langle r^2 \rangle_{3\text{He}} &= [R_C({}^3\text{He})]^2 + (0.8502)^2 - \frac{1}{2} \times (0.3563)^2,\end{aligned}\quad (3.6)$$

where R_C^2 stands for the squared charge radius for the point nucleons which is obtained from the Faddeev calculations. Since our three-nucleon bound state wave functions are given in the momentum representation, we first calculate the charge form factors $F_C(Q^2)$, according to the formulation given in Ref. [165]. The values R_C^2 are then extracted from the power series expansion of $F_C(Q^2)$ with respect to Q^2 . In the present calculation, the Coulomb force and the relativistic correction terms [166] of the charge current operator are entirely neglected. The experimental values are difficult to determine, as discussed in Ref. [166]. Here we compare our results with two empirical values

$$\sqrt{\langle r^2 \rangle_{3\text{H}}} = \begin{cases} 1.70 \pm 0.05 \text{ fm} & [167] \\ 1.81 \pm 0.05 \text{ fm} & [168] \end{cases}, \quad \sqrt{\langle r^2 \rangle_{3\text{He}}} = \begin{cases} 1.87 \pm 0.05 \text{ fm} & [167] \\ 1.93 \pm 0.03 \text{ fm} & [168] \end{cases}. \quad (3.7)$$

The agreement with the experiment is satisfactory both for fss2 and FSS.

For the systems composed of three identical particles, the self-consistent energy of the two-cluster RGM kernel, ε_{NN} , has a clear physical meaning related to the decomposition of the total triton energy E into the kinetic-energy and potential-energy contributions. A simple manipulation of the Faddeev equations and the self-consistency condition yields

$$\langle H_0 \rangle = 2(3\varepsilon_\alpha - E), \quad \langle V \rangle = 3(E - 2\varepsilon_\alpha), \quad (3.8)$$

where the expectation value is calculated with respect to the three-nucleon total wave function. From the first equation, the ε_{NN} is obtained from the kinetic-energy contribution through $\varepsilon_{NN} = E/3 + \langle H_0 \rangle/6$. Table 11 lists this decomposition, together with the results of CD-Bonn [47] and AV18 [161] potentials [163]. We see that our QM results of ε_{NN} by FSS and fss2 are just in between these potentials, which

Table 11: Decomposition of the total triton energy E into the kinetic-energy and potential-energy contributions: $E = \langle H_0 \rangle + \langle V \rangle$. The unit is in MeV. In the present framework, this is given by the expectation value ε_{NN} of the two-cluster Hamiltonian with respect to the Faddeev solution, which is determined self-consistently. The results of CD-Bonn [47] and AV18 [161] are taken from Ref. [163].

model	ε_{NN}	E	$\langle H_0 \rangle$	$\langle V \rangle$
fss2	4.492	-8.519	43.99	-52.51
FSS	4.177	-8.394	41.85	-50.25
CD-Bonn	3.566	-8.012	37.42	-45.43
AV18	5.247	-7.623	46.73	-54.35

have very different strengths of the tensor force. The energy-dependence of the NN RGM kernel with the explicit structure $+\varepsilon K$ has some effects favorable to give a larger binding energy of the triton, since the value of the exchange normalization kernel K is $-1/9$ for the most compact ($0s$) wave function between the two nucleon-clusters. The RGM kernel becomes more attractive for a larger value of ε_{NN} . Table 11 indicates a larger $\langle V \rangle$ for a larger ε_{NN} , whereas the CD-Bonn and AV18 potentials do not have such an energy dependence.

The Faddeev calculations for ${}^3\text{H}$ using the QM NN potentials have also been carried out by Takeuchi, Cheon and Redish [169] and by the Salamanca-Jülich group [170]. In the former calculation, the model QCM-A gives the NN phase shifts with almost the same accuracy as our model FSS, and predicts $P_D = 5.58\%$ and $B_t = 8.01 - 8.02$ MeV in the 5-channel calculation. These are very similar to our FSS results. On the other hand, the Salamanca-Jülich group predicts $B_t = 7.72$ MeV, in spite of the small D -state probability $P_D = 4.85\%$. It is not clear to us how they treated the energy dependence of the RGM kernel when the separable expansion is introduced for solving the Faddeev equations. We think that the fit of the NN phase shifts for higher partial waves, especially for the P waves, has to be improved in order to extend their calculation to more than 5 channels.

3.4.2 The hypertriton

Next, we apply our QM NN and YN interactions to the hypertriton (${}^3_\Lambda\text{H}$) which has the small separation energy of the Λ -particle, $B_\Lambda^{\text{exp}} = 130 \pm 50$ keV [107]. Since the Λ -particle is far apart from the two-nucleon subsystem, the on-shell properties of the ΛN and ΣN interactions are expected to be well reflected in this system. In particular, this system is very useful to learn the relative strength of 1S_0 and 3S_1 attractions of the ΛN interaction, since the 1S_0 component plays a more important role than 3S_1 in this system and the available low-energy Λp total cross section data cannot discriminate many possible combinations of the 1S_0 and 3S_1 interactions. In fact, Refs. [171, 172, 173] showed that most

Table 12: Results of the hypertriton Faddeev calculations by fss2 and FSS. The heading E is the hypertriton energy measured from the ΛNN threshold, B_Λ the Λ separation energy, ε_{NN} ($\varepsilon_{\Lambda N}$) the NN (ΛN) expectation value determined self-consistently, and P_Σ the ΣNN probability in percent. The calculated deuteron binding energy is $\varepsilon_d = 2.2247$ MeV for fss2 and 2.2561 MeV for FSS ($\varepsilon_d^{\text{exp}} = 2.224644 \pm 0.000046$ MeV [86]). The norm of admixed redundant components is less than 10^{-9} .

model	No. of channels	E (MeV)	B_Λ (keV)	ε_{NN} (MeV)	$\varepsilon_{\Lambda N}$ (MeV)	P_Σ (%)
fss2	6 (S)	-2.362	137	-1.815	5.548	0.450
	15 (SD)	-2.423	198	-1.762	5.729	0.652
	30 ($J \leq 1$)	-2.403	178	-1.786	5.664	0.615
	54 ($J \leq 2$)	-2.498	273	-1.673	5.974	0.777
	102 ($J \leq 4$)	-2.513	288	-1.658	6.022	0.804
	150 ($J \leq 6$)	-2.514	289	-1.657	6.024	0.805
FSS	6 (S)	-2.910	653	-1.309	3.984	1.022
	15 (SD)	-2.967	710	-1.433	6.171	1.200
	30 ($J \leq 1$)	-2.947	691	-1.427	6.143	1.191
	54 ($J \leq 2$)	-3.121	865	-1.323	6.467	1.348
	102 ($J \leq 4$)	-3.134	877	-1.317	6.488	1.360
	150 ($J \leq 6$)	-3.134	878	-1.317	6.488	1.361

Table 13: Correlation between 1S_0 and 3S_1 effective range parameters of various ΛN interactions and the Λ separation energy B_Λ of the hypertriton. The B_Λ value for NSC89 is taken from Ref. [173]. The experimental B_Λ value is 130 ± 50 keV [126].

model	a_s (fm)	r_s (fm)	a_t (fm)	r_t (fm)	B_Λ (keV)
FSS [40]	-5.41	2.26	-1.02	4.20	878
fss2 [42, 43]	-2.59	2.83	-1.60	3.01	289
NSC89 [124]	-2.59	2.90	-1.38	3.17	143

meson-theoretical interactions fail to bind the hypertriton except for the Nijmegen soft-core potentials NSC89 [124], NSC97f and NSC97e [155]. It is also pointed out in Refs. [171] and [173] that a small admixture of the ΣNN components less than 1% is very important for this binding. We therefore carry out the ΛNN - ΣNN CC Faddeev calculation, by properly taking into account the existence of the SU_3 Pauli-forbidden state $(11)_s$ at the quark level. The necessary formulation is given in Sec. 2.4.

Table 12 shows the results of the Faddeev calculations using fss2 and FSS. In the 15-channel calculation including the S and D waves of the NN and YN interactions, we have already obtained $B_\Lambda = -\varepsilon_d - E(^3\text{H}) \approx 200$ keV for fss2. The convergence in the partial-wave expansion is very rapid, and the total angular-momentum $J \leq 4$ of the baryon pairs is enough to obtain 1 keV accuracy. With 150-channel ΛNN and ΣNN configurations we obtain $B_\Lambda = 289$ keV with the ΣNN component $P_\Sigma = 0.80\%$ for the fss2 prediction, and $B_\Lambda = 878$ keV with $P_\Sigma = 1.36\%$ for FSS.

Table 13 shows the correlation between the Λ separation energy B_Λ and the 1S_0 and 3S_1 ΛN effective range parameters of FSS, fss2 and NSC89. Although all of these ΛN interactions reproduce within the experimental error bars the low-energy ΛN total cross section data below about $p_\Lambda = 300$ MeV/ c , our QM interactions seem to be slightly more attractive than the NSC89 potential [124]. The model FSS gives a large overbinding since the 1S_0 ΛN interaction is strongly attractive. The phase-shift difference of the 1S_0 and 3S_1 states at about $p_\Lambda = 200$ MeV/ c is $\Delta\delta = \delta(^1S_0) - \delta(^3S_1) \approx 30^\circ$ for FSS, while $\Delta\delta \approx 10^\circ$ for fss2. Since the fss2 result is still slightly overbound, this difference should be made smaller in order to reproduce the experimental value. From the two results given by fss2 and FSS, we extrapolate the desired difference to be $0^\circ - 2^\circ$ in our QM. The same conclusion is also obtained in Ref. [174], using simulated interactions of the Nijmegen models.

In order to make sure that this extrapolation gives a good estimation, we modify the κ -meson mass of the model fss2 from the original value, $m_\kappa = 936$ MeV (see Table 2), to 1,000 MeV, and repeat the whole

Table 14: Decomposition of the NN and YN expectation values (ε_{NN} and ε_{YN}), the deuteron energy ($-\varepsilon_d$) and the total three-body energy E to the kinetic-energy and potential-energy contributions. The unit is in MeV. The results for NSC89 are taken from Ref. [171].

model	$h_{NN} + v_{NN} = \varepsilon_{NN}$	$h_d + v_d = -\varepsilon_d$ (deuteron)
FSS	19.986 - 21.303 = -1.317	16.982 - 19.238 = -2.256
fss2	19.371 - 21.029 = -1.657	17.495 - 19.720 = -2.225
NSC89	20.48 - 22.25 = -1.77	19.304 - 21.528 = -2.224
model	$h_{YN} + v_{YN} = \varepsilon_{YN}$	$\langle H \rangle + \langle V \rangle = E$
FSS	10.036 - 4.602 = 5.435	27.372 - 30.506 = -3.134
fss2	8.066 - 2.667 = 5.400	23.849 - 26.362 = -2.514
NSC89	7.44 - 3.54 = 3.90	23.45 - 25.79 = -2.34

calculation. This modification makes the 1S_0 ΛN interaction less attractive and the 3S_1 more attractive. We obtain $B_\Lambda = 145$ keV with $P_\Sigma = 0.53\%$, which is very close to the NSC89 prediction $B_\Lambda = 143$ keV with $P_\Sigma = 0.5\%$ [171, 173]. The effective range parameters of this modified fss2 interaction are $a_s = -2.15$ fm, $r_s = 3.05$ fm, and $a_t = -1.80$ fm, $r_t = 2.87$ fm. The phase-shift difference is only 1.3° and the increase of the total cross section of the ΛN scattering is at most 10 mb at $p_\Lambda = 100$ MeV/ c (from 286 mb to 296 mb), which is still within the experimental error bars. It should be kept in mind that the effective range parameters or the S -wave phase-shift values determined in this way is very much model dependent, since the B_Λ value is not determined by these quantities alone. It depends on how higher partial waves contribute and also on the details of the ΛN - ΣN coupling of a particular model. The reliability of the extrapolation shown here is based on the fact that the models fss2 and FSS have a common framework for the quark sector and EMEP's.

Table 12 also shows that the expectation value of the NN Hamiltonian, ε_{NN} , determined self-consistently is close to the deuteron energy $-\varepsilon_d$, especially in fss2. This feature is even more conspicuous if these energies are decomposed to the kinetic-energy and potential-energy contributions. Table 14 shows this decomposition with respect to fss2, FSS and NSC89. (For this comparison, we use the definition of the kinetic-energy part of the deuteron, given by $h_d = \langle \chi_d | h_{NN} | \chi_d \rangle / \langle \chi_d | \chi_d \rangle$, where χ_d is the RGM relative wave function between the neutron and the proton.) In fss2, the kinetic energy of the NN subsystem is 1.88 MeV larger than that of the deuteron, which suggests that the NN subsystem shrinks by the effect of the outer Λ -particle, in comparison with the deuteron in the free space. In NSC89, this difference is smaller, i.e., 1.18 MeV. These results are consistent with the fact that the hypertriton in NSC89 is more loosely bound ($B_\Lambda = 143$ keV) [173] than in fss2 (289 keV), and the Λ -particle is very far apart from the NN subsystem. Table 14 lists the kinetic-energy and potential-energy decompositions for the ΛN - ΣN averaged YN expectation value ε_{YN} and the total energy E . The kinetic energies of ε_{YN} are much smaller than those of ε_{NN} , which indicates that the relative wave function between the hyperon and the nucleon is widely spread in the configuration space. The comparison of the total-energy decomposition shows that the wave functions of fss2 and NSC89 may be very similar. A clear difference between them, however, appears in the roles of the higher partial waves. The energy increase due to the partial waves higher than the S and D waves is 91 keV in fss2 and 168 keV in FSS, respectively. On the other hand, the results in Refs. [171] and [173] indicate that this is only 20 - 30 keV in the case of NSC89. This difference originates from both of the NN and YN interactions. Since the characteristics of the meson-theoretical YN interactions in higher partial waves are *a priori* unknown, more detailed analysis of the fss2 results sheds light on the adequacy of the QM baryon-baryon interactions.

3.5 Application to $^9_\Lambda\text{Be}$ and $^6_{\Lambda\Lambda}\text{He}$ systems

3.5.1 The $\alpha\alpha\Lambda$ system for $^9_\Lambda\text{Be}$

As a typical example of three-cluster systems composed of two identical clusters, we apply the present formalism to the $\alpha\alpha\Lambda$ Faddeev calculation for $^9_\Lambda\text{Be}$, using the $\alpha\alpha$ RGM kernel and the $\Lambda\alpha$ folding potential generated from a simple ΛN effective interaction [135, 136]. For the $\alpha\alpha$ RGM kernel, we use the three-range Minnesota force [69] with the Majorana exchange mixture $u = 0.94687$, and the h.o. size parameter $\nu = 0.257$ fm $^{-2}$. The effective ΛN central interaction, denoted SB in Table 15, is a Minnesota-type potential

$$v_{\Lambda N} = \left[v(^1E) \frac{1 - P_\sigma}{2} + v(^3E) \frac{1 + P_\sigma}{2} \right] \left[\frac{u}{2} + \frac{2 - u}{2} P_r \right], \quad (3.9)$$

where $v(^1E)$ and $v(^3E)$ are simple two-range Gaussian potentials generated from the 1S_0 and 3S_1 phase shifts predicted by the QM ΛN interaction fss2. The inversion method based on supersymmetric

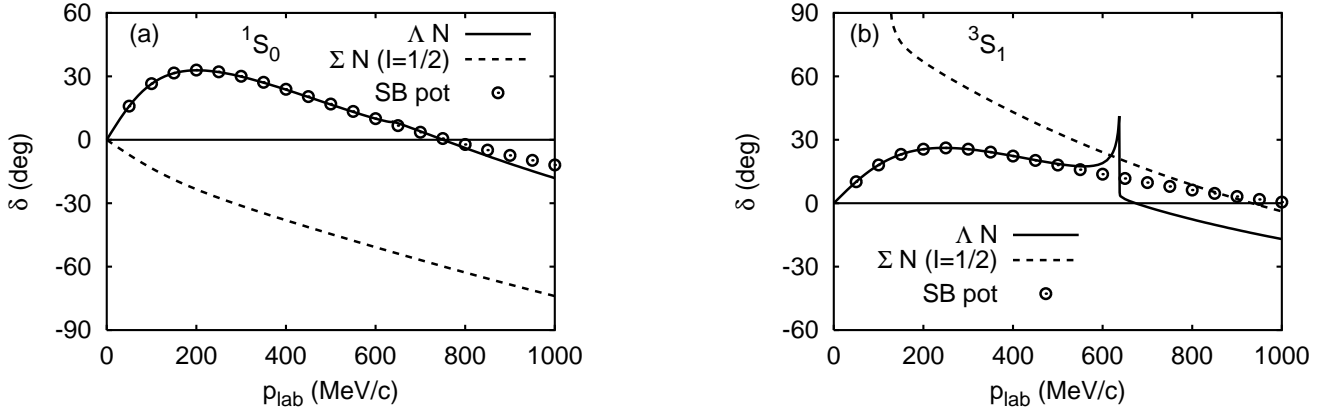


Figure 33: ΛN - ΣN 1S_0 (a) and 3S_1 (b) phase shifts for the isospin $I = 1/2$ channel, calculated with fss2 (solid and dashed curves) and the single-channel SB potentials ($f = 1$) in Eq. (3.10) (circles).

quantum mechanics is used to derive phase-shift equivalent local potentials [175]. These potentials are then fitted by two-range Gaussian functions:

$$\begin{aligned} v(^1S_0) &= -128.0 \exp(-0.8908 r^2) + 1015 \exp(-5.383 r^2) \quad (\text{MeV}), \\ v(^3S_1) &= -56.31 f \exp(-0.7517 r^2) + 1072 \exp(-13.74 r^2) \quad (\text{MeV}), \end{aligned} \quad (3.10)$$

where f is an adjustable parameter and r is the relative distance between Λ and N measured in fm. Figure 33 shows that these potentials fit the 1S_0 and 3S_1 ΛN phase shifts obtained by the full ΛN - ΣN CCRGM calculations of fss2. In the 3S_1 state, the phase shifts are fitted only in the low-momentum region with $p_{\text{lab}} < 600$ MeV/c, since the cusp structure is never reproduced in the single-channel calculation. Since any central and single-channel effective ΛN force leads to the well-known overbinding problem of $^5_\Lambda\text{He}$ by about 2 MeV (in the present case, it is 1.63 MeV) [111], the attractive part of the 3S_1 ΛN potential is modified to reproduce the correct binding energy, $E^{\text{exp}}(^5_\Lambda\text{He}) = -3.12 \pm 0.02$ MeV with $f = 0.8923$. This overbinding problem is mainly attributed to the Brueckner rearrangement effect of the α -cluster, originating from the starting energy dependence of the bare two-nucleon interaction due to the addition of an extra Λ -particle [176]. The odd-state ΛN interaction is introduced in Eq. (3.9) with the Majorana exchange parameter $u \neq 1$. All partial waves up to $\lambda_{\text{Max}} = \ell_{1\text{Max}} = 6$ for the $\alpha\alpha$ and $\Lambda\alpha$ pairs are included. The direct and exchange Coulomb kernel between the two α -clusters is introduced at the nucleon level with the cut-off radius, $R_C = 10$ fm. In the first calculation using only the central force, the SB potential with the pure Serber character ($u = 1$ in Eq. (3.9)) can reproduce the energies of the ground and excited states within 100 - 200 keV accuracy [135].

As already discussed in Sec. 3.2.7, one of the interesting problems in $^9_\Lambda\text{Be}$ is the very small spin-orbit (ℓs) splitting, $\Delta E_{\ell s} = E_x(3/2^+) - E_x(5/2^+)$, of the $5/2^+$ and $3/2^+$ excited states. The recent Hyperball γ -ray spectroscopy experiment predicts $\Delta E_{\ell s}^{\text{exp}} = 43 \pm 5$ keV [132, 133]. In the non-relativistic models of the YN interaction, this phenomenon is usually described by the strong cancellation of the ordinary LS component and the antisymmetric LS component ($LS^{(-)}$ force), the latter of which is a characteristic feature of baryon-baryon interactions between non-identical baryons. For example, our FSS interaction yields such a strong $LS^{(-)}$ component [29] that is about one half of the ordinary LS component with the opposite sign. We performed the G -matrix calculation in symmetric nuclear matter, using this QM interaction [45], and calculated the Scheerbaum factor S_B [46]. The ratio of S_B to the nucleon strength $S_N \approx -40$ MeVfm⁵ is $S_\Lambda/S_N \approx 1/5$ and $S_\Sigma/S_N \approx 1/2$ in the Born approximation, while it changes to $S_\Lambda/S_N \approx 1/12$ in the G -matrix calculation of the model FSS at the normal density $\rho_0 = 0.17$ fm⁻³. The significant reduction of S_Λ in the latter is due to the enhancement of the $LS^{(-)}$ component in the diagonal ΛN channel, owing to the P -wave ΛN - ΣN coupling.

Table 15: The ground-state energy $E_{\text{gr}}(1/2^+)$, the $5/2^+$ and $3/2^+$ excitation energies, $E_x(5/2^+)$ and $E_x(3/2^+)$, and the spin-orbit splitting, $\Delta E_{\ell s} = E_x(3/2^+) - E_x(5/2^+)$, calculated by solving the Faddeev equations for the $\alpha\alpha\Lambda$ system in the jj coupling scheme. The exchange mixture parameter of the SB ΛN force is assumed to be $u = 0.82$. The $\Lambda\alpha$ spin-orbit force is generated from the Born kernel of the FSS and fss2 ΛN LS interactions. For the fss2 LS interaction, the LS component from EMEP's is also included. The ΛN central potentials $v_{\Lambda N}^C$ used are Eqs. (3.9) and (3.10) (SB), the simulated Nijmegen models (NS, ND, NF) and Jülich model-A and B potentials (JA, JB) [177].

$v_{\Lambda N}^{LS}$	$v_{\Lambda N}^C$	$E_{\text{gr}}(1/2^+)$ (MeV)	$E_x(5/2^+)$ (MeV)	$E_x(3/2^+)$ (MeV)	$\Delta E_{\ell s}$ (keV)
FSS	SB	-6.623	2.854	2.991	137
	NS	-6.744	2.857	2.997	139
	ND	-7.485	2.872	3.024	152
	NF	-6.908	2.877	3.002	125
	JA	-6.678	2.866	2.991	124
	JB	-6.476	2.858	2.980	122
fss2	SB	-6.623	2.828	3.026	198
	NS	-6.745	2.831	3.033	202
	ND	-7.487	2.844	3.064	220
	NF	-6.908	2.853	3.035	182
	JA	-6.679	2.843	3.024	181
	JB	-6.477	2.834	3.012	178
Exp't [132, 133]		-6.62(4)	3.024(3)	3.067(3)	43(5)

In the $\alpha\alpha\Lambda$ three-cluster model, the origin of the ℓs splitting of the $5/2^+$ and $3/2^+$ excited states is only from the $\Lambda\alpha$ ℓs interaction. We therefore carry out the Faddeev calculation in the jj -coupling scheme, by using the central plus spin-orbit $\Lambda\alpha$ interactions [136]. The $\Lambda\alpha$ spin-orbit interaction is generated from the Born kernel of the ΛN LS QM interaction Eq. (2.31) by the α -cluster folding. The three possible LS types, LS , $LS^{(-)}$, and $LS^{(-)}\sigma$, in Eq. (2.32) are all included. The derivation of the $\Lambda\alpha$ Born kernel from the ΛN Born kernel can be carried out analytically, yielding the final form

$$V_{\Lambda\alpha}^{LS}(\mathbf{q}_f, \mathbf{q}_i) = \sum_{\mathcal{T}} [X_{\mathcal{T}}^d V_{\mathcal{T}}^{LSd}(\mathbf{q}_f, \mathbf{q}_i) + X_{\mathcal{T}}^e V_{\mathcal{T}}^{LSe}(\mathbf{q}_f, \mathbf{q}_i)] i\mathbf{n} \cdot \mathbf{S}_{\Lambda}. \quad (3.11)$$

Here $X_{\mathcal{T}}^{d,e}$ and $V_{\mathcal{T}}^{LSd,e}(\mathbf{q}_f, \mathbf{q}_i)$ are the spin-flavor factors and the spatial integrals, respectively, for the QM interaction types, $\mathcal{T} = D_-, D_+$ and S (S'), in the ΛN interaction. Since the QM ΛN interaction contains the strangeness exchange term, both the direct (d) and exchange (e) Feynman diagrams between Λ and the nucleon in the α -cluster contribute, and they are extremely non-local. The LS components from EMEP's are also included for the model fss2.

Table 15 shows the results of Faddeev calculations in the jj -coupling scheme, predicted by our QM ΛN LS interaction plus the SB and other various ΛN central potentials [177]. The ground-state energy does not change much from the LS -coupling calculation, indicating the dominant s -wave coupling of the Λ -hyperon. We can reproduce the ground-state energy using the SB central force with the Majorana exchange mixture $u = 0.82$. The final values for the ℓs splitting of the $5/2^+$ - $3/2^+$ excited states are $\Delta E_{\ell s} = 137$ keV (FSS) and 198 keV (fss2). Compared to the experimental value of 43 ± 5 keV, these predictions are three to five times too large. For the G -matrix simulated NSC97f LS potential in Ref. [134], we obtain 209 keV for the same SB force. The deviation from 0.16 MeV in Ref. [134] is

due to the model dependence of the $\alpha\alpha$ and $\Lambda\alpha$ interactions. Our FSS prediction for $\Delta E_{\ell s}$ is less than 2/3 of the NSC97f prediction, while fss2 gives almost the same result as NSC97f. If we switch off the EMEP contribution in the fss2 calculation, we find $\Delta E_{\ell s} = 86$ keV. This results from the dominant LS component (and the very small $LS^{(-)}$ component) generated from the EMEP of fss2.

We see that the direct use of the QM Born kernel for the ΛN LS component is not good enough to reproduce the small experimental value 43 ± 5 keV for the ℓs splitting. In order to clarify the origin of the problem, we have carried out an analysis of the $\Lambda\alpha$ s.p. spin-orbit potential, using the Scheerbaum factor, S_Λ [136]. Table 16 lists S_Λ in symmetric nuclear matter, obtained by the G -matrix calculations in the continuous prescription. The Fermi momentum, $k_F = 1.07 \text{ fm}^{-1}$, corresponding to the half of the normal density $\rho_0 = 0.17 \text{ fm}^{-3}$, is assumed. The table also shows the decompositions into various contributions and the results obtained by turning off the ΛN - ΣN coupling through the $LS^{(-)}$ and $LS^{(-)}\sigma$ forces. For FSS, we find a large reduction of S_Λ from the Born value -7.8 MeV fm^5 [46], especially when the P -wave ΛN - ΣN coupling is properly taken into account. When all the ΛN - ΣN couplings including those by the pion tensor force are turned off, the $LS^{(-)}$ contribution is just a half of the LS contribution with the opposite sign (in the dominant odd partial wave), which is the same result as in the Born approximation. The ${}^3P_2 + {}^3F_2$ ΛN - ΣN coupling slightly enhances the attractive LS contribution, while the ${}^1P_1 + {}^3F_1$ ΛN - ΣN coupling largely enhances the repulsive $LS^{(-)}$ contribution. If we use this reduction of the S_Λ factor from -7.8 MeV fm^5 to -1.9 MeV fm^5 in the realistic G -matrix calculation, the $\Delta E_{\ell s}$ value is reduced from -137 MeV to an almost correct value -33 keV . However, such a reduction of the Scheerbaum factor due to the ΛN - ΣN coupling is supposed to be hindered in the $\Lambda\alpha$ system in the lowest-order approximation from the isospin consideration. On the other hand, the situation of fss2 in Table 16 is rather different, although the cancellation mechanism between the LS and $LS^{(-)}$ components and the reduction effect of S_Λ factor in the full calculation are equally observed. When all the ΛN - ΣN couplings are neglected, the ratio of the $LS^{(-)}$ and LS contributions in the quark sector is still one half. Since the EMEP contribution is mainly for the LS type, it amounts to about -6 MeV fm^5 , which is very large and remains with the same magnitude even after the P -wave ΛN - ΣN coupling is included. Furthermore, the increase of the $LS^{(-)}$ component is rather moderate in comparison with the FSS case. This is because the model fss2 contains an appreciable EMEP contribution (about 40%) which has very little $LS^{(-)}$ contribution. As a result, the total S_Λ value in fss2 G -matrix calculation is 3 - 6 times larger than the FSS value, depending on the Fermi momentum $k_F = 1.35 - 1.07 \text{ fm}^{-1}$. Such an appreciable EMEP contribution to the LS component of the YN interaction is not favorable to reproduce the negligibly small ℓs splitting of ${}^9_\Lambda\text{Be}$.

Table 16: The Scheerbaum factor S_Λ in symmetric nuclear matter with $k_F = 1.07 \text{ fm}^{-1}$, predicted by G -matrix calculations of FSS and fss2 in the continuous prescription for intermediate spectra. Decompositions into various contributions are shown, together with the cases when the ΛN - ΣN coupling by the $LS^{(-)}$ and $LS^{(-)}\sigma$ forces is switched off (coupling off). The unit is in MeV fm^5 .

model		full		coupling off	
		odd	even	odd	even
FSS	LS	-17.36	0.38	-19.70	0.30
	$LS^{(-)}$	14.83	0.22	8.37	0.26
	total	-1.93		-10.77	
fss2	LS	-19.97	-0.14	-21.04	-0.20
	$LS^{(-)}$	8.64	0.21	6.12	0.23
	total	-11.26		-14.89	

In conclusion, the failure of the present Faddeev calculation is probably because the P -wave ΛN – ΣN coupling is not properly taken into account. The QM baryon-baryon interaction with a large spin-orbit contribution from the S-meson exchange potentials is not appropriate to reproduce the very small ℓs splitting observed in ${}^9_\Lambda\text{Be}$. A way of incorporating the P -wave ΛN – ΣN coupling in the cluster model calculations is a future problem.

3.5.2 The $\Lambda\Lambda\alpha$ system for ${}^6_\Lambda\text{He}$

As another application of the $\Lambda\alpha$ T -matrix in the $\alpha\alpha\Lambda$ Faddeev calculation, we discuss the ground-state energy of ${}^6_\Lambda\text{He}$ [178]. The full CC T -matrices of fss2 and FSS with strangeness $S = -2$ and isospin $I = 0$ are employed for the $\Lambda\Lambda$ RGM T -matrix (\tilde{T} -matrix). Table 17 shows the two- Λ separation energy $\Delta B_{\Lambda\Lambda}$ (defined by $\Delta B_{\Lambda\Lambda} = B_{\Lambda\Lambda}({}^6_\Lambda\text{He}) - 2B_\Lambda({}^5_\Lambda\text{He})$), predicted by various combinations of the ΛN and $\Lambda\Lambda$ interactions. The results of a simple three-range Gaussian potential, $v_{\Lambda\Lambda}$ (Hiyama), used in Ref. [177] are also shown. This $\Lambda\Lambda$ potential and our Faddeev calculation using the FSS \tilde{T} -matrix yield very similar results with large $\Delta B_{\Lambda\Lambda}$ values of about 3.6 MeV, in accordance with the fact that the $\Lambda\Lambda$ phases shifts predicted by these interactions increase up to about 40° (see Fig. 22). The improved QM fss2 yields $\Delta B_{\Lambda\Lambda} = 1.41$ MeV. (For the $\Lambda\Lambda$ single-channel T -matrix, this value is reduced to 1.14 MeV.) In Table 17, results are also shown for $v_{\Lambda\Lambda}(\text{SB})$ which is generated from the fss2 1S_0 $\Lambda\Lambda$ phase shift (see Fig. 23) in the full-channel calculation, using the supersymmetric inversion method [175]. This single-channel effective potential is given by

$$v_{\Lambda\Lambda}(\text{SB}) = -103.9 \exp(-1.176 r^2) + 658.2 \exp(-5.936 r^2) \quad (\text{MeV}). \quad (3.12)$$

We think that the 0.5 MeV difference between our fss2 result and the $v_{\Lambda\Lambda}(\text{SB})$ result is probably because we neglected the CC effects of the $\Lambda\Lambda\alpha$ channel to $\Xi N\alpha$ and $\Sigma\Sigma\alpha$ channels. We should also keep in mind that in all of these three-cluster calculations the Brueckner rearrangement effect of the α -cluster is very important, producing about -1 MeV (repulsive) contribution [142]. It is also reported in Ref. [179] that the quark Pauli effect between the α -cluster and the Λ -hyperon yields a non-negligible repulsive contribution of 0.1 - 0.2 MeV for the two- Λ separation energy of ${}^6_\Lambda\text{He}$, even when a rather compact ($3q$) size of $b = 0.6$ fm is assumed as in our QM interactions. Taking all of these effects into consideration, we can conclude that the present results by fss2 are in good agreement with the recent experimental value, $\Delta B_{\Lambda\Lambda}^{\text{exp}} = 1.01 \pm 0.20$ MeV, deduced from the NAGARA event [137].

Table 17: Comparison of $\Delta B_{\Lambda\Lambda}$ values in MeV, predicted by various $\Lambda\Lambda$ interactions and ΛN potentials. The $\Lambda\Lambda$ potential $v_{\Lambda\Lambda}$ (Hiyama) is the three-range Gaussian potential used in Ref. [177], and $v_{\Lambda\Lambda}(\text{SB})$ the two-range Gaussian potential given in Eq. (3.12). FSS and fss2 use the $\Lambda\Lambda$ RGM T -matrix (\tilde{T} -matrix) with $\varepsilon_{\Lambda\Lambda}$, which is the $\Lambda\Lambda$ expectation value determined self-consistently. The ΛN central potentials $v_{\Lambda N}^C$ used are Eqs. (3.9) and (3.10) (SB), the simulated Nijmegen models (NS, ND, NF) and Jülich model-A and B potentials (JA, JB) [177]. The experimental value is $\Delta B_{\Lambda\Lambda}^{\text{exp}} = 1.01 \pm 0.20$ MeV [137].

$v_{\Lambda\Lambda}$	Hiyama	FSS		fss2		SB
$v_{\Lambda N}^C$	$\Delta B_{\Lambda\Lambda}$	$\Delta B_{\Lambda\Lambda}$	$\varepsilon_{\Lambda\Lambda}$	$\Delta B_{\Lambda\Lambda}$	$\varepsilon_{\Lambda\Lambda}$	$\Delta B_{\Lambda\Lambda}$
SB	3.618	3.657	5.124	1.413	5.938	1.910
NS	3.548	3.630	5.151	1.366	5.947	1.914
ND	3.181	3.237	4.479	1.288	5.229	1.645
NF	3.208	3.305	4.622	1.271	5.407	1.713
JA	3.370	3.473	4.901	1.307	5.702	1.824
JB	3.486	3.599	5.141	1.327	5.952	1.911

4 Summary

Since the advent of the Yukawa's meson theory, an enormous amount of efforts have been devoted to understand the fundamental nucleon-nucleon (NN) interaction and related hadronic interactions. The present view of these interactions is a non-perturbative realization of inter-cluster interactions, governed by the fundamental theory of the strong interaction, quantum chromodynamics (QCD), in which the gluons are the field quanta exchanged between quarks. On this basis, the meson "theory" can be understood as an effective description of the quark-gluon dynamics in the low-energy regime. The short-range part of the NN and hyperon-nucleon (YN) interactions are still veiled with unsolved mechanism of quark confinement and multi-gluon effects.

In this review article, we applied a constituent quark model to the study of the baryon-baryon interactions, in which some of the essential features of QCD are explicitly taken into account in the non-relativistic framework. For example, the color degree of freedom of quarks is explicitly included, and the full antisymmetrization of quarks is carried out in the resonating-group method (RGM) formalism. The gluon exchange effect is represented in the form of the quark-quark interaction, for which a color analogue of the Fermi-Breit (FB) interaction is used with an adjustable parameter of the quark-gluon coupling constant α_S . The confinement potential is a phenomenological r^2 -type potential, which has no contributions to the baryon-baryon interactions in the present framework. Since the meson-exchange effects are the non-perturbative aspect of QCD, these are described by the effective-meson exchange potentials (EMEP's) acting between quarks.

Our purpose is to construct a realistic model of the NN and YN interactions, which describes not only the baryon-baryon scattering quantitatively in the wide energy region, but also reproduces rich phenomena observed in few-baryon systems and various types of finite nuclei and nuclear matter. The present framework incorporates both the quark and mesonic degrees of freedom into the model explicitly. This framework is very versatile, since it is based on the natural picture that the quarks and gluons are the most economical ingredients in the short-range region, while the meson-exchange processes dominate in the medium- and long-range regions of the interaction. The short-range repulsion is described by the color-magnetic term of the FB interaction and the Pauli effect at the quark level. In this article, we have focused on our recent versions called FSS [39, 40, 41] and fss2 [42, 43]. In FSS only the scalar-meson and pseudoscalar-meson exchanges are introduced as the EMEP's, while in fss2 the vector-meson exchanges are introduced as well. All possible standard terms used in the non-relativistic one-boson exchange potentials (OBEP) can in principle be included in the final version. As a first step to study the charge dependence of the baryon-baryon interactions, the pion-Coulomb correction is also taken into account in the particle basis. After these improvements mainly related to the EMEP's, the most recent model fss2 has achieved an accurate description of the NN and YN interactions.

An advantage of using the quark model for the study of the baryon-baryon interactions is that the flavor SU_3 symmetry (and also the spin-flavor SU_6 symmetry) is automatically incorporated in the framework, so that all the interactions between the octet-baryons (B_8) are treated in a unified manner in close connection with the well-known NN interaction. We extended the $(3q)$ -($3q$) RGM study of the NN and YN interactions to the strangeness $S = -2, -3$ and -4 sectors with no *ad hoc* parameters, and clarified the characteristic features of the $B_8 B_8$ interactions [43]. The results appear to be reasonable, if we consider i) the spin-flavor SU_6 symmetry of B_8 , ii) the weak pion effect in the strangeness sector, and iii) the effect of the flavor-symmetry breaking (FSB) of the underlying quark Hamiltonian. In particular, the existence of the Pauli-forbidden state in the SU_3 (11)_s channel (for the flavor-symmetric configuration) and the almost Pauli-forbidden state in the (30) channel (for the flavor-antisymmetric configuration) is of prime importance, in order to understand the origin of the Pauli repulsion and the relative strength among various baryon-baryon interactions. This is the most prominent feature of the spin-flavor SU_6 symmetry. The second feature, the weak pion effect in the strangeness sector, is a direct consequence of the SU_3 relationship in the model framework. The last

item is important even in the kinetic-energy term, since the heavier baryon masses reduce the kinetic energies appreciably. In fact, the light pion mass itself is a reflection of the chiral symmetry, which gives the most important source of the FSB.

These B_8B_8 interactions are now used for the detailed study of the few-body systems, as well as medium-weighted hypernuclei and baryonic matter through the G -matrix calculations. In particular, the G -matrix calculations are very useful to clarify the characteristics of the model interactions. Both fss2 and FSS are found to produce the nucleon single-particle (s.p.) potentials and nuclear-matter saturation curves, which are similar to those obtained with the standard meson-exchange potentials. For example, fss2 gives results very similar to the Bonn model-B potential. It is interesting to note that the deuteron properties calculated with fss2 are close to those of model-C, which has a larger D -state probability of the deuteron than model-B. Since fss2 reproduces the NN phase shifts at non-relativistic energies quite well, the difference of the off-shell effect between our quark model and the other OBEP models does not seem to appear prominently, as far as the nuclear saturation properties are concerned. Some interesting features of our quark model appear in the predictions for hyperon properties in nuclear medium. The Λ s.p. potential has a depth of 48 MeV (fss2) and 46 MeV (FSS) if the continuous prescription is used for intermediate energy spectra. This value is slightly more attractive than the value expected from the experimental data of Λ -hypernuclei [126]. However, the recent analysis of the Λ s.p. potentials in finite nuclei, using the local-density and Thomas-Fermi approximations, seems to suggest that this is an appropriate strength of attraction. The Σ s.p. potential is repulsive, with the strength of about 8 MeV (fss2) and 20 MeV (FSS). The origin of this repulsion is due to the strong Pauli effect of the (30) component in the $\Sigma N(I = 3/2) {}^3S_1$ state. This result is consistent with the recent analysis [127, 131] of the (K^-, π^\pm) and (π^-, K^+) experimental data [128, 129, 130]. Future experiments are expected to settle the problem of the Σ s.p. potential and the isospin dependence of the ΣN interaction. One of the characteristic features of fss2 is the LS force generated from the scalar-meson EMEP. If this contribution is large, the cancellation of the LS and $LS^{(-)}$ components from the FB interaction becomes less prominent. The model fss2 predicts the ratio of the Scheerbaum factors $S_\Lambda/S_N \approx 1/4$, which is larger than the FSS value $1/12$. Though these ratios are for symmetric nuclear matter with the normal density $\rho_0 = 0.17 \text{ fm}^{-3}$, the density dependence of S_Λ/S_N is actually weak in fss2.

We also discussed some applications of the NN , YN and YY interactions to the Faddeev calculations of the three-nucleon bound state, the ΛNN - ΣNN system for the hypertriton, the $\alpha\alpha\Lambda$ system for ${}^9_\Lambda\text{Be}$, and the $\Lambda\Lambda\alpha$ system for ${}^6_{\Lambda\Lambda}\text{He}$. For these applications, we developed a new three-cluster Faddeev formalism which uses two-cluster RGM kernels for the interacting pairs. The model fss2 gives the triton binding energy close enough to compare with the experiment. The charge root-mean-square radii of ${}^3\text{H}$ and ${}^3\text{He}$ are also correctly reproduced. The application to the hypertriton calculation shows that fss2 gives a result similar to the Nijmegen soft-core model NSC89, except for the appreciable contributions of higher partial waves. We find that the 1S_0 state of the ΛN interaction should be only slightly more attractive than the 3S_1 state, in order to reproduce the empirical hypertriton binding energy. A desirable difference of the 1S_0 and 3S_1 phase shifts around $p_\Lambda = 200 \text{ MeV}/c$ is only $0^\circ - 2^\circ$, although fss2 is still too attractive, giving about 10° . In the application to the $\alpha\alpha\Lambda$ system, the $\alpha\alpha$ RGM kernel and some appropriate ΛN forces generated from the low-energy phase-shift behavior of fss2 reproduce the ground-state and excitation energies of ${}^9_\Lambda\text{Be}$ within 100 - 200 keV accuracy. The very small spin-orbit splitting of the excited $5/2^+$ and $3/2^+$ states of ${}^9_\Lambda\text{Be}$ is studied in the Faddeev calculation in the jj -coupling scheme, where $\Lambda\alpha$ spin-orbit potential is generated from the ΛN Born kernel of the FSS and fss2 RGM kernels. It was argued that the P -wave ΛN - ΣN coupling by the $LS^{(-)}$ and $LS^{(-)}\sigma$ forces is very important to achieve the extremely small spin-orbit splitting as an almost complete cancellation between the LS and $LS^{(-)}$ contributions. The EMEP LS force generated from the scalar-meson exchange in fss2 reduces this cancellation. As deduced from the NAGARA event [137] for ${}^6_{\Lambda\Lambda}\text{He}$, the weak $\Lambda\Lambda$ force is reasonably well reproduced by the Faddeev calculation of the $\Lambda\Lambda\alpha$ system, using the present $\Lambda\alpha$ T -matrix and the

full CC $\Lambda\Lambda$ - ΞN - $\Sigma\Sigma$ \tilde{T} -matrix of fss2.

The interactions of the octet-baryons, derived from the quark model fss2 in the RGM formalism, enable us to reproduce a large number of NN and YN scattering observables. To further test these interactions, it is vital to apply them to the systems of more than two particles. The three-cluster formalism presented here will serve as a basic tool for this purpose and open a way to solve the few-body systems which interact via the quark-model baryon-baryon interactions, while keeping the essential features of the RGM kernels, i.e., the non-locality, the energy dependence and a possible existence of the pairwise Pauli-forbidden state. Since this formalism makes it possible to relate the underlying NN and YN interactions directly to the structure of the few-baryon systems, we expect to learn the interplay of the ingredients of the quark model, the baryon-baryon interactions, and the structure and binding mechanism of the nuclear systems.

Acknowledgments

This research is supported by Grants-in-Aid for Scientific Research from the Japanese Ministry of Education, Science, Sports and Culture (Nos. 04640296, 07640397, 08239203, 09225201, 12640265), Grants-in-Aid for Scientific Research (C) (Nos. 15540270, 15540284, 15540292 and 18540261) and for Young Scientists (B) (No. 15740161) from the Japan Society for the Promotion of Science (JSPS), and a Grant for Promotion of Niigata University Research Project (2005 - 2007). Some of the results presented in this article are based on the collaborations with T. Fujita (Japan Meteorological Agency), M. Kohno (Kyushu Dental College), and K. Miyagawa (Okayama Science University).

Appendix

Table 18: List of acronyms and abbreviations used in the text

Term	Meaning	Term	Meaning
B_8	octet-baryons	QM	quark model
NN	nucleon-nucleon	FB	Fermi-Breit
YN	hyperon-nucleon	FSB	flavor-symmetry breaking
YY	hyperon-hyperon	CIB	charge-independence breaking
B_8B_8	baryon-octet baryon-octet	CSB	charge-symmetry breaking
RGM	resonating-group method	LS-RGM	Lippmann-Schwinger RGM
GCM	generator-coordinate method	CC	coupled-channels
OCM	orthogonality condition model	\tilde{T} -matrix	RGM T -matrix in Eq. (2.58)
OPEP	one-pion exchange potential	LS	spin-orbit
OBEP	one-boson exchange potential	$LS^{(-)}$	antisymmetric LS
EMEP	effective-meson exchange potential	$LS^{(-)}\sigma$	antisymmetric LS with P_σ in Eq. (2.32)
s.p.	single-particle	QLS	quadratic LS in Eq. (2.33)
h.o.	harmonic-oscillator	ℓs	one-body LS

Table 18: -continued

Term	Meaning	Reference
RGM-F	quark model including effective-meson exchange potentials at the baryon level	[35, 36, 37]
FSS	quark model including scalar- and pseudoscalar-meson interactions	[39, 40, 41]
RGM-H	an alternative version of FSS	[40, 41]
fss2	quark-model including scalar-, pseudoscalar- and vector-meson interactions	[42, 43]
QMPACK	quark-model package homepage http://qmpack.homelinux.com/~qmpack/index.php	
SAID	Scattering Analysis Interactive Dial-up	
SP99	phase shift analysis in the SAID program	[61]
PWA93	phase shift analysis by the Nijmegen group	[62]
NSC**	Nijmegen soft-core potential	[124, 155, 143]
ESC**	Nijmegen extended soft-core potential	[25, 26]
CD-Bonn	charge-dependent Bonn	[47]
RSC	Reid soft-core potential	[160]
AV18	Argonne potential with 18 operators including CIB and CSB	[161]
SB	Sparenberg and Baye potential in Eqs. (3.10), (3.12)	[135, 178]

References

- [1] A. Valcarce, H. Garcilazo, F. Fernández and P. González, *Rep. Prog. Phys.* 68 (2005) 965
- [2] D. A. Liberman, *Phys. Rev. D* 16 (1977) 1542
- [3] A. De Rújula, H. Georgi and S.L. Glashow, *Phys. Rev. D* 12 (1975) 147
- [4] M. Oka and K. Yazaki, *Phys. Lett.* 90B (1980) 41 ; *Prog. Theor. Phys.* 66 (1981) 556, 572
- [5] M. Harvey, *Nucl. Phys. A* 352 (1981) 301, 326
- [6] Amand Faessler, F. Fernandez, G. Lübeck and K. Shimizu, *Phys. Lett. B* 112 (1982) 201
- [7] Y. Suzuki, *Nucl. Phys. A* 430 (1984) 539
- [8] See, for example, M. Oka and K. Yazaki, in *Quarks and Nuclei*, ed. W. Weise (World Scientific, Singapore, 1984), p.489
- [9] C.W. Wong, *Phys. Rep.* 136 (1986) 1
- [10] M. Oka, K. Shimizu and K. Yazaki, *Nucl. Phys. A* 464 (1987) 700
- [11] K. Shimizu, *Rep. Prog. Phys.* 52 (1989) 1
- [12] M. Oka and K. Yazaki, *Nucl. Phys. A* 402 (1983) 477
- [13] Y. Yamauchi and M. Wakamatsu, *Nucl. Phys. A* 457 (1986) 621
- [14] S. Takeuchi, K. Shimizu and K. Yazaki, *Nucl. Phys. A* 504 (1989) 777
- [15] K. Shimizu, *Phys. Lett.* 148B (1984) 418
- [16] U. Straub, Zhang Zong-Ye, K. Bräuer, Amand Faessler, S.B. Khadkikar and G. Lübeck, *Nucl. Phys. A* 483 (1988) 686 ; 508 (1990) 385c

- [17] K. Bräuer, Amand Faessler, F. Fernández and K. Shimizu, *Nucl. Phys. A* 507 (1990) 599
- [18] F. Fernández, A. Valcarce, U. Straub and A. Faessler, *J. Phys. G* 19 (1993) 2013
- [19] A. Valcarce, A. Buchmann, F. Fernández and Amand Faessler, *Phys. Rev. C* 50 (1994) 2246 ; 51 (1995) 1480
- [20] Zong-ye Zhang, Amand Faessler, U. Straub and L. Ya. Glozman, *Nucl. Phys. A* 578 (1994) 573
- [21] L. J. Qi, J. H. Zhang, P. N. Shen, Z. Y. Zhang and Y. W. Yu, *Nucl. Phys. A* 585 (1995) 693
- [22] Y. W. Yu, Z. Y. Zhang, P. N. Shen and L. R. Dai, *Phys. Rev. C* 52 (1995) 3393
- [23] P. N. Shen, Z. Y. Zhang, Y. W. Yu, X. Q. Yuan and S. Yang, *J. Phys. G* 25 (1999) 1807
- [24] J. Haidenbauer and Ulf-G. Meißner, *Phys. Rev. C* 72 (2005) 044005
- [25] Th. A. Rijken, *Phys. Rev. C* 73 (2006) 044007
- [26] Th. A. Rijken and Y. Yamamoto, *Phys. Rev. C* 73 (2006) 044008
- [27] Y. Fujiwara, *Prog. Theor. Phys.* 90 (1993) 105
- [28] Y. Suzuki and K. T. Hecht, *Nucl. Phys. A* 420 (1984) 525 ; 446 (1985) 749 (E)
- [29] C. Nakamoto, Y. Suzuki and Y. Fujiwara, *Phys. Lett. B* 318 (1993) 587
- [30] Y. Fujiwara and K. T. Hecht, *Nucl. Phys. A* 444 (1985) 541 ; 451 (1986) 625 ; 456 (1986) 669
- [31] Y. Fujiwara and K. T. Hecht, *Nucl. Phys. A* 462 (1987) 621
- [32] A. Faessler, G. Lübeck and K. Shimizu, *Phys. Rev. D* 26 (1981) 3280
- [33] M. Oka, *Phys. Rev. D* 31 (1985) 2274
- [34] J. Burger, R. Müller, K. Tregel and H. M. Hofmann, *Nucl. Phys. A* 493 (1989) 427
- [35] C. Nakamoto, Y. Suzuki and Y. Fujiwara, *Prog. Theor. Phys.* 94 (1995) 65
- [36] Y. Fujiwara, C. Nakamoto and Y. Suzuki, *Prog. Theor. Phys.* 94 (1995) 215
- [37] Y. Fujiwara, C. Nakamoto and Y. Suzuki, *Prog. Theor. Phys.* 94 (1995) 353
- [38] M. M. Nagels, T. A. Rijken and J. J. de Swart, *Phys. Rev. D* 20 (1979) 1633
- [39] Y. Fujiwara, C. Nakamoto and Y. Suzuki, *Phys. Rev. Lett.* 76 (1996) 2242
- [40] Y. Fujiwara, C. Nakamoto, and Y. Suzuki, *Phys. Rev. C* 54 (1996) 2180
- [41] T. Fujita, Y. Fujiwara, C. Nakamoto and Y. Suzuki, *Prog. Theor. Phys.* 100 (1998) 931
- [42] Y. Fujiwara, T. Fujita, M. Kohno, C. Nakamoto and Y. Suzuki, *Phys. Rev. C* 65 (2002) 014002
- [43] Y. Fujiwara, M. Kohno, C. Nakamoto and Y. Suzuki, *Phys. Rev. C* 64 (2001) 054001
- [44] Y. Fujiwara, M. Kohno, C. Nakamoto and Y. Suzuki, *Prog. Theor. Phys.* 103 (2000) 755
- [45] M. Kohno, Y. Fujiwara, T. Fujita, C. Nakamoto and Y. Suzuki, *Nucl. Phys. A* 674 (2000) 229
- [46] Y. Fujiwara, M. Kohno, T. Fujita, C. Nakamoto and Y. Suzuki, *Nucl. Phys. A* 674 (2000) 493
- [47] R. Machleidt, *Phys. Rev. C* 63 (2001) 024001
- [48] M. M. Nagels, T. A. Rijken and J. J. de Swart, *Ann. Phys. (N.Y.)* 79 (1973) 338
- [49] Y. Fujiwara, *Prog. Theor. Phys. Suppl.* No. 91 (1987) 160
- [50] M. Kamimura, *Prog. Theor. Phys. Suppl.* No. 62 (1977) 236
- [51] K. Kume and S. Yamaguchi, *Phys. Rev. C* 48 (1993) 2097
- [52] D. R. Entem, F. Fernández and A. Valcarce, *Phys. Rev. C* 62 (2000) 034002
- [53] H. P. Noyes, *Phys. Rev. Lett.* 15 (1965) 538
- [54] K. L. Kowalski, *Phys. Rev. Lett.* 15 (1965) 798, 908 (E)
- [55] Y. Fujiwara, M. Kohno, C. Nakamoto and Y. Suzuki, *Prog. Theor. Phys.* 104 (2000) 1025

- [56] Y. Fujiwara and Y. C. Tang, *Memoirs of the Faculty of Science, Kyoto University, Series A of Physics, Astrophysics, Geophysics and Chemistry* Vol. XXXIX, No. 1, Article 5 (1994) 91
- [57] Y. Suzuki, *Nucl. Phys. A* 405 (1983) 40
- [58] Y. Fujiwara, *Prog. Theor. Phys.* 88 (1992) 933
- [59] Y. Fujiwara, C. Nakamoto, Y. Suzuki and Zhang Zong-ye, *Prog. Theor. Phys.* 97 (1997) 587 : The S -type $LS^{(-)}\sigma$ factor in Eq. (C.4) of this paper should be read as $X_S^{LS^{(-)\sigma}} = -\frac{1}{108} (1 - \frac{1}{\lambda}) [\frac{5}{3} (1 + \frac{1}{\lambda}) + (1 - \frac{1}{\lambda}) P_F]$ for $B_3B_1 = \Sigma\Lambda$. Accordingly, the second expression in Eq. (5.17) is changed to $(X_{S'}^{LS^{(-)\sigma}})_{\Lambda\Sigma} = \frac{1}{108} (1 - \frac{1}{\lambda}) [\frac{5}{3} (1 + \frac{1}{\lambda}) - (1 - \frac{1}{\lambda}) P_F]$.
- [60] K. Yazaki, *Prog. Part. Nucl. Phys.* 24 (1990) 353
- [61] Scattering Analysis Interactive Dial-up (SAID), Virginia Polytechnic Institute, Blacksburg, Virginia, R. A. Arndt: Private Communication
- [62] V. G. J. Stoks, R. A. M. Klomp, C. P. F. Terheggen and J. J. de Swart, *Phys. Rev. C* 49 (1994) 2950
- [63] R. R. Scheerbaum, *Nucl. Phys. A* 257 (1976) 77
- [64] C. M. Vincent and S. C. Phatak, *Phys. Rev. C* 10 (1974) 391
- [65] Y. Fujiwara, in *Proceedings of the Third Asia-Pacific Conference on Few-Body Problems in Physics* (APFB05), Nakhon Ratchasima, Thailand, July 26 - 30, 2005.
- [66] H. Horiuchi, *Prog. Theor. Phys.* 51 (1974) 1266 ; 53 (1975) 447
- [67] Y. Fujiwara, H. Nemura, Y. Suzuki, K. Miyagawa and M. Kohno, *Prog. Theor. Phys.* 107 (2002) 745
- [68] Y. Fujiwara, Y. Suzuki, K. Miyagawa, M. Kohno and H. Nemura, *Prog. Theor. Phys.* 107 (2002) 993
- [69] D. R. Thompson, M. LeMere and Y. C. Tang, *Nucl. Phys. A* 286 (1977) 53
- [70] Y. Fujiwara, K. Miyagawa, M. Kohno, Y. Suzuki, D. Baye and J.-M. Sparenberg, *Phys. Rev. C* 70 (2004) 024002
- [71] Y. Fujiwara, K. Miyagawa, M. Kohno, Y. Suzuki, D. Baye and J.-M. Sparenberg, *Nucl. Phys. A* 738 (2004) 495
- [72] S. Oryu, K. Samata, T. Suzuki, S. Nakamura and H. Kamada, *Few-Body Systems* 17 (1994) 185
- [73] Y. Fujiwara, M. Kohno and Y. Suzuki, *Few-Body Systems* 34 (2004) 237
- [74] V. I. Kukulin and V. N. Pomerantsev, *Ann. Phys. (N.Y.)* 111 (1978) 330
- [75] B. Buck, H. Friedrich and C. Wheatley, *Nucl. Phys. A* 275 (1977) 246
- [76] Y. Fujiwara, Y. Suzuki and M. Kohno, *Phys. Rev. C* 69 (2004) 037002
- [77] E. M. Tursunov, *J. Phys. G* 27 (2001) 1381
- [78] E. M. Tursunov, D. Baye and P. Descouvemont, *Nucl. Phys. A* 723 (2003) 365
- [79] P. Descouvemont, C. Daniel and D. Baye, *Phys. Rev. C* 67 (2003) 044309
- [80] R. A. Bryan and B. L. Scott, *Phys. Rev.* 164 (1967) 1215
- [81] <http://qmpack.homelinux.com/~qmpack/index.php>
- [82] V. G. J. Stoks, R. A. M. Klomp, M. C. M. Rentmeester and J. J. de Swart, *Phys. Rev. C* 48 (1993) 792
- [83] A. Valcarce, Amand Faessler and F. Fernández, *Phys. Lett. B* 345 (1995) 367
- [84] M. Lacombe, B. Loiseau, J. M. Richard, R. Vinh Mau, J. Côté, P. Pirès and R. de Tournell, *Phys. Rev. C* 21 (1980) 861

- [85] R. Machleidt, *Adv. Nucl. Phys.* 19 (1989) 189
- [86] O. Dumbrajs, R. Koch, H. Pilkuhn, G. C. Oades, H. Behrens, J. J. de Swart and P. Kroll, *Nucl. Phys. B* 216 (1983) 277
- [87] L. J. Allen, H. Fiedeldey and N. J. McGurk, *J. Phys. G* 4 (1978) 353
- [88] M. Kohno, *J. Phys. G* 9 (1983) L85
- [89] N. L. Rodning and L. D. Knutson, *Phys. Rev. C* 41 (1990) 898
- [90] David M. Bishop and Lap M. Cheung, *Phys. Rev. A* 20 (1979) 381
- [91] G. A. Miller, B. M. K. Nefkens and I. Šlaus, *Phys. Rep.* 194 (1990) 1
- [92] C. R. Howell *et al.*, *Phys. Lett. B* 444 (1998) 252
- [93] D. E. González Trotter *et al.*, *Phys. Rev. Lett.* 83 (1999) 3788
- [94] J. R. Bergervoet, P. C. van Campen, W. A. van der Sanden and J. J. de Swart, *Phys. Rev. C* 38 (1988) 15
- [95] G. T. Stephenson, Jr., Kim Maltman and T. Goldman, *Phys. Rev. D* 43 (1991) 860
- [96] M. M. Nagels, T. A. Rijken and J. J. de Swart, *Phys. Rev. D* 12 (1975) 744
- [97] Y. Suzuki and K. T. Hecht, *Phys. Rev. C* 27 (1983) 299
- [98] C. Nakamoto, Y. Suzuki and Y. Fujiwara, *Prog. Theor. Phys.* 97 (1997) 761
- [99] T. Fujita, Y. Fujiwara, C. Nakamoto and Y. Suzuki, *Prog. Theor. Phys.* 96 (1996) 653
- [100] T. Kadowaki *et al.*, *Eur. Phys. J. A* 15 (2002) 295
- [101] M. Kurosawa, KEK-Report 2005-104
- [102] K. Miyagawa and H. Yamamura, *Phys. Rev. C* 60 (1999) 024003
- [103] S. Shinmura, Y. Akaishi and H. Tanaka, *Prog. Theor. Phys.* 71 (1984) 546
- [104] Y. Yamamoto, T. Motoba, H. Himeno, K. Ikeda and S. Nagata, *Prog. Theor. Phys. Suppl. No.* 117 (1994) 361
- [105] E. Hiyama, *Nucl. Phys. A* 670 (2000) 273c
- [106] H. Nemura, Y. Suzuki, Y. Fujiwara and C. Nakamoto, *Prog. Theor. Phys.* 103 (2000) 929
- [107] Y. Fujiwara, K. Miyagawa, M. Kohno and Y. Suzuki, *Phys. Rev. C* 70 (2004) 024001
- [108] G. Alexander, U. Karshon, A. Shapira, G. Yekutieli, R. Engelmann, H. Filthuth and W. Lughofer, *Phys. Rev.* 173 (1968) 1452
- [109] B. Sechi-Zorn, B. Kehoe, J. Twitty and R. A. Burnstein, *Phys. Rev.* 175 (1968) 1735
- [110] J. A. Kadyk, G. Alexander, J. H. Chan, P. Gaposchkin and G. H. Trilling, *Nucl. Phys. B* 27 (1971) 13
- [111] R. H. Dalitz, R. C. Herndon and Y. C. Tang, *Nucl. Phys. B* 47 (1972) 109
- [112] D. J. Millener, *Nucl. Phys. A* 691 (2001) 93c
- [113] Y. Fujiwara, T. Fujita, C. Nakamoto and Y. Suzuki, *Prog. Theor. Phys.* 100 (1998) 957
- [114] J. J. de Swart and C. Dullemond, *Ann. Phys. (N.Y.)* 19 (1962) 458
- [115] R. R. Ross, *Bull. Ann. Phys. Sic.* 3 (1958) 335
- [116] V. Hepp and H. Schleich, *Z. Phys.* 214 (1968) 71
- [117] D. Stephen, Ph. D. thesis, Univ. of Massachusetts, 1970 (unpublished)
- [118] R. Engelmann, H. Filthuth, V. Hepp and E. Kluge, *Phys. Lett.* 21 (1966) 587
- [119] F. Eisele, H. Filthuth, W. Föhlich, V. Hepp and G. Zech, *Phys. Lett.* 37B (1971) 204
- [120] J. K. Ahn *et al.*, *Nucl. Phys. A* 648 (1999) 263
- [121] J. K. Ahn *et al.*, *Nucl. Phys. A* 761 (2005) 41

- [122] Y. Kondo *et al.*, *Nucl. Phys. A* 676 (2000) 371
- [123] R. Brockmann and R. Machleidt, *Phys. Rev. C* 42 (1990) 1965
- [124] P. M. M. Maessen, Th. A. Rijken and J. J. de Swart, *Phys. Rev. C* 40 (1989) 2226
- [125] H.-J. Schulze, M. Baldo, U. Lombardo, J. Cugnon and A. Lejeune, *Phys. Rev. C* 57 (1998) 704
- [126] H. Bando, T. Motoba and J. Žofka, *Int. J. of Mod. Phys. A* 5 (1990) 4021
- [127] J. Dąbrowski, *Phys. Rev. C* 60 (1999) 025205
- [128] R. Sawafta, *Nucl. Phys. A* 585 (1995) 103c ; 639 (1998) 103c
- [129] H. Noumi *et al.*, *Phys. Rev. Lett.* 89 (2002) 072301 ; 90 (2003) 049902 (E)
- [130] P. K. Saha *et al.*, *Phys. Rev. C* 70 (2004) 044613
- [131] M. Kohno, Y. Fujiwara, Y. Watanabe, K. Ogata and M. Kawai, *Prog. Theor. Phys.* 112 (2004) 895 ; to appear in *Phys. Rev. C* (2006)
- [132] H. Akikawa *et al.*, *Phys. Rev. Lett.* 88 (2002) 082501
- [133] H. Tamura *et al.*, *Nucl. Phys. A* 754 (2005) 58c
- [134] E. Hiyama, M. Kamimura, T. Motoba, T. Yamada and Y. Yamamoto, *Phys. Rev. Lett.* 85 (2000) 270
- [135] Y. Fujiwara, K. Miyagawa, M. Kohno, Y. Suzuki, D. Baye and J.-M. Sparenberg, *Phys. Rev. C* 70 (2004) 024002
- [136] Y. Fujiwara, M. Kohno, K. Miyagawa and Y. Suzuki, *Phys. Rev. C* 70 (2004) 047002
- [137] H. Takahashi *et al.*, *Phys. Rev. Lett.* 87 (2001) 212502
- [138] D. J. Prowse, *Phys. Rev. Lett.* 17 (1966) 782
- [139] M. Danysz *et al.*, *Phys. Rev. Lett.* 11 (1963) 29
- [140] S. Aoki *et al.*, *Prog. Theor. Phys.* 85 (1991) 1287
- [141] I. N. Filikhin, A. Gal and V. M. Suslov, *Nucl. Phys. A* 743 (2004) 194
- [142] M. Kohno, Y. Fujiwara and Y. Akaishi, *Phys. Rev. C* 68 (2003) 034302
- [143] V. G. J. Stoks and Th. A. Rijken, *Phys. Rev. C* 59 (1999) 3009
- [144] M. Oka, K. Shimizu and K. Yazaki, *Phys. Lett.* 130B (1983) 365
- [145] C. Nakamoto, Y. Fujiwara and Y. Suzuki, *Nucl. Phys. A* 670 (2000) 315c
- [146] C. Nakamoto, Y. Fujiwara and Y. Suzuki, *Nucl. Phys. A* 639 (1998) 51c
- [147] U. Straub, Zong-Ye Zhang, K. Bräuer, Amand Faessler and S. B. Khadkikar, *Phys. Lett. B* 200 (1988) 241
- [148] Y. Koike, K. Shimizu and K. Yazaki, *Nucl. Phys. A* 513 (1990) 653
- [149] T. Fernández-Caramés, A. Valcarce and P. González, *Phys. Rev. D* 72 (2005) 054008
- [150] C. Nakamoto, Y. Fujiwara and Y. Suzuki, *Nucl. Phys. A* 691 (2001) 238c
- [151] T. Tamagawa *et al.*, *Nucl. Phys. A* 691 (2001) 234c
- [152] Y. Yamamoto, T. Tamagawa, T. Fukuda and T. Motoba, *Prog. Theor. Phys.* 106 (2001) 363
- [153] J. K. Ahn *et al.*, *Phys. Lett. B* 633 (2006) 214
- [154] I. N. Filikhin and A. Gal, *Nucl. Phys. A* 707 (2002) 491 ; *Phys. Rev. C* 65 (2002) 041001
- [155] Th. A. Rijken, V. G. J. Stoks and Y. Yamamoto, *Phys. Rev. C* 59 (1999) 21
- [156] Y. Fujiwara, K. Miyagawa, M. Kohno, Y. Suzuki and H. Nemura, *Phys. Rev. C* 66 (2002) 021001
- [157] Y. Fujiwara, K. Miyagawa, Y. Suzuki, M. Kohno and H. Nemura, *Nucl. Phys. A* 721 (2003) 983c
- [158] R. A. Brandenburg, G. S. Chulick, Y. E. Kim, D. J. Klepacki, R. Machleidt, A. Picklesimer and R. M. Thaler, *Phys. Rev. C* 37 (1988) 781

- [159] R. A. Brandenburg, G. S. Chulick, R. Machleidt, A. Picklesimer and R. M. Thaler, *Phys. Rev. C* 37 (1988) 1245
- [160] R. V. Reid, *Ann. Phys. (N.Y.)* 50 (1968) 411
- [161] R. B. Wiringa, V. G. J. Stoks and R. Schiavilla, *Phys. Rev. C* 51 (1995) 38
- [162] A. Nogga, D. Hüber, H. Kamada and W. Glöckle, *Phys. Lett. B* 409 (1997) 19
- [163] A. Nogga, H. Kamada and W. Glöckle, *Phys. Rev. Lett.* 85 (2000) 944
- [164] D. R. Entem and R. Machleit, *Phys. Lett. B* 524 (2002) 93
- [165] W. Glöckle, *Nucl. Phys. A* 381 (1982) 343
- [166] Kr. T. Kim, Y. E. Kim, D. J. Klepacki, Richard A. Brandenburg, E. P. Harper and R. Machleidt, *Phys. Rev. C* 38 (1988) 2366
- [167] H. Collard, R. Hofstadter, E. B. Hughes, A. Johansson, M. R. Yearian, R. B. Day and R. T. Wagner, *Phys. Rev.* 138 (1965) B57
- [168] J. Martino, in *The Three-Body Force in the Three-Nucleon System*, Vol. 260 of *Lecture Note in Physics*, edited by B. L. Berman and B. F. Gibson (Springer-Verlag, Berlin, 1986), p. 129
- [169] S. Takeuchi, T. Cheon and E. F. Redish, *Phys. Lett. B* 280 (1992) 175 ; *Nucl. Phys. A* 508 (1990) 247c
- [170] B. Juliá-Díaz, J. Haidenbauer, A. Valcarce and F. Fernández, *Phys. Rev. C* 65 (2002) 034001
- [171] K. Miyagawa, H. Kamada, W. Glöckle and V. Stoks, *Phys. Rev. C* 51 (1995) 2905
- [172] K. Miyagawa, H. Kamada, W. Glöckle, H. Yamamura, T. Mart and C. Bennhold, *Few-Body Systems Suppl.* 12 (2000) 324
- [173] A. Nogga, H. Kamada and W. Glöckle, *Phys. Rev. Lett.* 88 (2002) 172501
- [174] H. Nemura, Y. Akaishi and Y. Suzuki, *Phys. Rev. Lett.* 89 (2002) 142504
- [175] J.-M. Sparenberg and D. Baye, *Phys. Rev. C* 55 (1997) 2175
- [176] H. Bando and I. Shimodaya, *Prog. Theor. Phys.* 63 (1980) 1812
- [177] E. Hiyama, M. Kamimura, T. Motoba, T. Yamada and Y. Yamamoto, *Prog. Theor. Phys.* 97 (1997) 881
- [178] Y. Fujiwara, M. Kohno, K. Miyagawa, Y. Suzuki and J.-M. Sparenberg, *Phys. Rev. C* 70 (2004) 037001
- [179] Y. Suzuki and H. Nemura, *Prog. Theor. Phys.* 102 (1999) 203